Universiteit Antwerpen

UNIVERSITAIRE INSTELLING ANTWERPEN

Departement Natuurkunde

Determination of the partial width and forward-backward asymmetry of the Z^0 boson into $b\bar{b}$ final states

Proefschrift voorgelegd tot het behalen van de graad van Doctor in de Wetenschappen aan de Universitaire Instelling Antwerpen te verdedigen door **Hélène DE BOECK**.

Promotor: Prof. Dr. F. Verbeure

Antwerpen, december 1993.

I do not know what I may appear to the world,
but to myself I seem to have been only like a boy (m/f)
playing on the sea-shore,
and diverting myself in now and then finding a smoother pebble
or a prettier shell than ordinary,
whilst the great ocean of truth lay all undiscovered before me.

Sir Isaac Newton

Acknowledgments

During the last four years, I learned that scientific research is only possible through the collaboration of many individuals. I owe many thanks to a lot of people for helping and encouraging me in my scientific work.

First of all, I am grateful to Frans Verbeure for giving me the opportunity to work in his group and for introducing me in the DELPHI Collaboration. He has continuously guided my steps in my discovery of the world of particle physics and its practitioners. His advice and criticism on the contents and structure of this thesis are very much appreciated.

I thank Peter Kluit for learning me how to treat a big quantity of experimental data. He taught me the art of fitting and analysing the data. He explained me the strategy of presenting and defending the obtained results. The many discussions with him, shed a new light on the ongoing analysis. I thank him for the careful reading of the manuscript, leading to many suggestions. It is a pleasure to work with him.

The members of the DELPHI Collaboration broadened my insight through many useful discussions. Especially, the team11 senior physicists and the members of the subteam of team11 on semileptonic b physics are thanked for creating a stimulating working atmosphere. My view on the art of muon identification was influenced by many discussions with Guy, Paula and Peter. I appreciate very much the help of Tzanko in copying and "stripping" hadronic events.

I am grateful to the DELPHI people of the IIHE group for helping me to get acquainted with the muon detector of DELPHI, for their support, their constructive criticism and for the pleasant gatherings during my stays at CERN.

Special thanks to Eddi De Wolf for his advice on UNIX and computing related problems. I would also like to thank my colleague graduate students, Cao Fang, Sabine and Pierre for their moral support and friendship.

I am grateful to the I.W.O.N.L.(1989-1990) and I.I.K.W.(1990-) for the financial support.

Ik dank mijn ouders voor hun interesse en steun gedurende de laatste acht jaar.

Ik dank Frank voor alle uren die hij besteedde aan het uitleggen van theorie. Ook veel dank voor de morele steun in mijn wetenschappelijk werk. Zijn liefde en geduld tijdens de harde tijden van het schrijven van onze thesissen was een enorme steun.

Contents

I Theoretical Overview 5

1 Theoretical Overview 7

1.1 The standard model of electroweak interactions 7

1.2 Muon decay at tree level 11

1.3 Radiative corrections 12

1.4 Z^0 physics in $e^+e^- \rightarrow f\bar{f}$ 15

1.4.1 Born approximation 15

1.4.2 Improved Born approximation 16

1.5 Partial widths 21

1.6 Asymmetries 25

1.7 Event simulation and fragmentation models 28

1.7.1 The Lund Monte Carlo event generator 28

1.7.2 Heavy hadrons in the Monte Carlo simulation 31

II Experimental Setup 33

2 Experimental Setup 35

2.1 The LEP collider 35

2.1.1 Design 35
2.1.2 Luminosity 37
2.1.3 Machine background processes 39
2.2 The detector DELPHI 41
2.2.1 Tracking devices 43
2.2.2 Combined tracking system 49
2.2.3 Scintillation Counters 51
2.2.4 The Calorimeters 52
2.2.5 Particle Identification 55
2.2.6 Muon Chambers (MUC) 56
2.2.7 Luminosity Detectors 60
2.2.8 Overview of the DELPHI detector 61
2.3 The trigger and data acquisition 63
2.4 Data analysis 68
2.4.1 DELSIM 68
2.4.2 DELANA 69
2.4.3 DELGRA 71

III Analysis of inclusive b quark events 75

3 Muon identification in DELPHI 77

3.1 Extrapolation 80
3.2 EMMASS 80
3.3 MUCFIX 82
3.3.1 Introduction 82

3.3.2 MUCFIX performance 83
3.4 MUFLAG 89
3.4.1 MUFLAG structure 90
3.4.2 Tags and Performance 91
3.5 Conclusion 100

4 Heavy quark tagging **105**

4.1 Hadronic event selection 105
4.1.1 Reconstruction of the quark direction 106
4.1.2 Event selection 108
4.2 Heavy quark enriched sample 109
4.2.1 Lepton tag 110
4.2.2 Boosted sphericity tag 112
4.2.3 Impact parameter tag 115
4.2.4 B lifetime tag 116
4.2.5 Combined tags 116

5 Measurement of $\Gamma_{b\bar{b}}$ and the b forward-backward asymmetry **119**

5.1 Measurement of $\Gamma_{b\bar{b}}$ and the b forward-backward asymmetry using the semileptonic decay into muons 119
5.1.1 Sample composition 120
5.1.2 Fitting procedures 124
5.1.3 Determination of $\Gamma_{b\bar{b}}$ 126
5.1.4 Determination of the b forward-backward asymmetry . . . 131
5.2 Measurement of $\Gamma_{b\bar{b}}$ using a mixed tag method 136
5.2.1 The microvertex tag 136

5.2.2 The lepton tag 140

5.2.3 Fitting procedure 140

5.2.4 Determination of the partial width 142

5.3 Discussion of the results 148

5.3.1 The partial width into bottom quarks 148

5.3.2 Inclusive semileptonic branching ratio of b quarks into muons 150

5.3.3 The b forward-backward asymmetry and the effective weak mixing angle 150

5.4 Comparison with other LEP experiments 152

IV Appendices **157**

A Muon chamber resolution **159**

B Correction of systematics **161**

C Acceptance correction for the forward-backward asymmetry **165**

Introduction

At the end of the previous century, Henri Becquerel discovered the radioactivity of uranium. More than thirty years later, Enrico Fermi argued that the process of radioactivity was the handiwork of an entirely new force of nature, the weak interaction. He constructed a model for β-decay, where he postulated a point-interaction of four fermions. As in photon emission, the decay takes place, in Fermi's theory, at a single space-time point. The neutron turns into a proton and an electron and antineutrino are created. In the late fifties, it was conjectured that weak interactions take place by the exchange of intermediate vector bosons like the electromagnetic interactions are mediated by photons (γ). The force carriers, now called W^+ and W^-, have to be charged to account for the way that weak interactions convey charge. When the weak force transforms a neutron into a positive proton, a virtual negatively charged particle is emitted, and in its decay an electron and an antineutrino are created. From the first attempts to unify the electromagnetic and weak interactions, it became clear in the beginning of the sixties that the hypothesis of only three vector bosons ($W^{\pm}$,γ) was not sufficient and an additional neutral vector boson, the Z^0, was needed for symmetry reasons. However, till then, only charged current weak interactions were observed, e.g. the reaction $\nu_\mu e^- \rightarrow \mu^- \nu_e$, where the initial ν_μ emits a W^+ and turns into a muon. The existence of a neutral weak vector boson would imply the existence of weak "neutral currents", weak interactions where the particles do not change charge. Only in mid-1973, neutral current processes were experimentally observed in the Gargamelle bubble chamber. One candidate for the neutral current reaction $\bar{\nu_\mu} e^- \rightarrow \bar{\nu_\mu} e^-$ was detected [1] in the interactions of an antineutrino beam with a fixed target. In the same experiment, neutral current events of type $[\nu_\mu(\bar{\nu_\mu})N \rightarrow \nu_\mu(\bar{\nu_\mu})$ hadrons], with no final muon or electron, were also seen [2].

The unification of the weak and electromagnetic force, nowadays called the Standard Model (SM), was originally made for leptons only. The hadron sector was initially more complicated: in the 50-60's there was a zoo of particles. In 1964, it was conjectured that hadrons are composed of smaller subunits: the

quarks. All hadrons known at that time, could be described as being made up of two or three quarks of type up (u), down (d) and strange (s). The first experimental evidence of such subunits came in 1968, when it was deduced from deep inelastic scattering of electrons on a hydrogen target at SLAC, that protons were made of point-like, charged structures. Around 1970, the SM was extended to incorporate also the quarks by postulating a fourth quark, the charm quark. The existence of this quark was experimentally confirmed in 1974 by the discovery of a narrow resonance at 3.1 GeV/c^2, the J/ψ, a meson made of a charm (c) and anticharm quark. The fifth quark, the bottom or beauty quark (b), was found from the invariant mass spectrum of muon-antimuon pairs in collisions of 400 GeV protons on nuclear targets at Fermilab in 1978. These two muons are decay products of the Υ meson ($b\bar{b}$), a meson with a mass of 9.44 GeV/c^2. Actually, the sixth quark, the top quark, has not yet been discovered. Although, it is expected to be found in two experiments at the Tevatron, a $p\bar{p}$ collider at Fermi National Laboratory (Chicago), once they have accumulated enough statistics.

A strong confirmation of the Standard Model was provided by the UA1 and UA2 collaborations in 1983, working at the CERN $p\bar{p}$ collider. They detected directly the weak vector bosons $W^{\pm}$ and Z^0. The $W^{\pm}$ was reconstructed from its decay in $e\nu_e$, $\mu\nu_\mu$ and their charge conjugated states and the average value of the W mass was found to be [3]:

$$M_W = (80.8 \pm 1.3)\ \mathrm{GeV/c^2}$$

The Z^0 was observed through its decay in an electron-positron pair and the mass was determined to be:

$$M_Z = (92.0 \pm 1.8)\ \mathrm{GeV/c^2}$$

The SM describes the observable quantities, like branching ratios, in terms of a perturbation expansion in its coupling constants. It is therefore important to test the SM not only on its lowest order terms, but also at the level of quantum corrections, as it has been done for QED. These quantum corrections can be probed if one reaches a 1% accuracy on the observables. Hence, a better precision was needed. In 1982 it was decided at CERN to construct a new electron positron collider, LEP (Large Electron Positron collider), which operates at a centre of mass energy tuned to the mass of the Z^0 boson. This collider is able to produce several thousands of Z^0 events a day, whereas the measurements of UA1 and UA2 are based on a few hundred Z^0's, accumulated over different years of running. The detailed investigation of e^+e^- annihilations around the Z^0 resonance, allows the detection of small calculable deviations from the lowest order predictions for many physical quantities. These higher order corrections are called "radiative corrections". Moreover, these radiative corrections are a window to new physics. Indeed, according to quantum field theory, the virtual

presence of all physical states shows up in higher order calculations. Therefore, the (unknown) top quark mass and Higgs mass will affect the theoretical predictions for various physical quantities in a calculable way. The same idea holds to all kinds of particles connected to theories beyond the SM (all models that are extensions or modifications of the SM), which increase the number of diagrams and add new corrections to the calculation of physical quantities. LEP not only allows detailed studies of the electroweak theory, like the Z^0 mass, its width, asymmetries and branching ratios. Also explicit searches for the Higgs boson, predicted by the Standard Model, and other more exotic particles, showing up in theories beyond the Standard Model like supersymmetry and technicolor, are performed. By selecting the hadronic decay mode of the Z^0, one can study QCD (Quantum ChromoDynamics), the model for the strong interaction. Also the inclusive and exclusive decays of the b and c quarks are popular physics topics at LEP.

This work concentrates on the selection of the decay of the Z^0 into $b\bar{b}$ final states with the DELPHI detector at LEP, by using the semileptonic decay mode of the B hadrons into muons. Therefore it was necessary to study carefully the identification of muons in hadronic events. The forward-backward asymmetry of the b quark in Z^0 decays and the branching ratio of the Z^0 to $b\bar{b}$ is measured with the DELPHI data samples of 1990 till 1992.

This dissertation is divided into three main parts: an overview of the relevant theory, a description of the experimental setup and a part on b quark analyses.

In the first chapter, the Standard Model is sketched and the effects of radiative corrections on the branching ratio of the Z^0 into $b\bar{b}$ states and on the b forward-backward asymmetry are discussed. This illustrates that b quark physics is an interesting and challenging topic. The Monte Carlo generator and the fragmentation of the b quark into hadrons are briefly explained.

The second chapter describes the experimental setup. The accelerator LEP, the detector DELPHI and the data acquisition system of DELPHI are discussed. A short overview of the off-line analysis software is given.

The three remaining chapters of this thesis constitute the part on b quark analyses.

- In the third chapter, an algorithm for identifying muons with the DELPHI detector in hadronic events is explained. The performance of this muon identification is reported.
- In chapter 4, different methods which can be used to select a hadronic sample that contains a majority of b quark events (selection of a b enriched sample) are discussed.

- Chapter 5 contains some inclusive b quark analyses. Two kinds of b quark data analyses are described:
  - A semileptonic single tag method is used to extract the b asymmetry and the $Z^0 \rightarrow b\bar{b}$ branching ratio. This analysis has been performed on the 1990 and 1991 data.
  - A mixed (semileptonic - vertex) tag method is used to determine the $Z^0 \rightarrow b\bar{b}$ branching ratio in a less Monte Carlo dependent way. This method has been applied for the 1991 and 1992 data.

  The electroweak mixing angle and the inclusive semileptonic branching ratio of b quarks into muons are derived from these two measurements. The results of these analyses are discussed and compared with other recent LEP measurements.

Part I

Theoretical Overview

Chapter 1

Theoretical Overview

In this chapter, some aspects of the standard model of electroweak interactions are reviewed in order to put the subsequent physics analyses in a broader perspective. The treatment of radiative corrections and their effects on some observables are discussed. In particular, the partial width of the Z^0 into $b\bar{b}$ pairs and the asymmetry of the b quarks at a centre of mass energy equal to the Z^0 mass, are treated in detail.

In a second part, the LUND Monte Carlo generator of final states from e^+e^- annihilation is discussed. It is explained how the Monte Carlo program evolves the quarks into the final hadrons.

1.1 The standard model of electroweak interactions

Two kinds of particles exist in nature: fermions and bosons. The former, quarks and leptons, are the basic constituents of all matter. Interactions between these elementary fermions are mediated by gauge bosons. Their behaviour is described by the Standard Model (SM) with an astonishing accuracy. In this chapter, some elements of the Minimal Standard Model (MSM) are discussed.

One of the basic features of the SM, proposed by Glashow, Weinberg and Salam, is the concept of local gauge symmetries [5]. The Lagrangian density of a theory constructed following such principles, is invariant under a continuous group of transformations with parameters depending on space and time,

hence the name local symmetries. The symmetry group of the SM Lagrangian is $SU(2) \times U(1)$. $SU(2)$ is the group of rotations, familiar from quantum mechanics. Instead of angular momentum, the quantum numbers associated with it are called weak isospin in the SM. When acting with an element of the $U(1)_Y$ group on a state, it gets multiplied with a complex phase factor. The associated quantum number Y is called hypercharge. The electric charge, known from experiment, is given by the equation $Q = I_3 + \frac{Y}{2}$, where I_3 is the third generator of the $SU(2)$ group.

The next thing one has to do when constructing a model, is choosing a representation of the symmetry group for the fermions, in order to define their transformation under the group. In the SM, one takes different representations for the left and right chirality of the fermions. The left-handed part of the electron, muon and tau lepton are grouped in a doublet representation of $SU(2)$ together with the left-handed neutrinos. Their right-handed parts are in an $SU(2)$-singlet. The massless neutrinos do not have a right-handed component. Notice that the generators I_i of the doublet representation of the $SU(2)$ group are the Pauli-matrices. The left-handed parts of the quarks are also in doublets, the right-handed parts in singlets. The basic building blocks are thus classified as:

$$\begin{pmatrix} \mathrm{e} \\ \nu_\mathrm{e} \end{pmatrix}_L \quad \begin{pmatrix} \mu \\ \nu_\mu \end{pmatrix}_L \quad \begin{pmatrix} \tau \\ \nu_\tau \end{pmatrix}_L \quad \begin{pmatrix} \mathrm{u} \\ \mathrm{d} \end{pmatrix}_L \quad \begin{pmatrix} \mathrm{c} \\ \mathrm{s} \end{pmatrix}_L \quad \begin{pmatrix} \mathrm{t} \\ \mathrm{b} \end{pmatrix}_L \tag{1.1}$$

$$\mathrm{e}_R \quad \mu_R \quad \tau_R \quad \mathrm{u}_R \quad \mathrm{d}_R \quad \mathrm{c}_R \quad \mathrm{s}_R \quad \mathrm{t}_R \quad \mathrm{b}_R \tag{1.2}$$

In order to maintain the local invariance, one generally has to introduce one gauge boson for every gauge generator. A gauge boson is a spin 1 field, represented by a four-vector. Since $SU(2) \times U(1)$ has four generators, there are four gauge bosons in the SM, $W_\mu^{1,2,3}$ for $SU(2)$ and B_μ for $U(1)$. In addition, one has to define how the gauge bosons couple to the fermions: the coupling strength is given by two gauge group coupling constants g_1 for the $U(1)$ group and g_2 for the $SU(2)$ group. The gauge symmetry restricts the number of independent coupling constants to two, one for every symmetry group. It is in this sense that one says that the SM is not really a unification. A unified field theory for electromagnetic and weak interactions would have one symmetry group which contains $SU(2) \times U(1)$. The two independent coupling constants of the SM would then be related. An example, which however is not well supported experimentally, is based on SU(5).

The disadvantage of imposing local gauge invariance, is that it does not allow the presence of explicit mass terms in the Lagrangian, neither for the fermions nor for the gauge bosons. However, it is known from solid state physics

(ferromagnetism, superconductivity) that the ground state of a field theory can have a smaller symmetry group than the symmetry group of the Lagrangian. This process is called spontaneous symmetry breaking. In such a theory one has an order parameter, like the magnetisation or the density of Cooper pairs. Below, this is called the vacuum expectation value v. Spontaneous symmetry breaking has been incorporated in the SM, where it goes under the name Brout-Englert-Higgs mechanism. A doublet (under $SU(2)$ transformations) of complex scalar fields is introduced, with a potential such that classically the ground state is only invariant under $U(1)$ transformations. A massless Goldstone boson is associated with every broken symmetry generator. In the SM there are thus three Goldstone bosons. By fixing a gauge, the three degrees of freedom of the three Goldstone bosons are used to give a mass term for three vector bosons. One massive scalar boson is left, the Higgs boson.

After introducing the Higgs field, the Lagrangian will contain a non-diagonal mass matrix for the gauge bosons. Therefore, a transformation is needed to go to the mass eigenstates:

$$W_\mu^\pm = \frac{1}{\sqrt{2}}(W_\mu^1 \pm W_\mu^2) \tag{1.3}$$

$$Z_\mu = \cos\theta_W W_\mu^3 + \sin\theta_W B_\mu \tag{1.4}$$

$$A_\mu = -\sin\theta_W W_\mu^3 + \cos\theta_W B_\mu, \tag{1.5}$$

with $\sin\theta_W$ the mixing or Weinberg angle. The masses of the bosons are then given by

$$M_W = \frac{1}{2} g_2 v \tag{1.6}$$

$$M_Z = \frac{1}{2} v \sqrt{g_1^2 + g_2^2} \tag{1.7}$$

$$c_W \overset{NOT.}{=} \cos\theta_W = \frac{g_2}{\sqrt{g_1^2 + g_2^2}} = \frac{M_W}{M_Z} \tag{1.8}$$

$$s_W^2 \overset{NOT.}{=} \sin^2\theta_W = 1 - \frac{M_W^2}{M_Z^2} \tag{1.9}$$

Notice that the masses of the gauge bosons are determined by the gauge couplings and the vacuum expectation value. The so-called ρ_o parameter is defined as

$$\rho_o = \frac{M_W^2}{c_W^2 M_Z^2}, \tag{1.10}$$

and ρ_o equals 1 in the MSM. This parameter is different from unity in the non-minimal versions of the Higgs sector and then the relation (1.9) becomes

$$s_W^2 \overset{NOT.}{=} \sin^2\theta_W = 1 - \frac{M_W^2}{\rho_o M_Z^2} \tag{1.11}$$

Identifying A_μ with the photon field which couples via the electric charge e of the electron, e can be expressed as

$$e = g_2 s_W = g_1 c_W .$$

The fermions couple with the scalar Higgs field ϕ by a Yukawa coupling (the scalar constructed from the product of ϕ with the fermion scalar density). If g_f is the Yukawa coupling constant, the fermion mass is given by:

$$m_f = \frac{g_f v}{\sqrt{2}}.$$

Note that the coupling constants are different for every fermion species and are not determined by the model. The couplings of the fermions to the charged and neutral currents, are given by the following vertices:

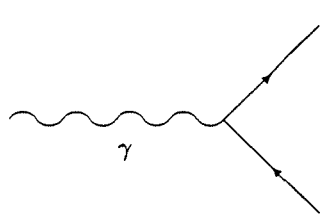

$-ieQ_f\gamma_\mu$

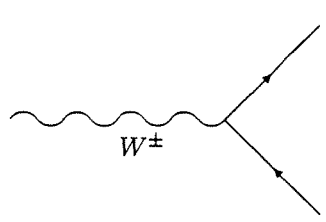

$ie\gamma_\mu(1-\gamma_5)\frac{1}{2\sqrt{2}s_W}$

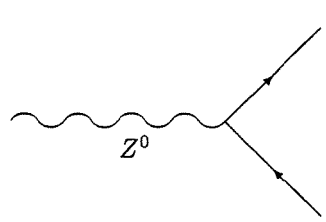

$ie\gamma_\mu(v_f - a_f\gamma_5)\frac{1}{2s_W c_W}$

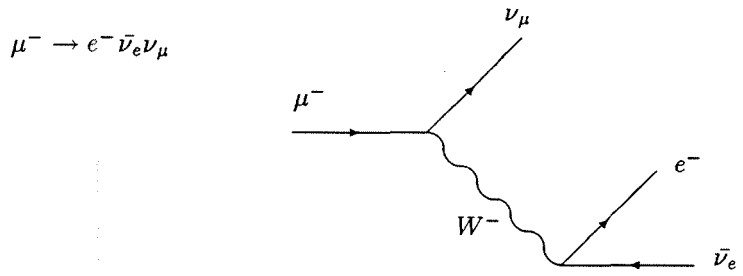

Figure 1.1: Lowest order diagram for the μ decay

with γ_μ the Dirac matrices, Q_f the electric charge of the fermion, a_f and v_f its axial and vector coupling constants with the Z boson. The vector and axial couplings are a function of the third component of the weak isospin, the electric charge and the mixing angle:

$$v_f = I_3^f - 2Q_f s_W^2 \quad (1.12)$$

$$a_f = I_3^f \quad (1.13)$$

The strong interaction can also be described by a gauge theory. The theory describes the hadrons as being made of pointlike quarks. The quarks have a quantum number, called colour charge, which can take three values. These three colours form the components of an SU(3) triplet. The observed hadronic states are colourless singlets. The symmetry group of the QCD (Quantum Chromo Dynamics) Lagrangian is SU(3). SU(3) has eight generators and hence eight gauge bosons, called gluons. The coupling constant of QCD is called α_s.

Now the muon decay in the SM at tree level and the second order terms of this decay is discussed. This process is easily calculable and will allow us to express the vector boson masses in terms of the muon lifetime, the electric charge and the mixing angle.

1.2 Muon decay at tree level

The decay amplitude $\mu^- \to e^- \bar{\nu}_e \nu_\mu$ can be calculated by the Fermi model with effective coupling G_μ as well as by the lowest order of the SM. The lowest order diagram of this process is depicted in Fig.1.1. At low energies, $q^2 << M_W^2$, with $q^2 = p_{final}^2 - p_{initial}^2$ the four momentum transfer and the propagator $\frac{1}{q^2+M_W^2}$

of the SM can be approximated by $\frac{1}{M_W^2}$, the propagator of the four fermion interaction. Identifying these two interactions gives:

$$\frac{G_\mu}{\sqrt{2}} = \frac{e^2}{8 s_W^2 M_W^2} = \frac{e^2}{8 s_W^2 c_W^2 M_Z^2}, \tag{1.14}$$

which allows us to predict the vector boson masses in terms of $\alpha(0) = \frac{e^2}{4\pi}, G_\mu$ and s_W^2. With $\alpha(0) = 1/137.0359895$, $G_\mu = 1.16639\,10^{-5}\mathrm{GeV}^{-2}$ from muon lifetime measurements and $s_W^2 = 0.2325 \pm 0.0008$ [6], the electroweak mixing angle which was already measured (although not with the quoted precision) in the neutrino experiment Gargamelle [1, 2], the following masses are obtained

$$M_W = 77.32 \pm 0.13\ \mathrm{GeV/c^2} \tag{1.15}$$
$$M_Z = 88.25 \pm 0.10\ \mathrm{GeV/c^2} \tag{1.16}$$

This can be compared to the experimentally measured masses [4, 13][1] :

$$M_W = 80.36 \pm 0.33 \pm 0.17\ \mathrm{GeV/c^2}\ \text{(UA2)} \tag{1.17}$$
$$M_W = 79.91 \pm 0.39\ \mathrm{GeV/c^2}\ \text{(CDF)} \tag{1.18}$$
$$M_Z = 91.187 \pm 0.007\ \mathrm{GeV/c^2}\ \text{(LEP)} \tag{1.19}$$

The discrepancy of more than 10 standard deviations is a strong indication that higher order diagrams have to be taken into account.

1.3 Radiative corrections

Till now, only discussed the "lowest order" or "Born" diagram of the process $\mu^- \rightarrow e^- \bar{\nu}_e \nu_\mu$ were discussed, i.e. the diagram that connects the initial and final states by the minimum number of vertices, the first term of the perturbation series. The next order will contain closed loops. When calculating the amplitudes associated to diagrams with such a closed loop, divergent terms show up. The procedure to treat these divergences, consists of two steps. Firstly, the divergences need to be isolated: one has to replace the divergent integral I showing up in the calculation of the amplitude, by a set of integrals $I(\mu)$ that are all function of a parameter μ. Those integrals are well defined for a large range of μ values and the original (divergent) integral is obtained by taking a certain limit for μ. The calculations are performed for the well-defined integrals, and the result for the divergent integral is then defined as the limit for μ of the result of the well-defined integrals. The result will be a set of finite terms and a

[1] UA2 measures the ratio M_W/M_Z. The value for M_W has been obtained using the M_Z measurement from LEP.

set of divergent terms. This is called the regularisation. Secondly the divergent terms are absorbed in some free parameters of the theory. In the MSM, the free parameters entering the amplitudes are e, M_W, M_Z and s_W^2; however, the mixing parameter s_W^2 is related to the boson masses by (1.9) and one is left with three independent parameters e, M_W and M_Z. These quantities e and the two masses in the Lagrangian need to be reinterpreted. They are not the physical charge or masses, but some bare charge e_0 or mass M_W^0, M_Z^0, related to the physical charge or mass by

$$e_0 = e + \delta e \tag{1.20}$$
$$M_W^0 = M_W + \delta M_W \tag{1.21}$$
$$M_Z^0 = M_Z + \delta M_Z. \tag{1.22}$$

$\delta e, \delta M_W$ and δM_Z are called the counterterms, taken such that e remains the coupling constant of the photon to the fermions and such that the pole of the propagator of the vector bosons corresponds to the physical mass of the associated particle. This is called the *on mass* renormalisation scheme. Note that, even if the loop integrals would not diverge and no regularisation is needed, one still would have to renormalise.

Below, the structure of the corrections to the Born approximation will be treated. It is assumed that the divergences have been taken care of. In the 1-loop diagrams, one identifies different types of corrections. They are:

- QED corrections: they consists of diagrams with an extra photon added to the Born diagrams, either as a real bremsstrahlung photon (initial and final state radiation) or a virtual photon loop.
- Weak corrections: these are the diagrams which involve corrections to the vector propagators γ, Z or W (self-energies), the set of vertex corrections and box diagrams with two massive boson exchanges. All these corrections have the effect of modifying the effective coupling constants. The vector boson self-energy corrections are called "oblique" corrections.

Taking the 1-loop diagrams into account, the Fermi coupling constant is given by the expression:

$$\frac{G_\mu}{\sqrt{2}} = \frac{e^2}{8 s_W^2 M_W^2}(1 + \Delta r), \tag{1.23}$$

with Δr the contribution of all radiative corrections of the 1-loop order of the charged current. It can be shown that $\Delta r(e, M_W, M_Z, M_H, m_t)$ is a finite combination of loop diagrams and counterterms. The contributions to Δr is split in three categories:

$$\Delta r = \Delta\alpha + \Delta r^{top} + \Delta r^{remainder}$$

- $\Delta\alpha$ is the correction originating from the vacuum polarisation of the photon:

$$\alpha(q^2) = \frac{\alpha(0)}{1 - \Delta\alpha}$$

  $\alpha(q^2)$ is called the running electromagnetic coupling constant. At $q^2 = M_Z^2$, the correction $\Delta\alpha = 0.0602 \pm 0.0009$ and the coupling constant $\alpha(M_Z^2)$ takes the value $\frac{1}{128.8}$.

- Δr^{top} contains the leading quadratic correction from a large top mass.

$$\Delta r^{top} = -\frac{c_W^2}{s_W^2}\Delta\rho,$$

  with

$$\Delta\rho = N_C \frac{\alpha}{16\pi s_W^2 c_W^2}\frac{m_t^2}{M_Z^2}, \tag{1.24}$$

  with N_C the colour factor, 3 for quarks, and 1 for leptons.

- All other terms are collected in $\Delta r^{remainder}$, which also contains a term logarithmic in the top mass and a term logarithmic in the Higgs mass. This term is numerically not so important, it is of the order ~ 0.01.

The value of Δr calculated in the on-mass renormalisation scheme is very sensitive to a large top mass. The sensitivity to the Higgs mass is much less, due to its logarithmic dependence.

Taking higher order terms into account, it can be proven[7] that the Fermi coupling constant as given by

$$G_\mu = \frac{\pi}{\sqrt{2}}\frac{1}{M_W^2 s_W^2}\frac{\alpha}{1 - \Delta r} \tag{1.25}$$

takes correctly into account all orders in the logarithmic corrections $(\Delta\alpha)^n$. However, in case of a heavy top, where also $\Delta\rho$ is large, the powers $(\Delta\rho)^n$ are not correctly resummed in (1.25) and another expression has to be used. The parameter ρ is defined as $\frac{1}{(1-\Delta\bar{\rho})}$, with $\Delta\bar{\rho}$ the $\Delta\rho$ correction, taking higher orders into account. It can be shown that this ρ enters in the same way in the expressions as the tree level parameter ρ_o in equation (1.11). Hence, up to a small quantity, they are indistinguishable from an experimental point of view and the top quark effect can not be disentangled from other effects.

Note that s_W^2 in (1.25) is not the effective mixing angle in the neutral current vector coupling at the Z^0 peak. The coupling constants get additional contributions from $\gamma - Z$ mixing and vertex corrections [7].

1.4 Z^0 physics in $e^+e^- \to f\bar{f}$

The radiative corrections of the process $e^+e^- \to (\gamma, Z^0) \to f\bar{f}$ are not the same as the ones associated to the charged current ($W^\pm$ exchange, see above), due to the γ, Z mixing which will redefine the neutral current coupling constants. First the tree level amplitude (Born approximation) is reviewed and then the non-QED or weak corrections is concentrated on.

1.4.1 Born approximation

The lowest order diagrams in $e^+e^- \to (\gamma, Z^0) \to f\bar{f}$ are depicted below.

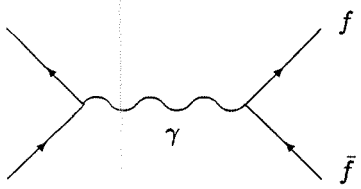

(1)

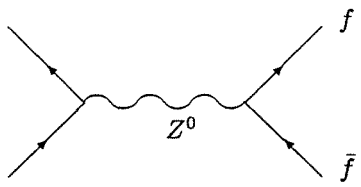

(2)

The amplitude associated to diagram (1) is given by

$$4\pi\alpha(0)\frac{Q_e Q_f}{s}\gamma_\mu \otimes \gamma^\mu,$$

with s the square of the centre of mass energy. The notation $\gamma_\mu \otimes \gamma^\mu$ is used as abbreviation for $\bar{u}(k_2)\gamma_\mu u(k_1)\bar{u'}(k_2')\gamma^\mu u'(k_1')$, with u and u' the spinors associated to the initial and final state fermions with four-vectors k_1, k_2 and k_1', k_2' respectively. The amplitude associated to diagram (2) is given by

$$\sqrt{2}G_\mu \rho_0 M_Z^2 \frac{\left[\gamma_\mu (I_3^e - 2Q_e s_W^{0\,2}) - I_3^e \gamma_\mu \gamma_5\right] \otimes \left[\gamma^\mu (I_3^f - 2Q_f s_W^{0\,2}) - I_3^f \gamma^\mu \gamma_5\right]}{s - M_Z^{0\,2}},$$

with I_3^e and I_3^f the third component of the weak isospin of the electron e and the final state fermion f.

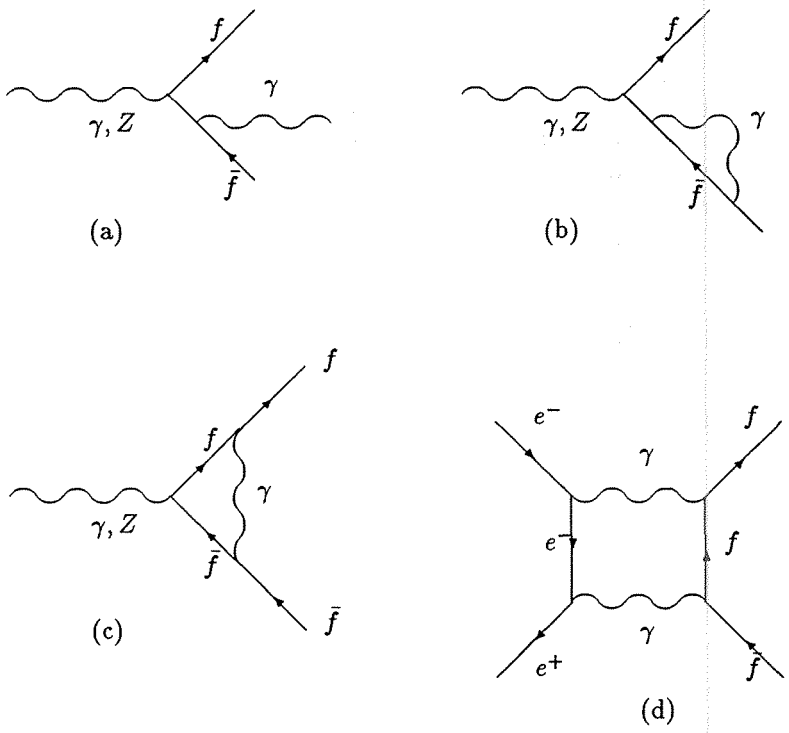

Figure 1.2: QED corrections: Real final state bremsstrahlung (a), virtual QED corrections (b), (c) and (d)

1.4.2 Improved Born approximation

The different types of 1-loop diagrams for $e^+e^- \rightarrow f\bar{f}$ are shown in Figs.1.2 and 1.3 where the blobs denote the sum of the individual contributions to the self-energies and vertex corrections. The vertex corrections and fermion self-energies are explicitly shown in Fig.1.4. After "tedious" calculations, the total amplitude can be written as the sum of a "dressed" photon amplitude and a dressed Z amplitude plus the contributions from the box diagrams which are numerically not significant around the Z^0 peak (relative contribution $< 10^{-4}$).

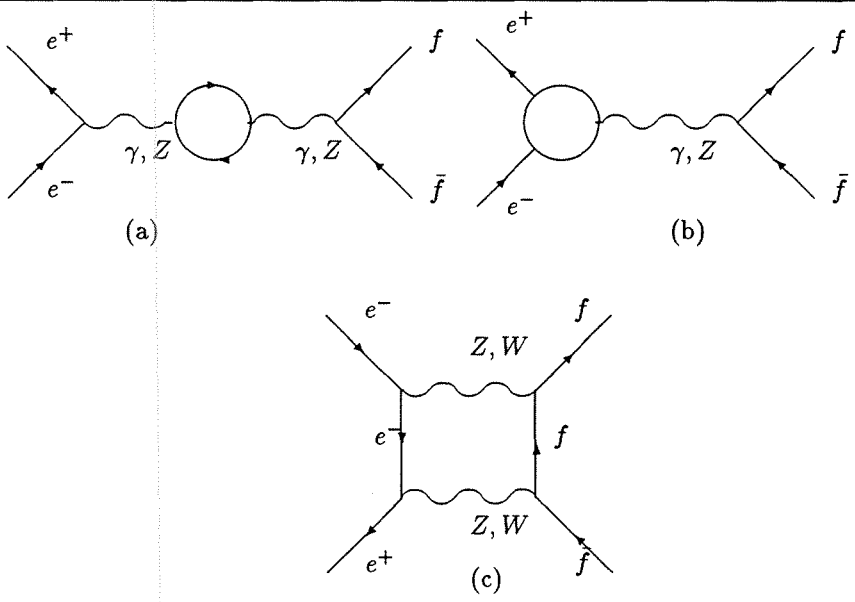

Figure 1.3: Non-QED corrections: boson self-energies (a), vertex corrections (b) and box diagrams (c)

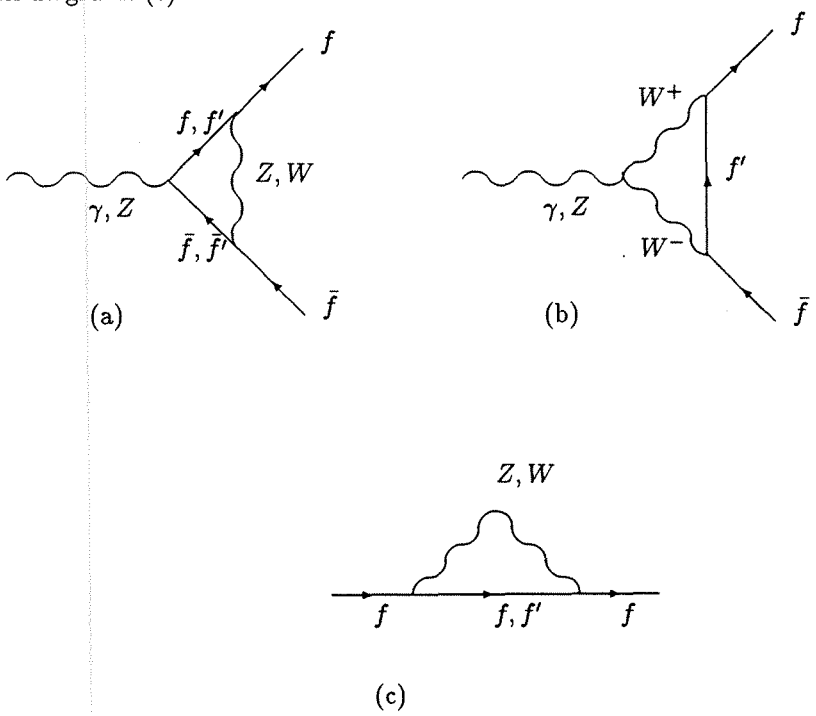

Figure 1.4: Non-QED vertex corrections (a), (b) and fermion self-energies (c)

Dressed photon amplitude

The dressed photon amplitude can be written as

$$A_\gamma = 4\pi\alpha(s)\frac{Q_e Q_f}{s}\left[(1+F_V^{\gamma e})\gamma_\mu - F_A^{\gamma e}\gamma_\mu\gamma_5\right] \otimes \left[(1+F_V^{\gamma f})\gamma^\mu - F_A^{\gamma f}\gamma^\mu\gamma_5\right]$$

The form factors $F_{V,A}(s)$ arise from the vertex correction diagrams and the external fermion self-energies. The typical sizes of the corrections are

$$F_V^{\gamma e}(M_Z^2) \simeq F_A^{\gamma e}(M_Z^2) \simeq 10^{-3} \tag{1.26}$$

The photon form factors are negligibly small around the Z peak.

Dressed Z amplitude

The dressing of the Z amplitude has much more important corrections to the Born amplitude. Without the box diagrams, it is given by

$$A_Z = \sqrt{2}G_\mu\sqrt{\rho_e\rho_f}M_Z^2 \times$$

$$\frac{\left[\gamma_\mu(I_3^e - 2Q_e s_W^2\kappa_e) - I_3^e\gamma_\mu\gamma_5\right] \otimes \left[\gamma^\mu(I_3^f - 2Q_f s_W^2\kappa_f) - I_3^f\gamma^\mu\gamma_5\right]}{s - M_Z^2 + i\frac{s}{M_Z^2}M_Z\Gamma_Z} \tag{1.27}$$

with ρ and κ fermion-dependent form factors. This form is quite close to the Born amplitude, the weak corrections show up in the form factors ρ and κ and in the s-dependent width in the denominator. The total cross section of the Z^0 resonance is a Breit-Wigner expression, with Γ_Z the width of the Z^0.

The form factors ρ and κ have universal parts (i.e. independent of the fermion) and non-universal parts, which explicitly depend on the kind of external fermions.

$$\rho_{e,f} = 1 + \Delta\rho_{univ} + \Delta\rho_{non-univ} \tag{1.28}$$

$$\kappa_{e,f} = 1 + \Delta\kappa_{univ} + \Delta\kappa_{non-univ} \tag{1.29}$$

The universal parts arise from the counterterms and the boson self-energies, the non-universal parts from the vertex corrections and the fermion self-energies in the external lines. In the leading terms, the universal contributions are

$$\Delta\rho_{univ} = \Delta\rho + \ldots \tag{1.30}$$

$$\Delta\kappa_{univ} = \frac{c_W^2}{s_W^2}\Delta\rho + \ldots \tag{1.31}$$

with $\Delta\rho$ as given by (1.24). Note that in (1.27) the effective mixing angle in the vector couplings is given by:

$$\sin^2\theta^f_{eff} = s^2_W\kappa_f = \bar{s}^2_W + \Delta\kappa_{non-univ}s^2_W$$

In this expression, $\bar{s}^2_W$ denotes the universal mixing angle for all fermion species:

$$\bar{s}^2_W = s^2_W(1 + \frac{c^2_W}{s^2_W}\Delta\rho + \ldots).$$

In analogy to (1.25), a new quantity $\Delta\bar{r}$ is introduced which relates $\bar{s}^2_W$ to the Z mass, if the self-energy contributions are included:

$$M^2_Z\bar{c}^2_W\bar{s}^2_W = \frac{\pi\alpha}{\sqrt{2}G_\mu}\frac{1}{1-\Delta\bar{r}}$$

For light fermions, the non-universal contributions are small and the leading top quark and Higgs mass terms enter only via the universal part. All the light quarks have the same heavy particle effects. This is, however, not true for b quarks where also the non-universal parts have a strong m_t dependence, due to the virtual top quarks in the vertex corrections. The non-universal parts of the form factors for b quarks is as follows:

$$(\Delta\rho)^b_{non-univ} = -\frac{4}{3}\Delta\rho - \frac{\alpha}{4\pi s^2_W}(\frac{8}{3} + \frac{1}{6c^2_W})\log\frac{m^2_t}{M^2_W} + \ldots \quad (1.32)$$

$$(\Delta\kappa)^b_{non-univ} = -\frac{1}{2}(\Delta\rho)^b_{non-univ} + \ldots \quad (1.33)$$

Due to the term $\Delta\rho$ in (1.32), the non-universal part for b quarks overcompensates the top dependence of the universal part $(\Delta\rho)_{univ}$ in (1.30). This dependence is due to the vertex corrections, where top quarks are contained in the vertex loop. This correction is much bigger for b quarks than for the other quarks due to the Kobayashi-Maskawa matrix element V_{tb}, which is expected to be approximately unity. This correction leads to a much weaker top mass dependence associated with $b\bar{b}$ final states. This is one of the main reasons why the b quark is of special interest.

The LEP experiments measure the effective electroweak mixing angle, which absorbs the weak corrections. SM calculations show that $\sin^2\theta^f_{eff}$ is flavour independent within 0.04% with the exception of b quarks. At LEP, the effective electroweak mixing angle is taken to be $\sin^2\theta_{eff}$ for all fermions except for b

quarks. The effective weak mixing angle for b quarks, $\sin^2\theta^b_{eff}$, is related to $\sin^2\theta_{eff}$ by

$$\sin^2\theta^b_{eff} = (1+\frac{2}{3}\Delta\rho)\sin^2\theta_{eff},$$

$$\Delta\rho = \frac{3G_F m_t^2}{8\pi^2\sqrt{2}}$$

The value $\sin^2\theta^b_{eff}$ is 0.4% larger than $\sin^2\theta_{eff}$, for a top quark mass of 150 GeV.

Improved Born approximation

Restricting ourselves to the leading terms in the form factors, one can give a recipe to write down an "improved Born approximation", which contains all large corrections from light and heavy fermions. It is sufficient to replace the bare parameters of the tree level expressions by:

$$\alpha(0) \Rightarrow \alpha(M_Z^2) \tag{1.34}$$

$$\rho_0 \Rightarrow \sqrt{\rho_e\rho_f} \tag{1.35}$$

$$s_W^2 \Rightarrow sin^2\theta^f_{eff} \tag{1.36}$$

$$iM_Z\Gamma_Z^0 \Rightarrow i\frac{s}{M_Z}\Gamma_Z \tag{1.37}$$

1.5 Partial widths

The partial width is the probability of transition per unit of time of a Z^0 into a given final state $f\bar{f}$. The total Z^0 width is the sum of the partial widths of all possible final states. The partial width in the improved Born approximation, when neglecting the finite fermion mass, is given by

$$\Gamma(Z \to f\bar{f}) = N_C^f \frac{M_Z}{48\pi}\sqrt{2}G_\mu M_Z^2 \rho_f [1 + (2I_3^f - 4Q_f s_W^2 \kappa_f)^2](1 + \delta_{QED}) + \Delta\Gamma_{QCD}$$

with $N_C^f = 3$ for quarks and $N_C^f = 1$ for leptons. δ_{QED} and $\Delta\Gamma_{QCD}$ denote the QED and QCD corrections to the partial width, respectively. This expression can also be written as

$$\Gamma(Z \to f\bar{f}) = N_C^f \frac{M_Z}{12\pi}\sqrt{2}G_\mu M_Z^2 [|g_A^f|^2 + |g_V^f|^2](1 + \delta_{QED}) + \Delta\Gamma_{QCD},$$

where the effective axial and vector coupling constants, g_A^f and g_V^f, are introduced.

$$g_A^f \Rightarrow \sqrt{\rho_f} I_3^f \tag{1.38}$$

$$g_V^f \Rightarrow \sqrt{\rho_f}(I_3^f - 2Q_f s_W^2 \kappa_f) \tag{1.39}$$

Taking into account the finite mass of the b quark, the partial width becomes:

$$\Gamma(Z \to f\bar{f}) = N_C^f \frac{M_Z}{12\pi}\sqrt{2}G_\mu M_Z^2 \beta [|g_A^f|^2\beta^2 + |g_V^f|^2 \frac{3-\beta^2}{2}](1 + \delta_{QED}) + \Delta\Gamma_{QCD}.$$

β is the velocity of the quark and given by $\beta = \sqrt{1-\mu^2}$ and $\mu^2 = \frac{4m_b^2}{s}$. The additional photonic QED correction δ_{QED} for the final state is very small ($\simeq 0.17\%$ for leptons and 0.019 % for b quarks) and given by

$$\delta_{QED} = \frac{3}{4}\frac{\alpha}{\pi}Q_f^2.$$

Taking the gluon corrections for the hadronic final state into account, the axial and vector part of the width is changed as follows:

$$|g_V^f|^2 \Rightarrow |g_V^f|^2(1 + c_V \frac{\alpha_s}{\pi} + \ldots) \tag{1.40}$$

$$|g_A^f|^2 \Rightarrow |g_A^f|^2(1 + c_A \frac{\alpha_s}{\pi} + \ldots) \tag{1.41}$$

$$c_V = 1 + 3\mu^2 + \ldots \tag{1.42}$$

$$c_A = 1 + 3\mu^2 \log\frac{4}{\mu^2} + \ldots \tag{1.43}$$

This correction is of the order of 4%.

Hence, the partial widths of $Z^0 \rightarrow f\bar{f}$ have, through ρ_f, a quadratic dependence on the mass of the top quark (see 1.24), except for $Z^0 \rightarrow b\bar{b}$ where the dependence is almost logarithmic (see 1.32). The top mass dependence on the partial width of the different flavours is shown in Fig.1.5a.

A priori, due to the poor sensibility of $\Gamma_{b\bar{b}}$ to the top mass, this observable does not seem very useful. However, the quantity $R_b = \frac{\Gamma_{b\bar{b}}}{\Gamma_{had}}$, where Γ_{had} is the total hadronic width, is an important observable:

- It isolates the b-vertex corrections, as the oblique corrections (the boson self-energy corrections, the universal corrections) cancel in the ratio. This feature allows to determine the top mass independently from the ρ parameter and the Higgs mass. A recent analysis, using the ratio of the b partial width to the leptonic width [18], puts a limit on the top mass of

  $$m_t < 208 \text{ GeV/c}^2 \text{ at 95 \% confidence level}$$

  The top mass dependence of $\frac{\Gamma_{b\bar{b}}}{\Gamma_{had}}$ is shown in Fig.1.6.

- Moreover, R_b is only weakly dependent on QCD corrections: $\Delta R_b < 0.1\%$ for a 10 % variation in α_s. This, together with its insensitivity to radiative corrections, makes it a good probe for a search for new physics, once the top mass is known. There are a number of mechanisms beyond the SM, which affect the branching fraction to $b\bar{b}$. These extensions can be disentangled from the $Zb\bar{b}$ vertex by measuring several quantities if one can reach a high accuracy (1% level). The method is detailed in ref.[11].

  - The Z': if one goes to higher dimensional symmetry groups, it is possible to generate more weak vector bosons. This will alter the top mass dependence of R_b.
  - *A second Higgs doublet*: it is possible to construct a theory with two Higgs doublets instead of one. This leads to a pair of charged Higgs scalars and a pair of neutral Higgs scalars. This would lead to a number of new vertex diagrams. The effect of these additional diagrams can be calculated and is shown in Fig.1.7 as the dotted line.
  - *Supersymmetry* SUSY requires that every fundamental particle has its supersymmetric partner with the same charge, colour, but a spin different by 1/2. All these new particles give rise to new diagrams and thus another top mass dependence of R_b [12]. It is shown in Fig.1.7 as the dashed line.

Experimental results will be discussed in Chapter 5.

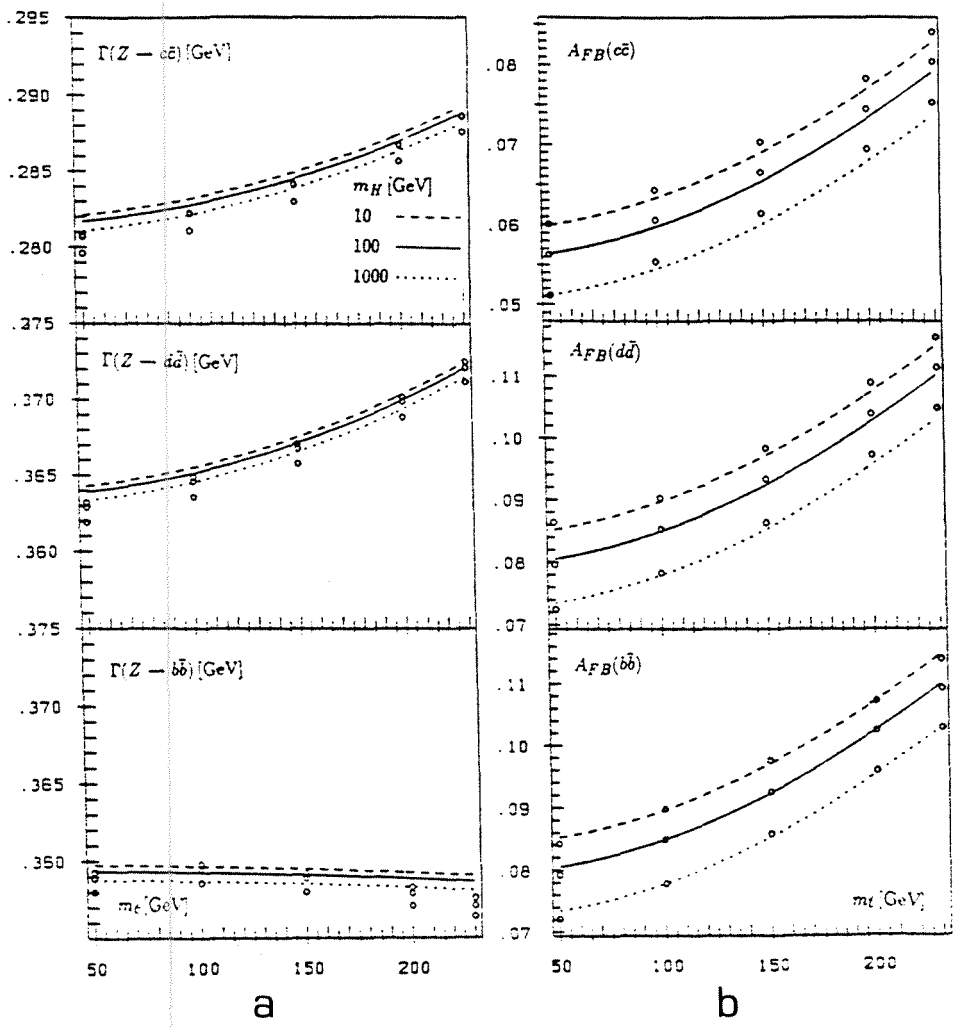

Figure 1.5: a)Partial width dependence on the top mass; b)Asymmetry dependence on the top mass

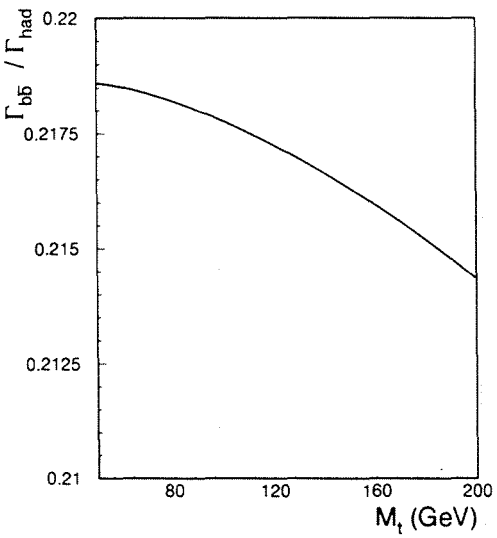

Figure 1.6: R_b dependence on the top mass

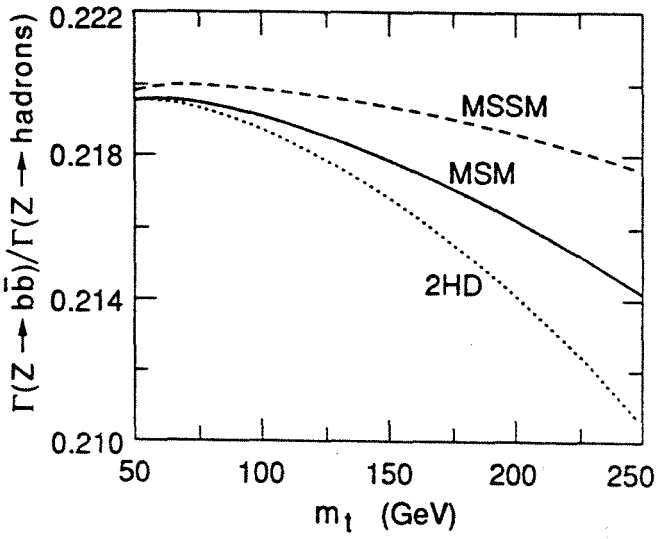

Figure 1.7: Top mass dependence for different models

1.6 Asymmetries

The forward-backward asymmetry is defined as

$$A_{FB}^f = \frac{\sigma^F - \sigma^B}{\sigma^F + \sigma^B},$$

with

$$\sigma^F = \int_{\theta=0}^{\theta=\pi/2} d\Omega \frac{d\sigma}{d\Omega}, \quad \sigma^B = \int_{\theta=\pi/2}^{\theta=\pi} d\Omega \frac{d\sigma}{d\Omega}.$$

$d\sigma/d\Omega$ is the angular differential cross section for b quarks. At $\sqrt{s} = M_Z$, this asymmetry is given by

$$A_{FB}^f = \frac{3}{4} \frac{2 g_A^e g_V^e}{{g_A^e}^2 + {g_V^e}^2} \frac{2 g_A^f g_V^f \beta}{{g_A^f}^2 \frac{3-\beta^2}{2} + {g_V^f}^2 \beta^2} + \Delta A_{FB}^I + \Delta A_{FB}^Q.$$

ΔA_{FB}^I is a small contribution resulting from the interference with the photon exchange (for b quarks it is 0.0004). ΔA_{FB}^Q is a small contribution from the pure photon exchange part (for b quarks it is -5.10^{-5}). These two contributions will be neglected in the following discussion. As a consequence of an accidental cancellation among the coupling constants, the mass correction is strongly suppressed and β can be taken to be one. The asymmetry at the Z resonance can be approximated by

$$A_{FB}^f = \frac{3}{4} A_e A_f, \tag{1.44}$$

with

$$A_f = \frac{2 g_V^f g_A^f}{{g_A^f}^2 + {g_V^f}^2} = \frac{2|2I_3^f - 4Q_f \sin^2\theta_{eff}^f|}{1 + (2I_3^f - 4Q_f \sin^2\theta_{eff}^f)^2} \tag{1.45}$$

The asymmetry is modified by final state QED and QCD corrections and can be written for b quarks as follows:

$$A_{FB}^b \Rightarrow A_{FB}^b (1 - \frac{3}{4} Q_b^2 \frac{\alpha}{\pi})(1 - \frac{\alpha_s}{\pi}(1 - \frac{4}{3}\pi \frac{m_q}{M_Z}))$$

The electroweak corrections can change the asymmetry value by as much as 0.04, for a top quark mass range of 50 to 230 GeV/c^2. The top mass dependence is much stronger than in $\Gamma_{b\bar{b}}$, but it is also much more dependent on the Higgs mass. This is shown in Fig. 1.5. The b asymmetry has a large s_{eff}^2 dependence as compared to the $\mu^+\mu^-$ asymmetry, and this makes it a good observable for measuring s_{eff}^2. The measured asymmetry as function of the effective mixing angle is depicted in Fig.1.8 for leptons, c and b quarks.

The forward-backward asymmetry of the quark is extracted by measuring the asymmetries of hadrons containing a b quark. For b quarks, there is not

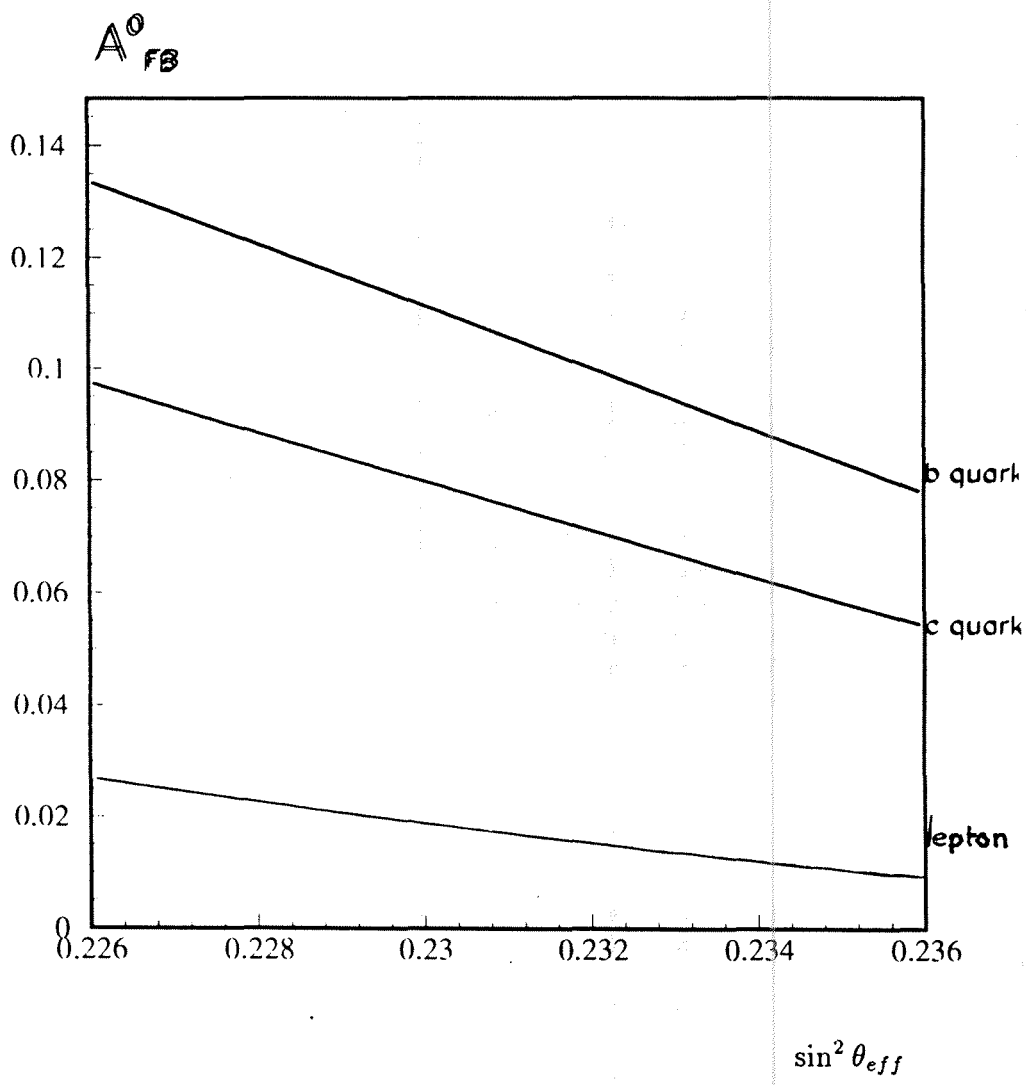

Figure 1.8: The lepton, c and b asymmetries as a function of the effective mixing angle

a one-to-one correspondence between the b quark and the B hadron, due to mixing in the neutral B_d^0 and B_s^0 system. The particles mix ($\bar{B}_d^0 \rightarrow B_d^0$ and $\bar{B}_s^0 \rightarrow B_s^0$) so that the b flavour changes at a rate comparable to or much more frequently than the decay rate for $\bar{B}_d^0$ and $\bar{B}_s^0$ respectively. This mixing reduces the b quark asymmetry

$$A_{FB}^{obs}(b) = (1 - 2\chi)A_{FB}(b),$$

with χ the probability of finding a $\bar{b}$ quark in a b beam. χ is a weighted mixture of B_d and B_s mixing parameters. The LEP measured value for χ [70, 71, 75] is

$$\chi^{LEP} = 0.115 \pm 0.009 \pm 0.006.$$

and hence the mixing will reduce the forward-backward asymmetry to $\simeq 75\%$ of the asymmetry at production.

1.7 Event simulation and fragmentation models

1.7.1 The Lund Monte Carlo event generator

During physics analyses, extensive use is made of Monte Carlo simulations. In the analyses presented below, for example, the momenta and transverse momenta of leptons from semileptonic decays of heavy quarks, are compared with those of simulations. Also b-tagging efficiencies and lepton identification efficiencies are extracted by applying the same algorithm to simulated events.

The Monte Carlo simulation evolves in two different phases:

- First, the generation of a final state from e^+e^- annihilation, i.e. a set of particles and their energy-momentum four-vectors, is generated.
- Second, the interaction of the particles with the detector is simulated.

The generation of the final state particles in the LUND Monte Carlo program JETSET [17], which will be used in the following analyses, is discussed below. Electrons and positrons, each having an energy around 46 GeV, are annihilated and a quark-antiquark pair is created. The hadronisation of $q\bar{q}$ to hadrons can not be treated exactly and is thus based on a phenomenological model. These models are permanently updated and tested using the results of different experiments.

The three different steps in the generation of final state particles are illustrated in figure 1.9. They are:

- **Perturbative QCD.** The production of a $q\bar{q}$ pair in a Z^0 decay is a pure electroweak process. Once the quarks are produced, they can evolve into gluons and more quarks: a process that can be described by perturbative QCD. However, till now only processes of order α_s^2 have been calculated analytically. The computation of matrix elements of order α_s, leads to final states of 3 partons (the 2 quarks + the emission of one gluon). At order α_s^2, the parton state can be 4 quarks or 2 quarks and 2 gluons.

  The so-called Parton Shower model is another way to evolve the initial quarks to a set of partons. The parton shower model is based on an iterative use of the basic branchings: $q \rightarrow qg$, $g \rightarrow gg$ and $g \rightarrow q\bar{q}$. At every stage of this evolution, the system is characterised by a parameter, typically an energy or a mass scale. The probability for one of these

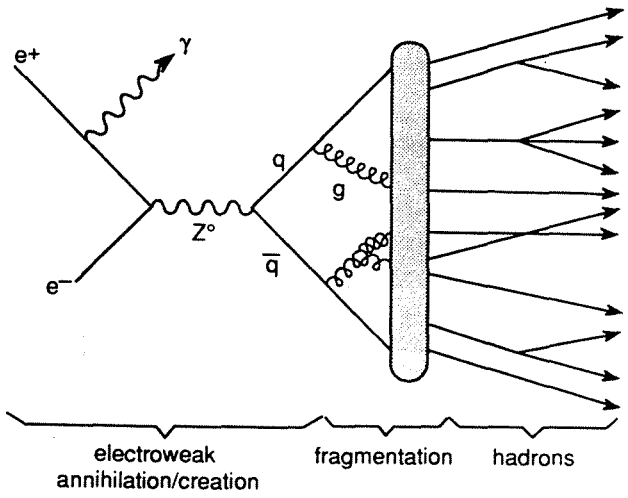

Figure 1.9: Schematic illustration of an e^+e^- annihilation

branching processes to occur depends on this parameter. The way these probabilities change when the characteristic parameter changes, i.e. during the evolution from initial state to final state of partons, is determined by the Altarelli-Parisi equations.

- **Hadronisation (or fragmentation).** The cascade is stopped when a typical mass scale of confinement is reached, around 1 GeV. At this stage, one is left with coloured objects (quarks and gluons), which have to be combined in colourless objects. Different models exist to do this. The LUND Monte Carlo program uses the "string fragmentation" [16]. This is a QCD inspired model, in which a colour tube is stretched between the original partons, and breaks into $q\bar{q}$ pairs according to given distributions in the z-variable, $f(z)$. z is defined as the ratio of the sum of energy and longitudinal momentum of the hadron with respect to the direction of the original parton and the sum of energy and momentum of that original parton.

$$z = \frac{(E + p_L)_{hadron}}{(E + p)_{parton}}$$

The breaking of a string in this approach is shown in fig 1.10. The hatched areas indicate nonvanishing colour fields.

The fragmentation function used in the LUND program is the left-right symmetric fragmentation function of the form:

$$f(z) \sim \frac{(1-z)^a}{z} e^{(-b\frac{m_T^2}{z})},$$

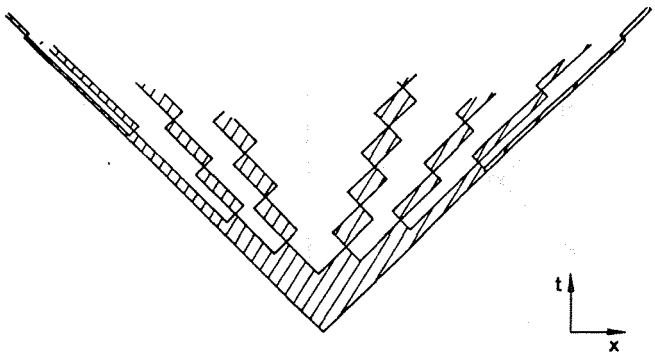

Figure 1.10: Breaking of a string in the Lund approach. Time is the vertical, distance the horizontal axis.

Year	version	ϵ_b	ϵ_c
1990	Jetset 7.2 Pet.	3.10^{-3}	24.10^{-3}
1991	Jetset 7.3 Pet.	6.10^{-3}	54.10^{-3}

Table 1.1: Fragmentation schemes and parameters in 90 and 91 MC of DELPHI

with a and b parameters and m_T the transverse mass of the created quark. It is known that c and b quarks (later noted as heavy quarks) have a harder fragmentation than the light quarks. LEP data have shown that the predictions of the LUND fragmentation function of the momentum distributions of semileptonic heavy quark decays, are too hard, i.e. the predicted momenta are on average larger than experimentally observed. The data can be described much better with the most common parametrisation of the heavy quark fragmentation, the Peterson fragmentation function [15]. In the latter scheme, the probability that a heavy hadron is produced with a value z is given by:

$$f(z) \sim \frac{1}{z(1-\frac{1}{z}-\frac{\epsilon_q}{(1-z)})^2},$$

where ϵ_q is a parameter that can be determined experimentally. In the DELPHI Monte Carlo, the LUND symmetric fragmentation function was used for light quarks u, d, s and the Peterson fragmentation function for heavy quarks b and c. The values of ϵ_c and ϵ_b that were used in the DELPHI simulations of the 1990 and 1991 data, are given in Table 1.1.

In the string fragmentation model, the production probability of a quark pair is proportional to $\exp(\frac{-\pi m_T^2}{\kappa})$, with κ the amount of energy per unit

length ($\kappa \simeq 1$ GeV/fm). This implies a suppression of heavy quark production: u:d:s:c $\simeq$ 1:1:0.3:10^{-11}. Thus heavy quarks are *not* expected to be produced in the soft fragmentation. This implies that whenever a B-meson is identified, this meson contains the initial b quark and by counting the B-mesons, one can estimate the partial width of the Z^0 resonance into $b\bar{b}$ pairs. The suppression of $s\bar{s}$ quark pairs, relative to $u\bar{u}$ pairs, is left as a free parameter in the Monte Carlo program. A default value of 0.30 is used.

- **Resonances and decays** A large fraction of the particles produced by fragmentation are unstable, and subsequently decay into the observable stable particles. Therefore, all particles with their mass, width and branching fractions are incorporated in JETSET. The properties used in the model, are taken from the Review of Particle Properties [6]. Since not all information on the different particles is known, some assumptions are made in the Monte Carlo. E.g. the decay treatment involves guesses of some branching ratios, like for B mesons, as these branching ratios are poorly known experimentally.

1.7.2 Heavy hadrons in the Monte Carlo simulation

At the Z^0 mass, $\sim 90\%$ of the produced B hadrons are mesons, $B_u(40\%)$, $B_d(40\%)$ and $B_s(10\%)$. The other $\sim 10\%$ are B baryons like Λ_b and Σ_b. The charm and bottom mesons are vector mesons (D^*, D^{**}, B^*) or pseudoscalars (D,B). All B^*'s decay electromagnetically to B. The D^* vector mesons can decay electromagnetically or via the strong force.

The ground state B and D mesons decay weakly by the emission of a virtual W boson, this process is described by spectator diagrams as shown in Fig.1.11. The lifetime of the various charmed hadrons differ significantly and have been well measured. The Monte Carlo uses the measured values. In the case of B mesons, the lifetime of the admixture of bottom hadrons produced at PEP, PETRA or LEP has been measured, but the lifetime of the separate species has not yet been measured accurately. However, the lifetime difference between the different B hadrons is expected to be significantly less than for the D hadrons. The average B lifetime has been precisely measured at LEP to be 1.47 ± 0.04 ps [76]. In the Monte Carlo, all lifetimes of B hadrons have been taken to be the same. The weak decays of the $D^{\pm}$ and D^0 are handled primarily through explicit decays which have been measured experimentally. The bottom hadrons decay to quarks and the resulting quarks fragment like a jet system. For semileptonic decays it is assumed that the spectator quark always forms a single hadron. Some semileptonic branching fractions and masses of B hadrons are given in Table.1.2 [6].

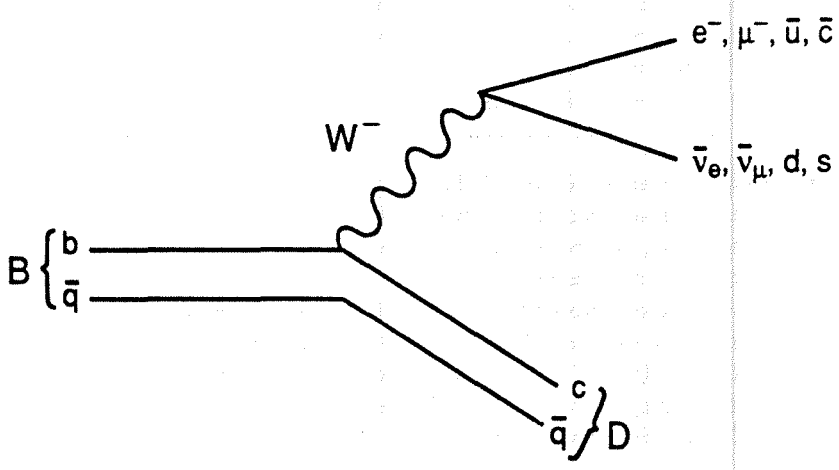

Figure 1.11: Spectator diagram for a semileptonic decay of a B meson

Inclusive semileptonic decay modes	
$BR(B \to e^{\pm}\nu_e \text{hadrons})$	$10.7 \pm 0.5\%$
$BR(B \to \mu^{\pm}\nu_\mu \text{hadrons})$	$10.3 \pm 0.5\%$
Masses	
$B^+(u\bar{b})$	5278.6 ± 2.0 MeV/c^2
$B_d^0(d\bar{b})$	5278.7 ± 2.1 MeV/c^2

Table 1.2: Some properties of the B hadrons

Part II

Experimental Setup

Chapter 2

Experimental Setup

2.1 The LEP collider

In order to test the validity of the Standard Model by determining all its parameters with hitherto unequaled precision, a Large Electron Positron collider (LEP) has been built at CERN, near Geneva. In a first stage of operation, detailed precision studies can be performed of the Z^0 resonance, requiring a centre of mass energy of $\sim$ 91 GeV. From 1996 on, the centre of mass energy will be increased to $\sim$ 170 GeV to study W^+W^- pair production. The cross section for e^+e^- annihilation as a function of the centre of mass energy is given in Fig.2.1.

2.1.1 Design

LEP [19, 20] has the shape of an octagon with rounded corners. Eight straight sections are alternated by eight arcs which have a radius of curvature of 3096 m. The tunnel housing the machine has a circumference of 26.7 km and is located under French and Swiss territory, at depths varying between 50 and 150 metres.

Electrons and positrons are accelerated in opposite direction. This is done using the same beam pipe and the same focussing and deflection magnets (dipoles, quadrupoles, sextupoles, etc ...), as electrons and positrons have the same mass and opposite charges.

The two beams can interact in 8 intersection points located in the centre of each straight section. Four of these are equipped with detectors: ALEPH,

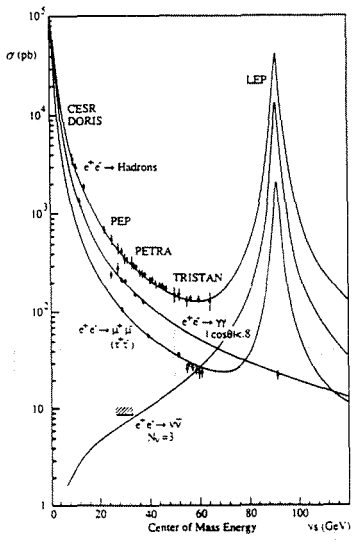

Figure 2.1: Cross section for e^+e^- annihilation as a function of the centre of mass energy

DELPHI, L3 and OPAL. Both the electrons and positrons are concentrated in 4 equidistant bunches with a length of a few cm. During the last weeks of the 1992 physics run, LEP has been operated with 8 bunches. The bunches are travelling in a beam pipe of 160 mm diameter, where a vacuum of less than 10^{-9} Torr is maintained. In the intersection regions, a vacuum of about 2.10^{-10} Torr is required to suppress interactions of the beam particles with the residual gas molecules.

The charged particles loose energy due to synchrotron radiation in the bending sections of the ring. The energy loss is proportional to the beam energy to the fourth power and to the inverse of the radius. For a beam energy of 45.5 GeV, this amounts to $\sim$ 100 MeV/particle/turn. These losses are restored and the beams are accelerated by a system of radiofrequency cavities.

The pre-acceleration of electrons and positrons takes place in different stages. First, electrons and positrons are accelerated to 600 MeV in the LIL (Linear Injection Linac), then they are injected into the EPA (Electron Positron Accumulating ring). When enough particles are accumulated (this is measured in Ampere, the current going through the ring), the beams are brought in the PS (Proton Synchrotron) where they are accelerated to 3.5 GeV. Thereafter they are injected in the SPS (Super Proton Synchrotron) where their energy is

raised to 20 GeV, and finally they are brought in LEP. When about 2 à 3 mA is accumulated in LEP and the beams are ramped to the nominal energy and brought in collision, the data taking period can start. The beam current decays exponentially $e^{-t/\tau}$ with a lifetime τ of several hours.

2.1.2 Luminosity

The number n of collisions per crossing for a given physical process with cross section σ is

$$\mathrm{n} = N_{e+}N_{e-}\frac{\sigma}{S},$$

with S the bunch cross section and $N_{e\pm}$ the number of particles in each bunch.

The event rate N per second for a given process is therefore

$$N = n_b f n = n_b f N_{e+}N_{e-}\frac{\sigma}{S},$$

where n_b is the number of bunches of each type in the machine and f the revolution frequency. The luminosity $\mathcal{L}$ is defined as

$$\mathcal{L} = n_b f \frac{N_{e+}N_{e-}}{S}, \tag{2.1}$$

such that

$$N = \mathcal{L}\sigma. \tag{2.2}$$

Typical values are $f = 11$ kHz, $N_{e\pm} = 4.10^{11}$ and the number of bunches $n_b = 4$ or 8. The design luminosity of LEP is 1.6 10^{31} cm^{-2}s^{-1}. The transverse shapes of the bunches can be described by Gaussian density distributions:

$$\rho_{\pm} = N_{e\pm}\frac{1}{2\pi\sigma_x\sigma_y}e^{\frac{-x^2}{2\sigma_x^2}}e^{\frac{-y^2}{2\sigma_y^2}},$$

with σ_x and σ_y the horizontal and vertical r.m.s. beam sizes at the intersection points. The bunch cross section is then given by

$$S = 4\pi\sigma_x\sigma_y.$$

A high luminosity implies a high intensity and a low bunch cross section (see 2.1). Bunch densities are limited by the energy loss due to the synchrotron radiation, by the magnetic field induced by the electrons and positrons in the walls of the vacuum pipe and by interactions between the two counter-rotating beams. The induced magnetic field is proportional to the current (and thus to

the density of particles per bunch) and will broaden the bunches. The beam-beam interaction is due to the attraction of the electrons in the electromagnetic field of the positrons and vice-versa. This gives rise to an increase of the betatron oscillations of the bunches and leads to instabilities of the beams.

Quadrupoles, placed a few metres from the intersection point, focus the beams to smaller dimensions. The bunch size in the interaction points is given typically by $\sigma_y = 10$ μm in the vertical and $\sigma_x = 150$ μm in the horizontal plane.

The total number of events recorded in a time interval t is given by

$$N_{tot} = \sigma \int_0^t \mathcal{L} dt. \tag{2.3}$$

The integrated luminosity is defined as $\mathcal{L}_{int} = \int \mathcal{L} dt$ and is given in events per nb or per pb[1]. Given a peak cross section of 40 nb and a peak luminosity of $\sim 7\ 10^{30}$, one expects a production rate of approximately 1000 Z^0 events per hour. The average luminosity achieved in 90, 91 and 92 was $3.2\,10^{-30}\mathrm{cm}^{-2}\mathrm{s}^{-1}$, $4.2\,10^{-30}\mathrm{cm}^{-2}\mathrm{s}^{-1}$ and $4.6\,10^{-30}\mathrm{cm}^{-2}\mathrm{s}^{-1}$, respectively. The integrated luminosity for the 1990, 1991 and 1992 runs is shown in Fig.2.2. The luminosity can be determined by the detectors themselves, by measuring the rate of a process with a well-known cross section (see equation 2.3). In LEP experiments the small-angle Bhabba scattering is used for this purpose. In the low angle[2] region, the t-channel photon exchange process of $e^+e^- \rightarrow e^+e^-$ is dominant and given by:

$$\frac{d\sigma}{d\Omega} = \frac{\alpha^2}{2s}\frac{s^2+u^2}{t^2} = \frac{\alpha^2}{2s}\frac{4+(1+\cos\theta)^2}{(1-\cos\theta)^2}$$

This cross section behaves like θ^{-4} and thus

$$\frac{d\sigma}{d\theta} \sim \theta^{-3}$$

The angular θ-distribution will peak at low angles.

The Bhabba events consist to lowest order in QED of two collinear outgoing e^+ and e^- tracks, each having an energy equal to that of the incoming beam particles. The luminosity detector therefore has to measure not only the direction of the particles, but also their energies. Hence, this detector will be composed of a tracking device and a calorimeter.

[1] 1barn = $10^{-24}\mathrm{cm}^2$

[2] Low angle = close to the beam pipe

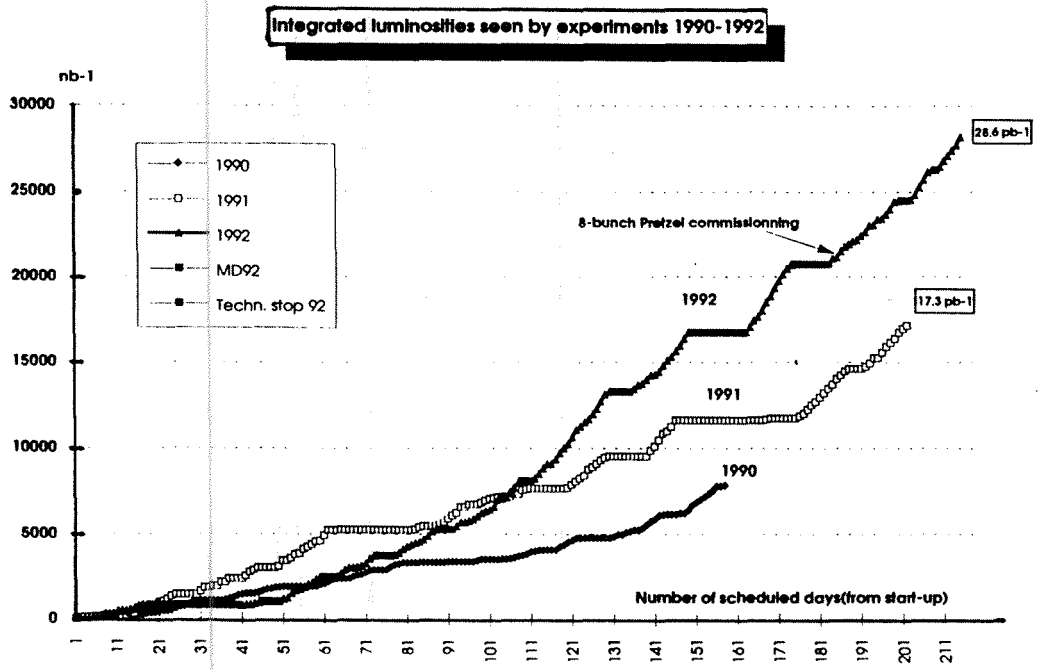

Figure 2.2: Integrated luminosity for the 1990, 1991 and 1992 physics runs

2.1.3 Machine background processes

LEP detectors are totally shielded from ambient low energy radiation from the tunnel by thick concrete walls some 13 metres away from the interaction point [21]. Therefore, machine induced backgrounds considered below, can only reach the detector through the 160 mm diameter beam pipe. The machine induced background at LEP can be divided into two categories:

- low energy photons from synchrotron radiation in the 10-1000 keV region. They can convert into an electron positron pair, give rise to random hits in the tracking detectors and complicate the pattern recognition.
- High energy $e^{\pm}$ with energies up to the beam energy. These particles are lost from the stable rotating beams in two ways:
  - by interactions with electromagnetic fields, in particular the field of the counter-rotating bunches (beam-beam interaction). These background particles have the full beam energy.
  - by interactions with rest-gas molecules. Such electrons and positrons will reach the detector if they originate mainly from two places. First, if they originate from the bending arcs and have an energy

Type of particle	Rate to experimental chamber per bunch crossing	
	without collimator	with collimator
Low energy photons		
Central detector	$4.5\ 10^{8}$	5
Forward detector	$4.5\ 10^{8}$	150
Off-momentum electrons		
to detector	$3\ 10^{-2}$	$2\ 10^{-2}$
to luminosity detector	0.2	$1\ 10^{-2}$

Table 2.1: Machine induced particle background rates (2 x 3mA, 55 GeV, nominal vacuum pressure)

1 to 2 % below the beam energy. Second, if they are generated by bremsstrahlung with the rest-gas along the last 400 metres upstream and if they have lost at least 20 % of their energy (off-momentum particles).

Those high energy particles affect the trigger rates in the detector. Also the count rate in the luminosity detectors will suffer from this kind of background.

- Muons (beam halo muons) originating from the interaction of beam particles with material, e.g. collimators, along the beam pipe. These muons traverse the detector parallel to the beam axis.

In order to keep the machine background to a minimum, a complex set of collimators has been installed near the experimental areas. The background rate with and without collimators is given in Table 2.1.

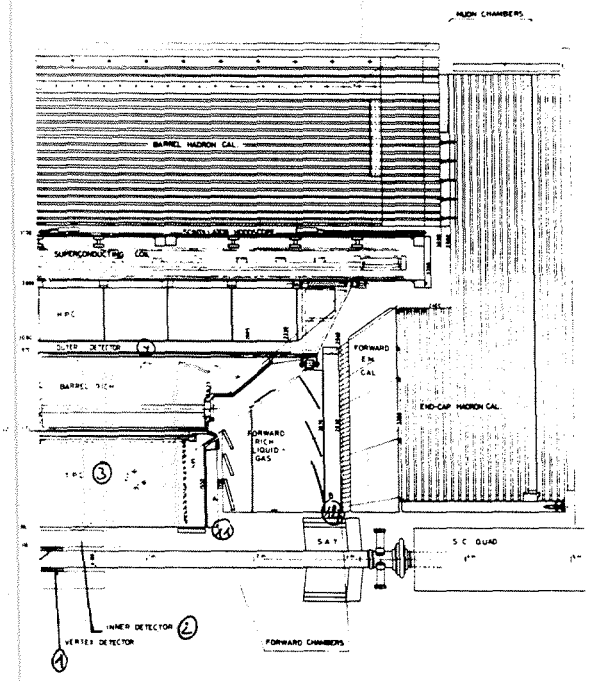

Figure 2.3: Longitudinal view of the DELPHI detector

2.2 The detector DELPHI

DELPHI [22, 23, 24], a Detector with Lepton, Photon and Hadron Identification, is one of the four detectors at LEP. The DELPHI detector is installed in a cavern 100 m below ground and is basically a closed cylinder of about 10 m diameter and length, that encloses completely the interaction region. It consists of a cylindrical section, the barrel, and two endcaps. A longitudinal and transverse view of the detector is shown in the Figs. 2.3 and 2.4. The detector is built and operated by a collaboration of 52 laboratories from all over the world.

Before describing the detector the coordinate system is defined. The DELPHI reference frame is a right handed orthogonal coordinate system with the origin in the middle of the DELPHI detector, approximately in the interaction point. The z-axis is defined in the e^- direction (the electron beam rotates anti-clockwise in LEP) and the x-axis is horizontal and points towards the centre of LEP. Points in the endcap are described by cartesian coordinates (x, y, z). In

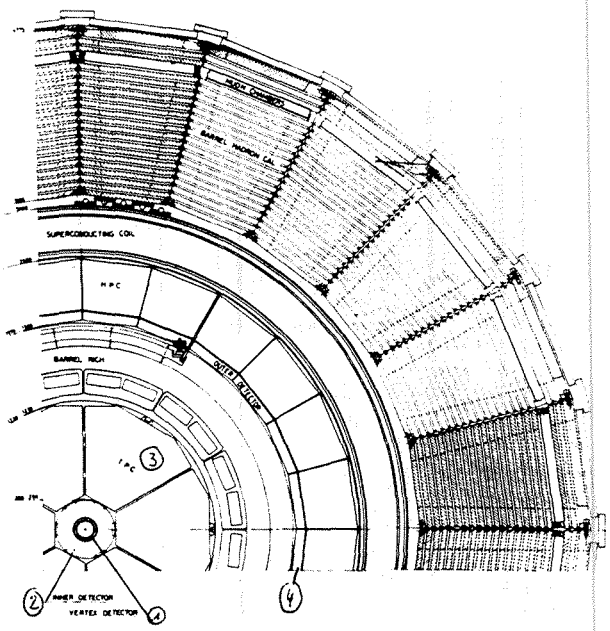

Figure 2.4: Transverse view of the DELPHI detector

the barrel region, cylindrical coordinates $(R, R\phi, z)$ are used, with

$$R = \sqrt{(x^2 + y^2)}$$

the radius and ϕ the azimuthal angle referred from the x-axis in the (x, y) plane. $R\phi$ is the product of R and ϕ and therefore the distance from the x-axis to the considered point on the circular arc of radius R. The track direction is described by spherical coordinates (θ, φ), with θ the polar and φ the azimuthal angle, defined at the perigee point[3]. The DELPHI reference frame is shown in Fig.2.5.

The apparatus is operated in a magnetic field of 1.23 Tesla, parallel to the z-axis and created by a superconducting coil with a length of 7.4 m and an inner diameter of 5.2 m. The field is produced by a single layer of NbTi conductor, carrying a current of 5000 Amperes. The longitudinal component of the magnetic field lies well within the range 12344^{+1}_{-10} G with negligible azimuthal variation. The radial component is less than 5 G.

The detector consists of various sub-components, each performing specific tasks. In particular there are:

[3]The perigee is the point of the track that is closest to the interaction point.

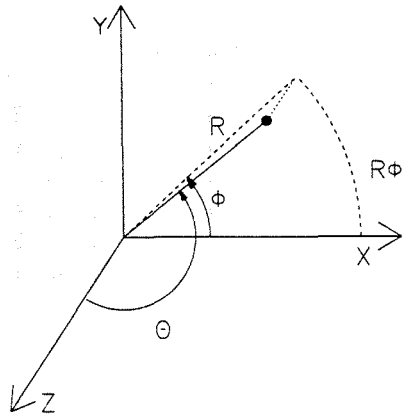

Figure 2.5: DELPHI reference frame

- tracking devices for the reconstruction of the particle trajectories, allowing a determination of the momentum and charge of charged particles;
- calorimeters for the measurement of the energy and position of charged and neutral particles;
- detectors for particle identification, for instance the Ring Imaging Cherenkov Detectors (RICH) and the muon chambers;
- luminosity monitors for measuring the Bhabha scattering rate.

The various components of the detectors[4] are discussed below. The position, momentum, energy and timing resolutions quoted below are obtained in data taking conditions, unless otherwise stated.

2.2.1 Tracking devices

All tracking devices are located inside the coil of the superconducting magnet in order to determine the momentum and charge from the curvature ρ of the particle trajectory in the magnetic field B. The transverse momentum p_t with respect to the magnetic field is given by $p_t = 0.3\rho B$ if p_t is given in GeV/c, ρ in metres and B in Tesla.

Segments of charged tracks are reconstructed by combining several measured space points in a given subdetector. Track segments of several tracking devices can be combined to reconstruct the trajectory of charged particles in three

[4] DELPHI as proposed before the upgrade

dimensions. Up to four different detectors can be used to fit the tracks. Particles in the barrel region will traverse consecutively the Microvertex Detector (1 in Figs.2.3 and 2.4), the Inner Detector (2), the Time Projection Chamber (TPC) (3) and the Outer Detector (4). In the forward region, i.e. below 45^o, information on a passing particle is given by the Inner Detector (2), the TPC (3), Forward Chamber A (11) and Forward Chamber B (14). The geometry and the intrinsic resolution of the separate components will be discussed, and then an overview is given of the function of each of them in the context of the combined tracking system of DELPHI.

The MicroVertex Detector (MVD)

is the detector closest to the interaction region [22, 25], surrounding the beam pipe. It provides an excellent $R\phi$ resolution in order to obtain very precise tracking information as close as possible to the interaction point. It covers the central region over a length of 24 cm in z, covers the angular region $37^0 < \theta < 143^0$ and consists of three concentric shells at radii 6.3, 9 and 11 cm (see Fig.2.6)[5]. Each shell consists of 24 modules with about 10 % overlap in ϕ between the modules. Each module carries four silicon microstrip detectors along z, with strips parallel to the beam. The measured intrinsic point resolution for a single track is

$$\sigma_{R\phi} = 8\,\mu\text{m}.$$

The two-track separation is

$$\sigma_{R\phi,\text{two-track}} \leq 100\,\mu\text{m}$$

The Inner Detector (ID)

consists of two concentric drift chamber detectors, surrounding the microvertex detector (see Fig.2.7).

- The jet-chamber (11.8 cm $< r <$ 22.3 cm) has 24 anode wires in the radial direction and provides a maximum of 24 $R\phi$ coordinates per track. The angular coverage is $17^o < \theta < 163^o$. There is no z-measurement. The resolution is:

$$\sigma_{R\phi} = 90\,\mu\text{m}$$

[5] Until the run of 1990, a larger beam pipe was used and the microvertex detector consisted of only two layers at 9 and 11 cm.

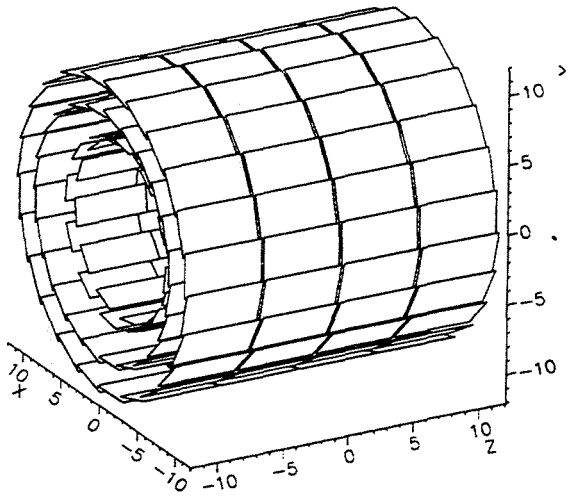

Figure 2.6: Microvertex detector: Sketch of assembly in three shells with 10% azimuthal overlap between 15^o sectors.

- Five cylindrical multi-wire proportional chamber (MWPC) layers (23 cm $< r <$ 28 cm) cover $30^o < \theta < 150^o$, where each layer has 192 anode wires in the z-direction and 192 circular cathode strips. The wires determine the $R\phi$ coordinate in a very short time, because the drift distance is small, and therefore the ID can be used in the first level trigger. Moreover, these measurements are used for resolving the left/right ambiguities of the jet-part. The cathode strips give information on the z-position, which is also used in the first level trigger. The obtained resolution on the z-determination is better than 1 mm.

$$\sigma_z < 1\,\text{mm}$$

The Time Projection Chamber (TPC)

is the principal tracking device of DELPHI, allowing three-dimensional spatial reconstruction of trajectories of charged particles. It is a drift chamber consisting of two half cylinders of 135 cm length with an inner and outer radius of 35 and 111 cm respectively. The two halves are separated by a central wall plane

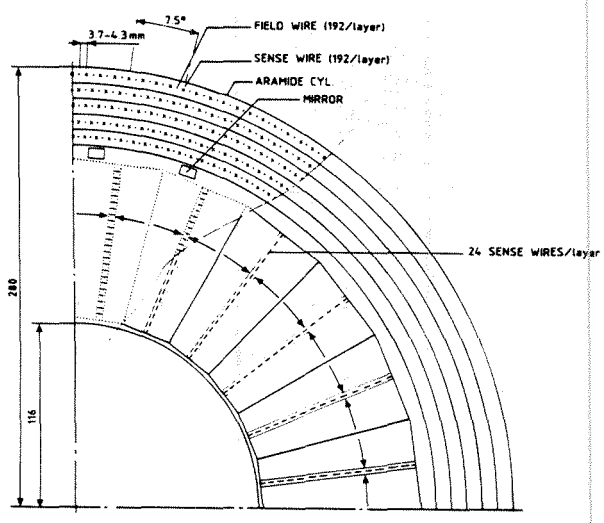

Figure 2.7: Inner detector: cross section in xy-plane.

at $z = 0$. The angular coverage is $20^o < \theta < 160^o$ if at least 3 space points are required. A charged particle traversing the sensitive volume causes ionisation of the gas. Under the action of a uniform applied electric field parallel to the z axis, the liberated electrons drift towards the endplates, where they induce a signal in the readout pads. Each endcap is divided in 6 sectors in ϕ and each sector has 16 circular cathode pad rows and 192 anode wires (see Fig. 2.8). The cathode pads are used for the determination of the R and $R\phi$ coordinate; the z coordinate is obtained by measuring the drift time to the endplate. The number of points of a particle trajectory depends on θ, with a maximum of 16 points for a track which is completely contained in the TPC.

The measured $R\phi$ resolution depends on ϕ and z and is in the range

$$\sigma_{R\phi} = 180 - 280\,\mu\text{m}$$

The z resolution is

$$\sigma_z < 0.9\,\text{mm}$$

The dimension and separation of the cathode pads specify the two-track separation that can be obtained in the $R\phi$ coordinate.

$$\sigma_{R\phi,2\text{ track}} \simeq \sigma_{z,2\text{ track}} \simeq 1.5\,\text{cm}$$

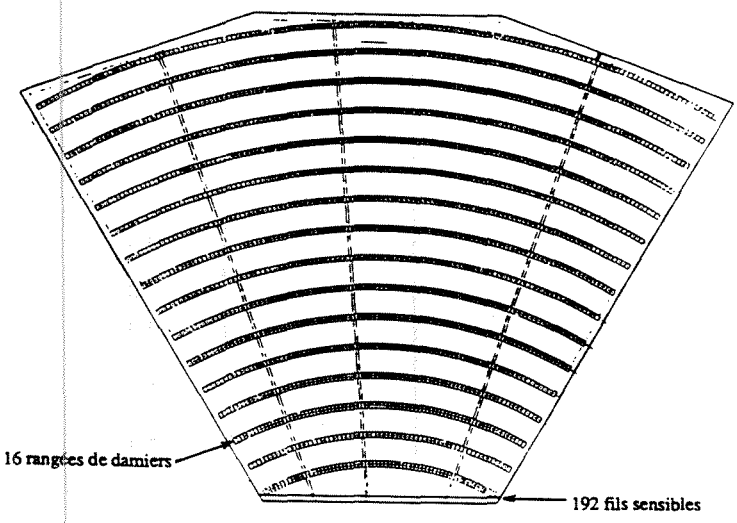

Figure 2.8: Time projection chamber: paths on the end plates

The pulse height on the sense wires is related to the ionisation energy loss of the particle over its track length. This dE/dx measurement is used for particle identification. The resolution is 5.5 % for muons at 45 GeV.

The Outer Detector (OD)

is installed at a radius of 198 cm and covers the angular region $43^o < \theta < 137^o$. It consists of 24 modules, each of them is 4.7 m long along z and contains 145 drift tubes, operating in the limited streamer mode, grouped in five staggered layers (see Fig. 2.9). The $R\phi$ coordinate is measured by the drift time in each tube, and is measured in the five layers; the z coordinate is derived from the timing signals from both ends of a tube in three of the five layers.

The resolution is

$$\sigma_{R\phi} = 110\,\mu\text{m}$$
$$\sigma_z = 4.4\,\text{cm}$$

The $R\phi$ and z information is used in the fast trigger decisions (see section 2.3), because this detector has a fast response due to the short drift distance in the tubes.

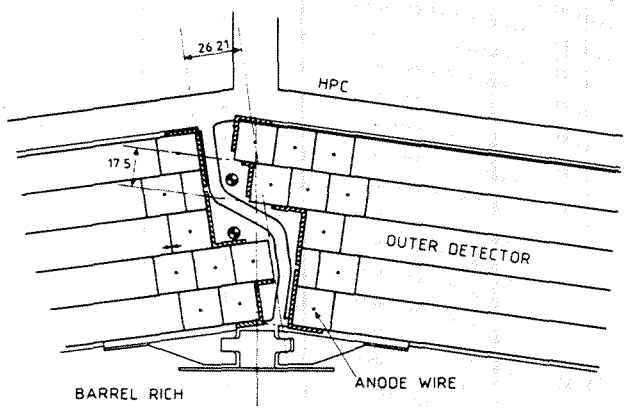

Figure 2.9: Outer detector: shape and arrangement of detector modules.

The Forward Chamber A (FCA)

is mounted on both ends, directly behind the TPC endplates, at $\mid z \mid$ between 155 and 165 cm. It covers the angular region $11^o < \theta < 33^o$ and has an inner radius of 30 cm and an outer radius of 103 cm. Each arm is built as two half discs, each half disc consists of three chambers that are 120^o rotated with respect to each other. Each chamber consists of two staggered layers of drift tubes (see Fig. 2.10). The drift tubes have the form of a rectangular parallelepiped forming square cells in the xz-plane of size 15 mm. Both outer surfaces carry a pattern of 58 mm wide cathode strips rotated by 60^o with respect to the anode wire in the centre. Points are measured in the internal coordinate system (x, u, v), defined in the plane perpendicular to the beam axis and each axis is perpendicular to the anode wire of the chambers. The axes x, u and v are 120^o rotated with respect to each other. The FCA provides per arm 2 times 3 coordinates (xx', uu', vv'), where x' is staggered with respect to x.

The obtained resolution is

$$\sigma_x = \sigma_u = \sigma_v = 300\,\mu\mathrm{m}$$

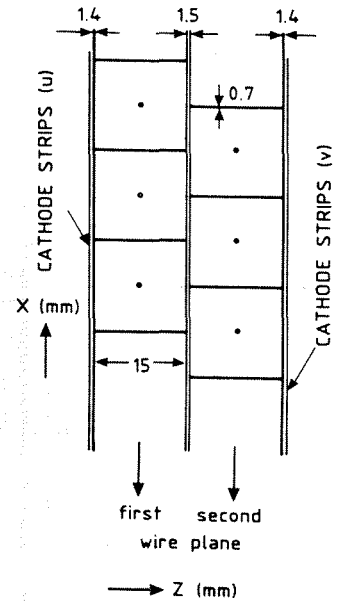

Figure 2.10: Forward chamber A: one staggered double layer.

The Forward Chamber B

is placed parallel to chamber A at $\mid z \mid$ between 267 and 283 cm ($11^o < \theta < 35^o$). Each arm is built as two half discs with inner and outer radius of respectively 53 and 195 cm. Each half disc contains 12 sense wire planes separated by cathode plates of 1 mm thickness, grouped in staggered pairs and rotated by 120° with respect to each other. Sense wires are spaced 2 cm and separated by field wires. The layout of FCB and a cross section of a half disc is shown in Fig.2.11. The FCB provides per arm 2 times 6 coordinates (xx', uu', vv') times 2.

The resolution is

$$\sigma_x = \sigma_u = \sigma_v = 250\,\mu\text{m}$$

The two forward chambers (FCA and FCB) are used in the first level trigger in the forward region.

2.2.2 Combined tracking system

DELPHI has a large number of independent tracking devices. The TPC is the main tracking device of DELPHI providing three-dimensional information. It is

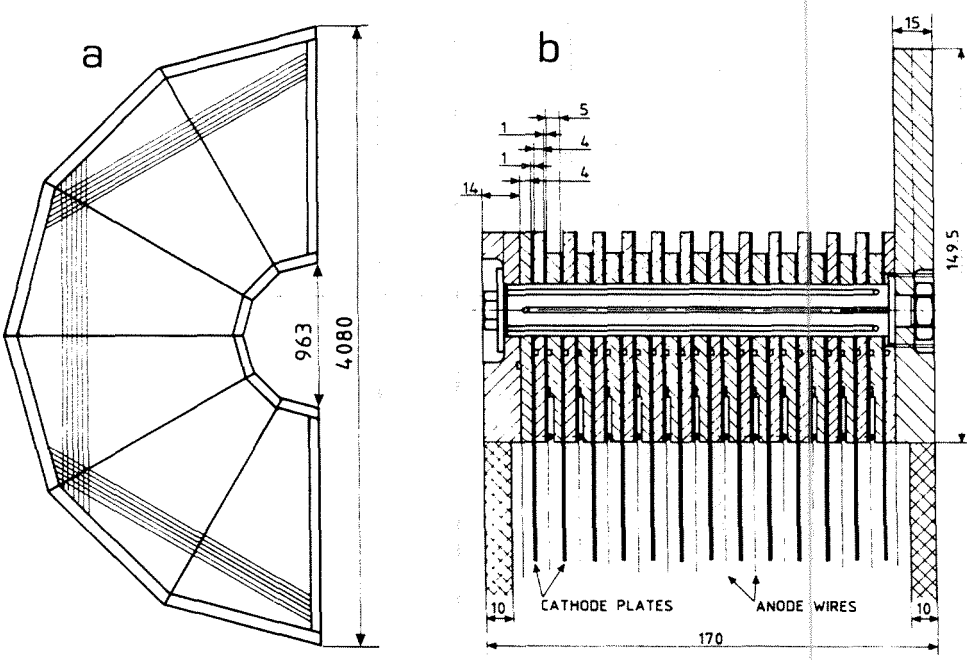

Figure 2.11: Forward chamber B: Layout (a) and cross section (b).

the main component in the track search and track fit. Adding the other tracking detectors in the track fit algorithm improves the track resolution.

Especially for high momentum tracks, like in $e^+e^- \rightarrow \mu^+\mu^-$ events, the outer detector is very useful. Its very good spatial resolution in $R\phi$ at 2 metres from the interaction point increases significantly the lever arm for the track reconstruction.

The ID provides precise measurements of the $R\phi$ coordinate, which is used to obtain a good extrapolation to the primary vertex. Together with the MVD, the primary vertex can be determined on an event by event basis. Secundary vertices from the decay of short living particles, can be reconstructed thanks to precise $R\phi$ measurement of the microvertex detector.

Below $\theta = 22^o$ and above $\theta = 158^o$, the number of TPC pads is less than 3, and below $\theta = 18^o$ and above $\theta = 162^o$, there is no pad information from the TPC. Tracks in these forward-backward directions are reconstructed using the information of the ID-jet chamber + FCA + FCB, and tracks can be reconstructed up to low angles ($\theta = 13^o$), with a worse momentum resolution. In the region of $22^o < \theta < 35^o$, the combination of TPC information with the measurements of FCA and FCB, yields a good determination of the track parameters. Due to the beam pipe, no information can be recorded below $\theta = 11^o$.

The relative positions of the different DELPHI sub-detectors are determined by using very energetic tracks, such as muon pairs and cosmic rays.

The following results for muon pairs have been obtained at 45.6 GeV:

in the barrel region (combining ID, TPC and OD):

$$\frac{\sigma_p}{p} = 0.08$$

in the forward region $20^o < \theta < 35^o$ (combining ID, TPC, FCA and FCB):

$$\frac{\sigma_p}{p} = 0.12$$

2.2.3 Scintillation Counters

The barrel region, in the angular region $41^o < \theta < 139^o$, is equipped with **Time-of-flight counters (TOF)**. They form 1 layer of 172 counters mounted just outside the solenoid. Such a counter consists of a scintillator sheet (2 cm x 19 cm x 355 cm) connected to photomultipliers on each side via light-guides. There is a dead zone of 6 cm around $\theta = 90^o$ and around the support legs of the cryostat. The time resolution is

$$\sigma_t = 1.2\,\text{ns}$$

Between the endcap yoke and the second muon chamber layer, the **Forward Hodoscope**[6] **(HOF)** is inserted. It consists of one layer of 4 quadrants, each having 28 counters (1 cm x 20 cm x 450 cm). The time resolution is

$$\sigma_t = 5\,\text{ns}$$

Scintillator detectors have a fast response and are mainly used in DELPHI for triggering purposes in the first level trigger. The TOF detector can be used to veto cosmic muons, because muons from e^+e^- interactions will arrive almost simultaneously in opposite counters of the TOF, while cosmic muons will produce two hits with a time difference of $\sim$ 20 ns. The HOF extends the muon pair trigger down to very low angles and is the only trigger that can be used for beam related halo muons, almost parallel to the beam axis, which are used for calibration and alignment of the forward detectors.

[6] A scintillation hodoscope is a system where many narrow parallel scintillator counters are used.

2.2.4 The Calorimeters

The calorimeters measure the energy deposited by the impinging particles and determine their position. They are located outside the tracking chambers, and are made of dense material (iron, lead). There are two types of calorimeters: calorimeters designed to measure the energy of electrons and photons (electromagnetic (EM) calorimeters: the shower develops due to electromagnetic interactions with the materials, i.e. mainly electron-positron pair creation and bremsstrahlung), and calorimeters dedicated to measure the energy of hadrons (hadron calorimeters: the particles interact strongly with the nucleons of the material). Experimentally the only difference in both types lies in the type of converter material that is used (lead for electromagnetic, iron for hadronic calorimeters). The electromagnetic calorimeter is located in front of the hadronic calorimeter, such that electrons and photons start showering in the EM calorimeter and are stopped. Hadrons will also start a shower in the EM calorimeter (but in a different way), but are not stopped, and reach the hadron calorimeter, where they produce hadronic showers.

The High-density Projection Chamber (HPC)

is the electromagnetic calorimeter in the barrel region. It has a radial extension from 208 cm to 260 cm and an angular coverage in θ from 43^o to 137^o. It consists of 144 separate modules with a segmentation of 24 in azimuth and a segmentation of 6 along z. There are gaps of 1 cm between the different modules. A module has a granularity of 4 mm along z, 1^o in azimuth and a nine-fold radial sampling in depth (18 radiation lengths). It consists of 41 accordion-like planes of lead wires, immersed in the sensitive gas volumes and 8 mm gas gaps. Particles that pass the HPC will produce an electromagnetic shower. Under the influence of an electric field parallel to the magnetic field, the electrons created by the ionisation of the gas, drift to the end of the module, where a proportional chamber records the spatial coordinates (R, $R\phi$), using a pad readout. The pad layout of a readout chamber, providing nine samples in R, is shown in Fig.2.12. The z-coordinate is obtained by measuring the drift time to the proportional chamber. The achieved resolution in the shower direction for test beam data is

$$\sigma_\theta = (\frac{36}{\sqrt{E}} + 2.5)\text{mrad}$$

$$\sigma_\phi = (\frac{97}{\sqrt{E}} + 10)\text{mrad}$$

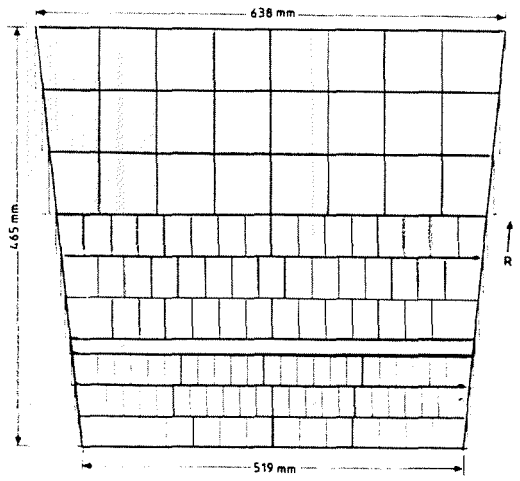

Figure 2.12: High density projection chamber: Pad layout

The measured energy resolution for a 46 GeV e^- [28] is

$$\frac{\sigma_E}{E} = 0.08$$

A scintillator is inserted in one of the HPC gaps close to the shower maximum after 4.5 radiation lengths and is used in the first level trigger.

The Forward Electromagnetic Calorimeter (FEMC)

consists of two disks with a diameter of 5 m, each containing 4532 lead glass blocks in a shape of truncated pyramids, arranged to point (almost) to the interaction point (see Fig.2.13). It covers polar angles $10^o < \theta < 36.5^o$ and $143.5^o < \theta < 170^o$. The lead glass counters have dimensions of 5 x 5 cm^2 ($\simeq 1^o \times 1^o$). The front planes of the detector are installed at $\mid z \mid = 284$ cm, and extend 56 cm in depth with 44 cm active detector, equivalent to 20 X_o.

The energy resolution for a 46 GeV e^- [28] is

$$\frac{\sigma_E}{E} = 0.05$$

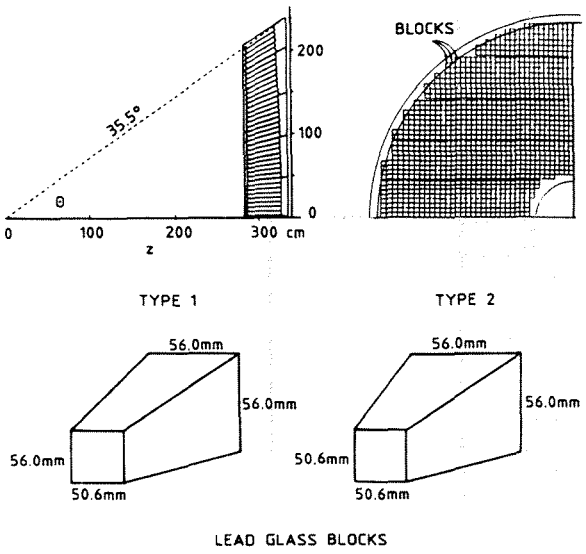

Figure 2.13: Forward electromagnetic calorimeter: layout.

The Hadron Calorimeter (HAC)

is a sampling gas detector incorporated in the magnet yoke of DELPHI. It consists of a barrel part that goes over in the endcap parts in a continuous way and covers the full region $11.2^o < \theta < 168.8^o$. The detector consists of a sandwich of iron planes and limited streamer tubes. Readout pads, glued to the streamer tubes, collect the charge induced by the crossing particle. The calorimeter has a projective geometry pointing to the interaction region.

The barrel part, placed at $r = 320$ cm, is divided into 24 sectors in $R\phi$ and a module is 760 cm long in z. The calorimeter consists of 19 iron plates of 5 cm thickness, two iron planes of 2.5 cm thickness and finally, a 10 cm thick iron plate. In total this corresponds to 110 cm iron or 6 interaction lengths. The detectors are inserted in 2 cm thick slots, the barrel has a total sampling depth of 20 layers. After 18 iron plates, there is a gap of 8 cm where muon chambers are inserted.

The endcaps consist of a big disc, inserted after FCB at $\mid z \mid = 340$ cm and has a sampling depth of 19 layers. Each endcap is segmented into 12 equal sector shaped modules, with 21 iron plates 5 cm thick. After 17 iron plates the first layer of the forward muon chamber is inserted.

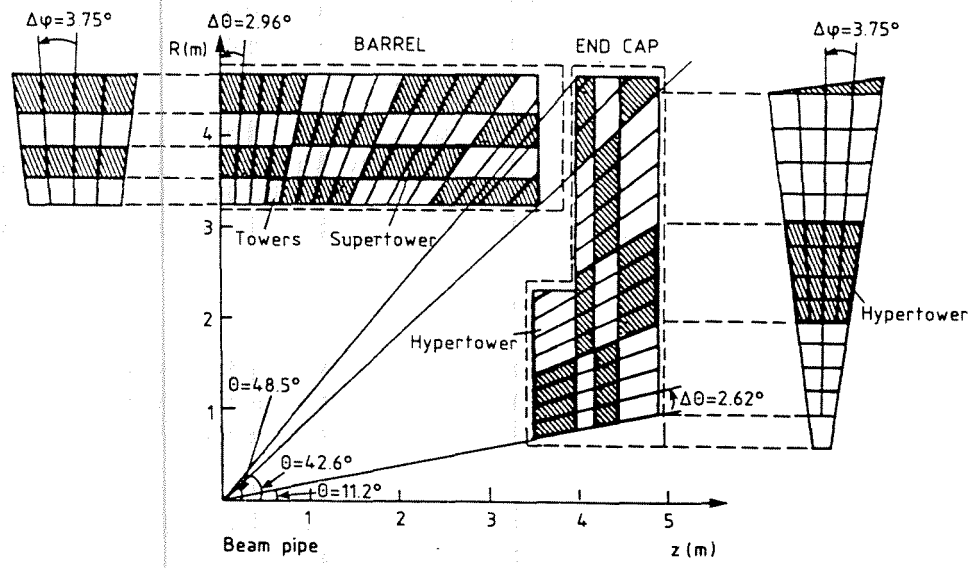

Figure 2.14: Hadron calorimeter: Tower structure of readout for the hadron calorimeter

For readout and analysis purposes, corresponding pads of sequential planes are grouped in towers. Almost everywhere there are four towers in depth, pointing to the interaction region and covering an angular region in the barrel of $\Delta\theta = 2.96^o$, $\Delta\phi = 3.75^o$ and with typical dimensions 25 x 25 x 25 cm^3 in the barrel (see Fig.2.14). The endcap towers cover a region of $\Delta\theta = 2.62^o$ and $\Delta\phi = 3.75^o$.

The achieved energy resolution is [28]

$$\frac{\sigma_E}{E} \simeq \frac{1.}{\sqrt{E}}$$

2.2.5 Particle Identification

The Ring Imaging Cherenkov Counters (RICH)

DELPHI is the only LEP detector equipped with RICHes, the barrel region is covered by the barrel RICH (BRICH), the forward region by the forward RICHes (FRICH). Here I will only briefly discuss the principle on which these

detectors are based. Only recently, one begins to understand the signals of the BRICH and to use them in analyses. Therefore, no attempt was made to use this complex detector in the subsequent analyses.

The aim is to be able to identify hadrons over most of the momentum range, using Cherenkov radiation. If a charged particle traverses a material with a velocity greater than the light velocity in that medium, it emits electromagnetic waves. At each point the particle radiates in a cone with opening angle α, given by

$$\cos(\alpha) = \frac{1}{\beta n}$$

where $\beta = v/c$ is the velocity of the particle and n is the refractive index of the medium. Once the velocity is known, it can be combined with the momentum measurement from the track detectors to obtain the particle mass.

The barrel RICH is inserted at a radius of 123 cm, between the TPC and the OD. The forward RICH is placed between FCA and FCB at $\mid z \mid = 172$ cm. More information on these detectors can be found in [22].

2.2.6 Muon Chambers (MUC)

The barrel as well as the forward regions of DELPHI [22] are covered by muon drift chambers. The barrel muon detector (MUB) has been built by Oxford University, the forward muon detector (MUF) by the high energy group of Belgium (IIHE-ULB-VUB — Université de Mons-Hainaut — Universitaire Instelling Antwerpen). Between the barrel and forward muon detector there is a dead zone for muons with polar angle between 48^o and 50^o.

The forward muon chambers (MUF)

The forward muon detector (MUF [26]) consists of two arms that cover the forward region of DELPHI. Both arms have 2 layers of chambers, one (the Inner layer) inside the yoke, behind 85 cm of iron, the second one (the Outer layer) 30 cm further, behind another 20 cm of iron and the forward scintillators. Each layer has two planes of muon chambers, the standard distances in z for the two inner planes are $\pm$ 464.05, $\pm$ 467.40 cm and the two outer planes $\pm$ 501.05 and $\pm$ 504.40 cm.

Each plane is composed of four quadrants; one quadrant consists of two orthogonal layers of 22 drift chambers each. In all there are 16 x 22 x 2 = 704 drift chambers, arranged in 16 quadrants (see Fig. 2.16).

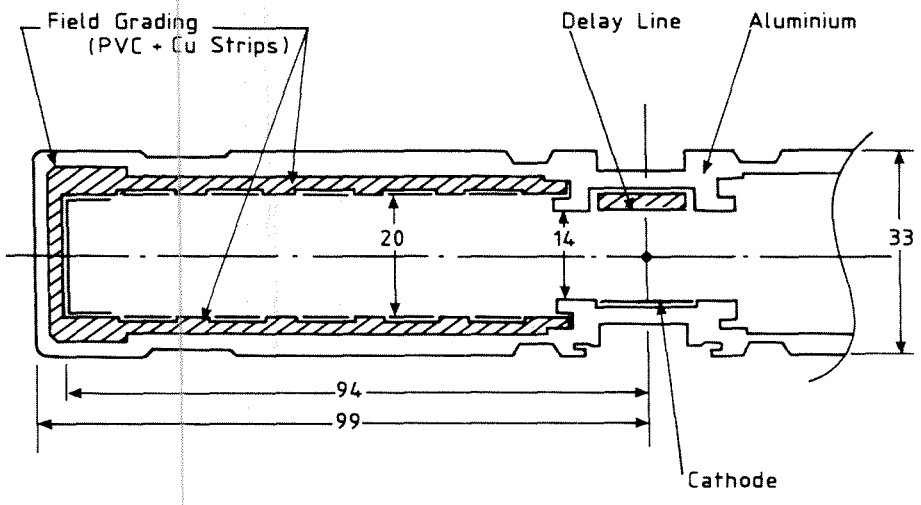

Figure 2.15: Forward muon chamber: Cross section through drift tube.

The sensitive volume of the standard drift chambers is 435.4 cm long, 18.8 cm wide and 2 cm high, with a 100 μm anode wire in the centre. The chamber is operated in the limited streamer mode. The chamber consists of four aluminium walls, two endplugs and an internal gas volume (Ar, CO_2, CH_4 and 2% i-propanol). Thin copper strips, coextruded in the PVC profile at the inside of the chambers, act as drift field electrodes (E = 700 V/cm). A flat solenoidal delay line, also glued to the PVC profile, parallel to the anode, acts as central cathode [27] (see Fig. 2.15). The two orthogonal coordinates are obtained from the drift time measurement to the anode wire and the two times at both ends of the delay line. The left-right ambiguity of the drift part is in most cases resolved using the delay line information of the crossed layer.

Typical values for drift and delay line velocity are

$$\text{drift velocity v } = 7.4\,10^{-4}\,\text{cm/ns}$$

$$\text{delay line velocity v} = 0.17\,\text{cm/ns}$$

The achieved spatial resolution both in the drift and delay line coordinate is

$$\sigma \sim 5\,\text{mm}$$

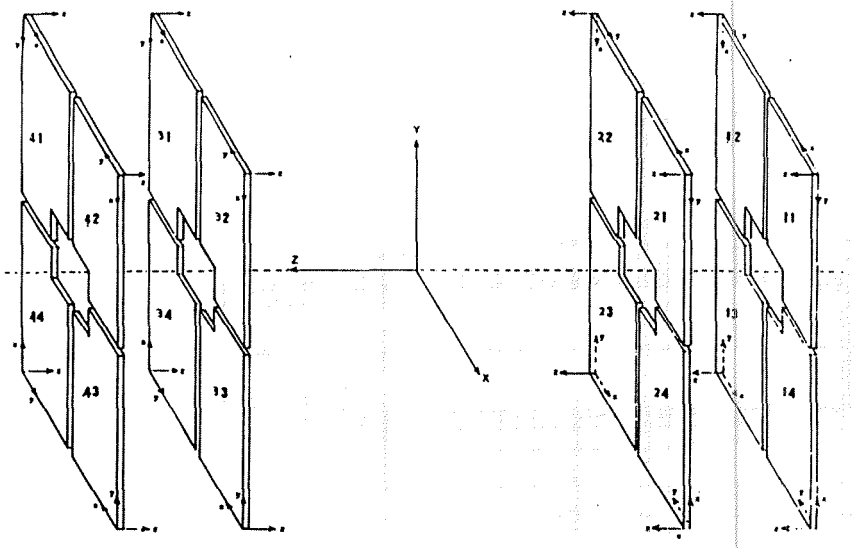

Figure 2.16: Forward muon chamber: Quadrants.

For a muon in the forward region, at most 4 layers of muon chambers can be crossed, thus leading to maximum 4 hits in the endcap. Less planes can be hit due to following reasons:

- One of the corners of a quadrant is not covered by drift chambers to allow the passage of the beam pipe.
- Between the adjacent quadrants there is an opening of 10 cm.
- Other dead spaces are due to gas and high voltage cables in the end plugs of the drift chambers.
- Drift chambers that are inefficient (e.g. due to voltage trips).

The barrel muon chambers (MUB)

The barrel muon detector is composed of three layers. The first (inner) layer is inserted after 90 cm of iron, the second (outer) and third (peripheral) layers are mounted outside the yoke, behind another 20 cm of iron. The standard radial distances from the DELPHI z-axis to the base of the inner, outer and peripheral

modules are, respectively, 445.5 cm, 479.3 cm and 532 cm. The individual drift chambers are arranged in planes with a 24-fold segmentation in ϕ, each set of modules occupying a 15° sector (Fig.2.17).

The inner module contains 14 drift chambers stacked in three layers (5+4+5). The third layer is a spare one, used in case of a defect of one of the two other layers. The outer and peripheral modules contain 7 drift chambers (4+3). The peripheral one covers the gaps in ϕ between the other two modules.

The barrel muon detector consists of 1372 proportional drift chambers, of typical volume 2.0 x 20.8 x 365 cm, with one anode wire running along the central longitudinal axis. The chambers operate in the proportional mode. The drift distance determines the Rϕ coordinate, the z-measurement is obtained using the arrival times of pulses at the end of a delay line, which is also one of the central cathode strips. Adjacent layers are staggered by half a chamber width in order to solve the left-right ambiguity of the drift time measurement.

Typical values for drift and delay line velocity are

$$\text{drift velocity v } = 4.6\,10^{-3}\,\text{cm/ns}$$

$$\text{delay line velocity v} \sim 0.5\,\text{cm/ns}$$

The achieved $R\phi$ and z resolution are

$$\sigma_{R\phi} \sim 3\,\text{mm}$$

$$\sigma_z \sim 1.8\,\text{cm}$$

Although there are 6 layers, most tracks have only 4 associated hits, namely arising from the combination Inner + Outer, Inner + Peripheral, or for some azimuthal angles, the Peripheral layer only.

Muons passing the barrel muon chambers can hit less than 4 layers because of following reasons:

- Each sector has two modules, one along the positive and one along the negative z-axis, with a gap of 12 cm between them.
- Some drift chambers are shorter to allow for the passage of cables, pipes and support structure for the yoke.
- Chamber inefficiencies

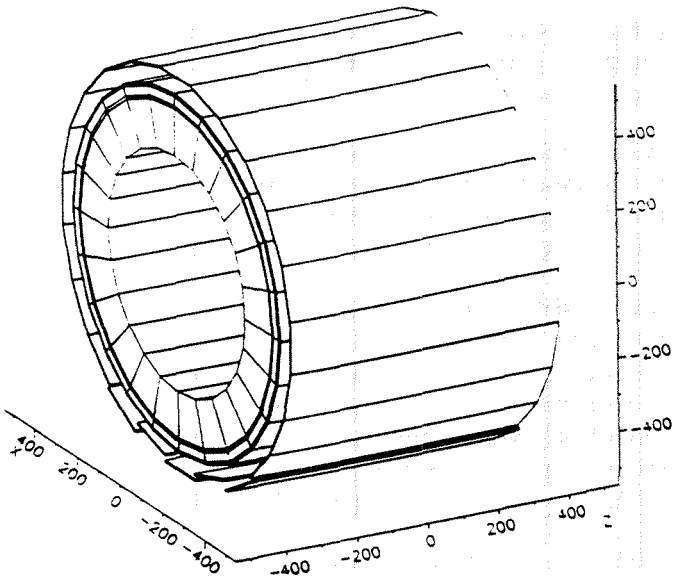

Figure 2.17: Barrel muon chamber: layout.

2.2.7 Luminosity Detectors

The primary luminosity measurement is based on the observation of small angle Bhabha scattering in the SAT calorimeters.

The Small Angle Tagger (SAT)

is installed in each arm, and consists of a tracker and a calorimeter.

The calorimeter is installed at a distance z of $\pm$ 250 cm from the interaction point, covering the angular region 43 mrad$(2.5^o) < \theta <$ 135 mrad(7.7^o) and is constructed in two half disks with a dead region of 2 cm between the disks. It is composed of alternating layers of 1 mm lead sheets and 1 mm diameter scintillating fibers running parallel to the beam axis. Layers are concentric with the beam axis. The readout is done in 8 rings, having extensions of 3 to 3.25 cm, and the ϕ-segmentation is 15^o for the four inner rings and 7.5^o for the four outer rings (Fig. 2.18). The total depth is 28 radiation lengths.

The track detector is designed to reconstruct with high accuracy the point where the charged particle enters the electromagnetic calorimeter. Both arms

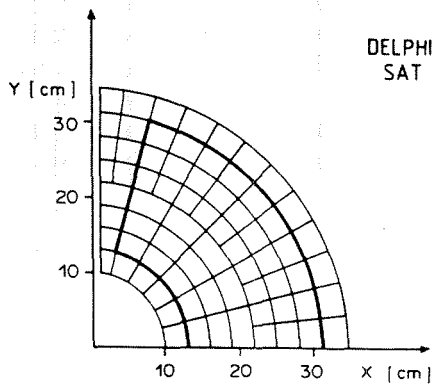

Figure 2.18: Small angle tagger: Segmentation of readout.

of the tracker have 3 planes of large area Silicon detectors at z=203, 216 and 230 cm, covering the region 43.5 mrad(2.5°) $< \theta <$ 120mrad(6.9°) . Each plane has circular strips and covers 5° in azimuth. On one side only two of the three planes are installed. On the other side, a lead mask is installed to define the inner acceptance radius for the calorimeter.

The Very Small Angle Tagger (VSAT)

is a second luminosity detector, installed in the very forward region outside of the DELPHI detector at distances of ±7.7 m. It delivers an independent measurement of the luminosity. It is a W-Si calorimeter of 24 radiation lengths, covering polar angles of 5 to 7 mrad (0.29° to 0.40°).

2.2.8 Overview of the DELPHI detector

DELPHI is an omni-purpose 4π detector, with a good tracking system and good particle identification properties. The main tracking of the detector is based upon the TPC, which delivers three-dimensional information on the passage of charged particles. Information from other tracking detectors, such as the ID, OD, FCA and FCB is combined with the TPC information to increase the lever arm of the tracks. The very forward region is covered by the ID, FCA and FCB. Precise vertex reconstruction is possible thanks to the $R\phi$ coordinates given by the microvertex detector.

Information on the identity of the particles is provided by a dE/dx measurement of the TPC and the Cherenkov detectors, installed between the TPC and the OD, and in the forward region installed between FCA and FCB. Electrons, photons and pions are identified by the EM calorimeters. Outside the coil, the hadron calorimeter measures the energy of charged and neutral hadrons. Muons will pass the HCAL and reach the muon chambers that are located in and outside the hadron calorimeter.

2.3 The trigger and data acquisition

With both e^- and e^+ beams circulating in LEP, there is a bunch crossing every 22.35 μs in each of the interaction regions. The repetition rate is thus 45 kHz. Using the machine luminosity of $\mathcal{L} \sim 0.8\,10^{30}$ cm^{-2} s^{-1} and the cross section $\sigma = 40$ nb for e^+e^- annihilation on the Z^0 resonance (91.1 GeV), the expected rate of Z^0 events, is

$$\frac{dN_{Z^0}}{dt} \simeq 0.3\text{Hz}$$

However, not only Z^0 events are of interest to the experiments, also processes like Bhabha scattering or $\gamma\gamma$-interactions. Cosmic rays and parallel muons are also recorded for calibration, monitoring and alignment purposes. This brings the rate of "interesting" events to $\sim$ 1 Hz. The main background of recorded "non-interesting" events comes from machine background events (off-momentum beam particles, beam-gas collisions, scattered γ's) and from noisy detector components, which fake real signals.

The task of selecting and recording events of interest for physics purposes is done by the trigger and the data acquisition (DAQ) system. The trigger decides whether an event is interesting or not, the DAQ reads the data buffers of the different detectors and writes all information of the detectors to a storage device (a tape of type IBM cartridge 3480).

The DELPHI trigger is designed in four levels. The first two levels are synchronous with the Beam Cross Over signal (BCO)[7], and the decisions are taken 3 μs and 40 μs after the BCO respectively. The third and fourth level are asynchronous with the BCO and are software triggers with processing times of 30 ms and 300-500 ms.

Each front-end module of a detector element (ADC's, TDC's, LTD's) has one or more front-end buffers (FEB) where the digitised data are stored. On the basis of the response time of the different detectors, they are divided in two classes:

- The fast detectors with a response time of a few hundred ns to 2 μs, such as MWPC's, cathode pads and scintillators.
- The slow detectors with a response time of 2 μs to 23 μs, mainly drift chambers.

The first level trigger (T1) only uses the data of the subtrigger module of the fast detectors. The trigger data from the subtrigger contain information on

[7] This is a signal from beam pick-up detectors placed upstream the experiments, detecting the arriving bunches of electrons and positrons.

the number of tracks or on energy deposition above a certain treshold. This information is sent, via the trigger data lines (TDL), to the central Trigger Supervisor, which produces the trigger decision function 3 μs after the BCO.

The Trigger Supervisor is composed of two units: the Trigger Supervisor Control Box (called ZEUS) and the Trigger Supervisor Decision Box (called PYTHIA), a look-up table which is programmed and loaded in the module. ZEUS is responsible for the communication between the Trigger Supervisor Decision Box and the subdetectors; it sends and receives trigger control signals to and from the different modules (sends the trigger decisions, receives a signal if the sub-detector is ready). PYTHIA, consisting of two identical modules PYTHIA 1, for the first level trigger and PYTHIA 2, for the second level trigger, produces the trigger decision.

In case of a negative decision, the data accumulation is halted and the front-end buffers are reset. If the decision is positive, a second level trigger (T2) is initiated. A decision, based on the data of the slow and fast detectors, is made by the same central Trigger Supervisor 39 μs after the BCO. If the decision is negative the present data are dumped and the system will be ready to take data at the next BCO. If the decision is positive (T2_yes), a 3.5 ms deadtime is introduced in order to free the front-end buffers of the detectors and to prepare for the next event. This implies that the experiment is blind for any event occurring during the next 200 BCO's. In Fig. 2.19 a timing diagram for the first and second level triggers is shown.

The data in the FEB's are read by the Crate Processor (CP) into the Crate Event Buffer (CEB), and subsequently put in the Multi Event Buffer (MEB). The processing of the third level trigger is done in parallel with the transfer from FEB to MEB. If the third level trigger decision is negative, the corresponding event data in the MEB will be dumped. The data in the 15 Multi event buffers (one per detector) is transferred to the Global Event Buffer (GEB). A scheme of the trigger and DAQ is given in Fig. 2.20.

The fourth level trigger runs simplified versions of pattern recognition algorithms on the event data stored in the GEB and different event types are tagged. This is done on IBM 3081/E emulators.

Once stored in the GEB, the data is transferred via an optical link connecting the detector 100 m underground to the DAQ computer at the surface, where the event is stored on a medium.

During the 1990 and 1991 data taking periods, only T1 and T2 were active. In 1992 also T3 and T4 became operational.

The trigger can be divided into classes of independent trigger components.

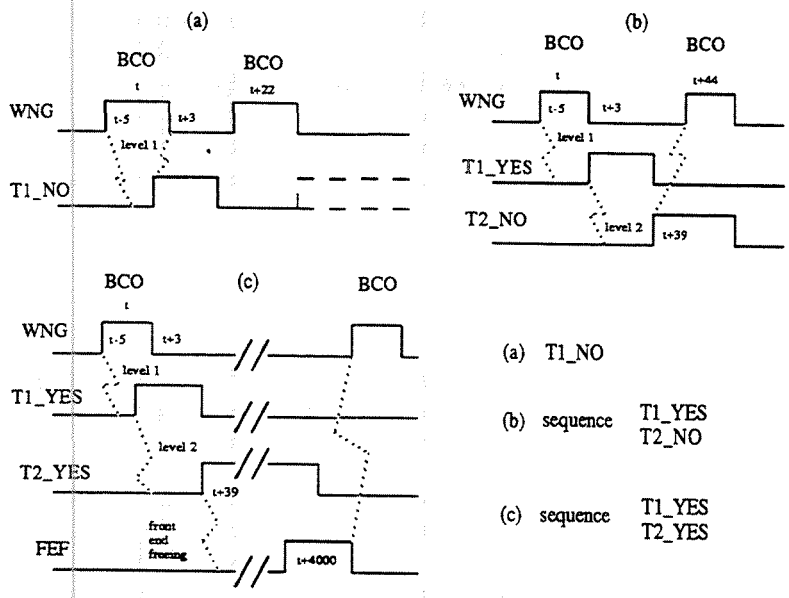

Figure 2.19: Timing diagram of first and second level trigger of DELPHI.

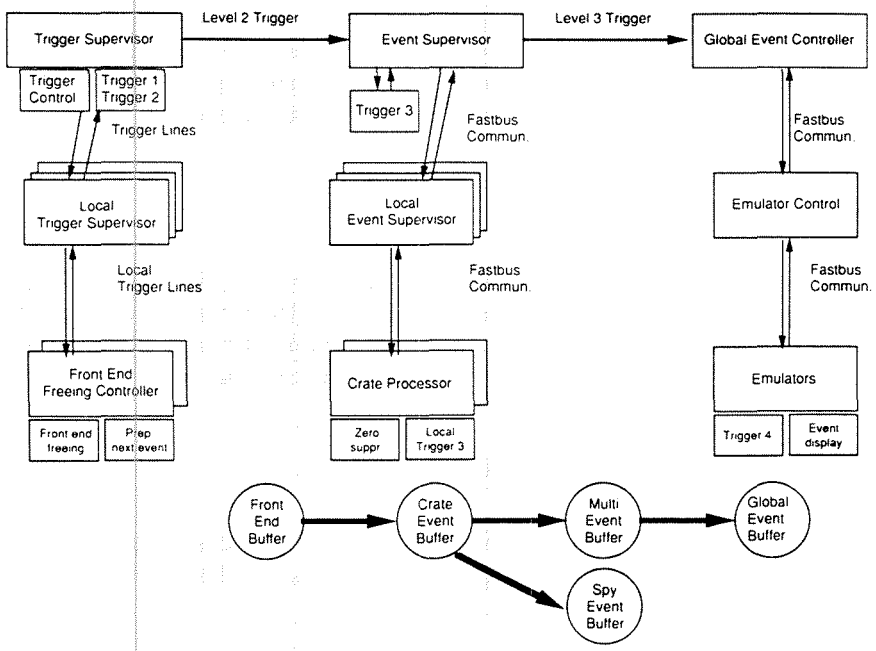

Figure 2.20: Architecture of the readout system.

This is done by grouping the signals according to their origin, e.g. signals from tracking devices. The main trigger components are "track", "muon", "electromagnetic energy", "hadron energy" and "bhabha". In addition, a special cosmic ray trigger, based on the TOF counters, can be set for calibration purposes. The different TDL signals of the components are described very briefly. It is given as an illustration and for more complete and detailed information the reader is referred to ref.[29].

The track trigger

corresponds to a combination of detector signals that have a high probability to be due to charged particles. It can be split in two independent components: the barrel track trigger and the forward track trigger.

The Inner and Outer detectors are used in the first and second level barrel trigger and cover the $42^o < \theta < 138^o$ region. A first level trigger is formed by requiring a correlation between ID and OD sectors. At second level the OD track multiplicity signals (a requirement of 3/4 out of the 5 chamber planes to be hit within a plank) is used in conjunction with the ID to construct the final TDLs. At second level the TPC also provides a barrel trigger.

FCA and FCB contribute to the forward track trigger in the polar region $20^o < \theta < 43^o$. In the first level, for each wire orientation in FCA, groups of four wires are formed which are correlated with corresponding wire groups in FCB. For the second level trigger reconstructed points are used.

The muon trigger

The detectors participating in the muon trigger are TOF, HOF and the muon chambers. TOF and HOF are used in the first level trigger, the muon chambers in the second level trigger by requiring a certain number of hits within a sector or quadrant. In 1990 only the forward muon trigger was active.

The electromagnetic energy trigger

The first level barrel trigger is provided by the HPC scintillation counters. The second level trigger is based on the pulse heights from the 128 pads per module, arranged in 6 groups for the trigger.

The forward/backward first and second level electromagnetic trigger is based on the FEMC. The trigger gives the number of superblocks with energy deposi-

tion above two thresholds. A superblock consists of 16-32 leadglass blocks. The high treshold is typically[8] 2.5 GeV, the low treshold around 1.5 GeV.

The hadron energy trigger

The calorimeter is segmented for trigger purposes in 24 segments in ϕ and 6 in θ in the barrel and 2 in θ in the forward region. The HAC contributes with the same TDLs to the first and second level trigger. The total energy deposition is compared with different energy thresholds (0.5, 2 and 5-7 GeV).

The Bhabha trigger

Bhabha events are triggered by requiring a coplanar energy deposition of at least 11 GeV in the forward and backward SAT. The SAT is also used in a single arm trigger by asking for a minimum energy deposition of 30 GeV in one of its arms.

The VSAT trigger is positive if an energy deposition of more than 30 GeV is found in opposite modules.

In 1990, and part of 1991, also a trigger component using NIM electronics (B1 trigger) was implemented which treated signals from the scintillators (TOF, HPC trigger layer and HOF) and the wire chambers (ID, OD and FCA/B).

During the 1991 run, for a luminosity of $\mathcal{L} \simeq 5\ 10^{30}\ \mathrm{cm}^{-2}\ \mathrm{s}^{-1}$ the first level trigger rate was 400 Hz, the second level trigger rate 4 Hz. In 1992 T3 was implemented with the aim of maintaining the data logging rate below 2 Hz [30].

[8] the thresholds can be selected according to noise and background conditions.

2.4 Data analysis

The data recorded by the Data Acquisition System (DAS) are converted to physical quantities by a complex reconstruction program DELANA (this is termed: processing of data). Besides this software package, there are two other packages that are common to all DELPHI data users. The main packages used are:

- DELSIM, a DELphi SIMulation package, generating physical particles and using Monte Carlo methods to simulate their behaviour when traversing the detector. The comparison between Monte Carlo and real data is used in different stages of the analysis. E.g. the efficiency of certain cuts will be estimated from the Monte Carlo data.
- DELANA, a DELphi ANAlysis package, converts the raw data (pulseheights, space points) to physical quantities, e.g. momenta, energy, vertices.
- DELGRA, a DELphi GRAphics package, showing a three-dimensional picture of the detector and the space points, energy depositions, tracks of the particles of the event.

2.4.1 DELSIM

DELSIM [33] is the Monte Carlo simulation program of the DELPHI detector. It consists of three different parts:

- the Monte Carlo event generator,
- the simulation of the interactions of each particle with the detector material,
- the signal response of each sub-detector.

The generator inside DELSIM is chosen according to the physical process one is studying. The process $e^+e^- \rightarrow q\bar{q}$ is generated by the LUND generator LUEEVT of JETSET 7.2 or 7.3 (see 1.7.1). The final state partons are calculated by the LUND Parton Shower model [17, 35] or the Matrix Element model [36]. The Lund string fragmention model combines the final partons into hadrons.

Once the final state particles are generated, each particle is tracked through the detector, taking into account the inefficient and dead zones. The interaction

with the material is simulated at every stage. The following processes are considered: Compton scattering, pair production, bremsstrahlung, positron annihilation, δ-rays, photon conversion, nuclear interaction and absorption, multiple scattering and the decay of short lived particles.

When the particle enters the sensitive volume of a sub-detector, the response of this detector is simulated, i.e. the hits or showers are determined and those points are converted into the response of the electronics. During the tracking and sub-detector simulation, DELSIM extracts information from a database which contains the geometry, position and material of each detector volume.

The final result of DELSIM is stored in the same ZEBRA[9] bank format as the "raw data". The same reconstruction program DELANA is subsequently run for data and Monte Carlo.

2.4.2 DELANA

DELANA is the DELPHI event reconstruction program. It reads the "raw" data of the different sub-detectors and produces track parameters (curvature, positions), vertices and energy depositions, by applying search and fit algorithms on these raw data.

Structure

The pattern recognition is embedded in a data structure called TANAGRA [32]. It defines a well defined structure VETBAS (VErtex and Track Basic Structure) for storing track and vertex information in a format independent of the various program modules. The relationship between the various processing stages in the pattern recognition and the data stored in the VETBAS structure, is shown in Fig. 2.21 and described below.

- Each sub-detector produces Detector DATA (TD). These data are stored in a form that is as much as possible sub-module independent; they are usually space coordinates and pulse height signals after discrimination and calibration.
- The TD's are input to the local pattern recognition, which produces track elements (TE). This step is done on the level of the sub-detector. A TE element will contain kinematic information ranging from point coordinates

[9] ZEBRA is a system which allows a dynamic creation of data structures at execution-time and is able to manipulate these structures.

to impulse vectors, depending on the type of detector. (For the muon chambers the TE's are the three-dimensional hit points in the different layers.)

- Track search processors group the TE's into candidate track strings (TS). This is done globally for the Track Elements of all sub-detectors. On the level of TS's ambiguities can exist, one TE can belong to different strings (TS).
- One or a set of TS's are submitted to a full track fit to resolve ambiguities and provide fitted track parameters. The remaining set is a set of Tracks (TK).
- Vertex search and fit processors group tracks that are possibly from the same vertex, into Bundles (TB).
- Finally a fit of the bundles is carried out to resolve ambiguities and provide the final vertices (TV). The resulting parameters are the vertex position and the track parameters at the fitted vertex.

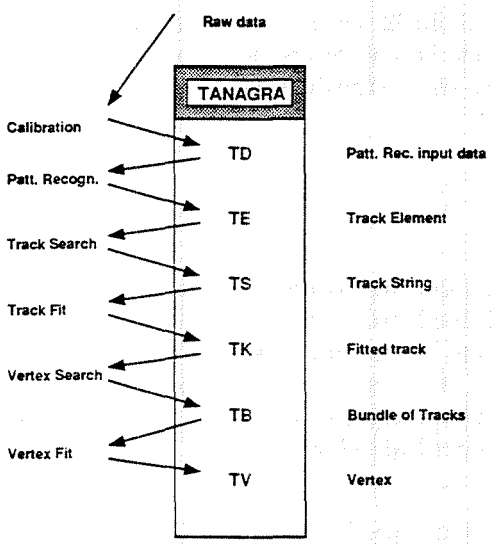

Figure 2.21: Tanagra Structure

The mass identification

Once the pattern recognition is finished, all detectors with separate mass identification processors are called (e.g. EMMASS, see chapter 3) and the results are

included in the data for the appropriate track. The mass identification provided by the individual detectors is then collected and analysed by a global processor to give a final mass assignment to the tracks. In practice, the mass identification from DELANA is not often used in the analyses, but separate routines of mass identification, being run on DST level (see below), have been developed to identify the particles. The detectors used in the mass identification are:

- the muon chambers MUB and MUF in combination with the extrapolation of the tracks to the muon chambers to discriminate muons from pions;
- the HAC and the Combined Calorimetry, also to discriminate muons from pions;
- the HPC and FEMC to identify photons, electrons, minimum ionising particles and hadrons;
- the TPC provides a dE/dx measurement used in electron identification;
- the RICHes are able to identify electrons, pions, kaons and protons in certain momentum intervals.

DST

The DST (Data Summary Tape) is extracted from the VETBAS data structure to save space and to provide a faster access to the data. Only the most important information about the tracks and particle showers is kept, such as momenta, energies, charges, track lengths, deposited energies in the calorimeter, etc... The 1990 data consists of 786 cartridges with the raw data, TANAGRA structure and DST of the events. When only the DST information is written on the cartridges, 38 cartridges remain.

Most physics analyses start from the physical quantities written on the DST.

2.4.3 DELGRA

DELGRA [34] is an interactive display program that visualises the detector response of an event. It is used for checking the detector performance and for checking some analyses; e.g. in the search for the Higgs boson, the events that remain after the application of a selection procedure, are examined visually. A hadronic event containing one high p_t muon is visualised in the xy view in Fig.2.22 and in the xz view in Fig.2.23.

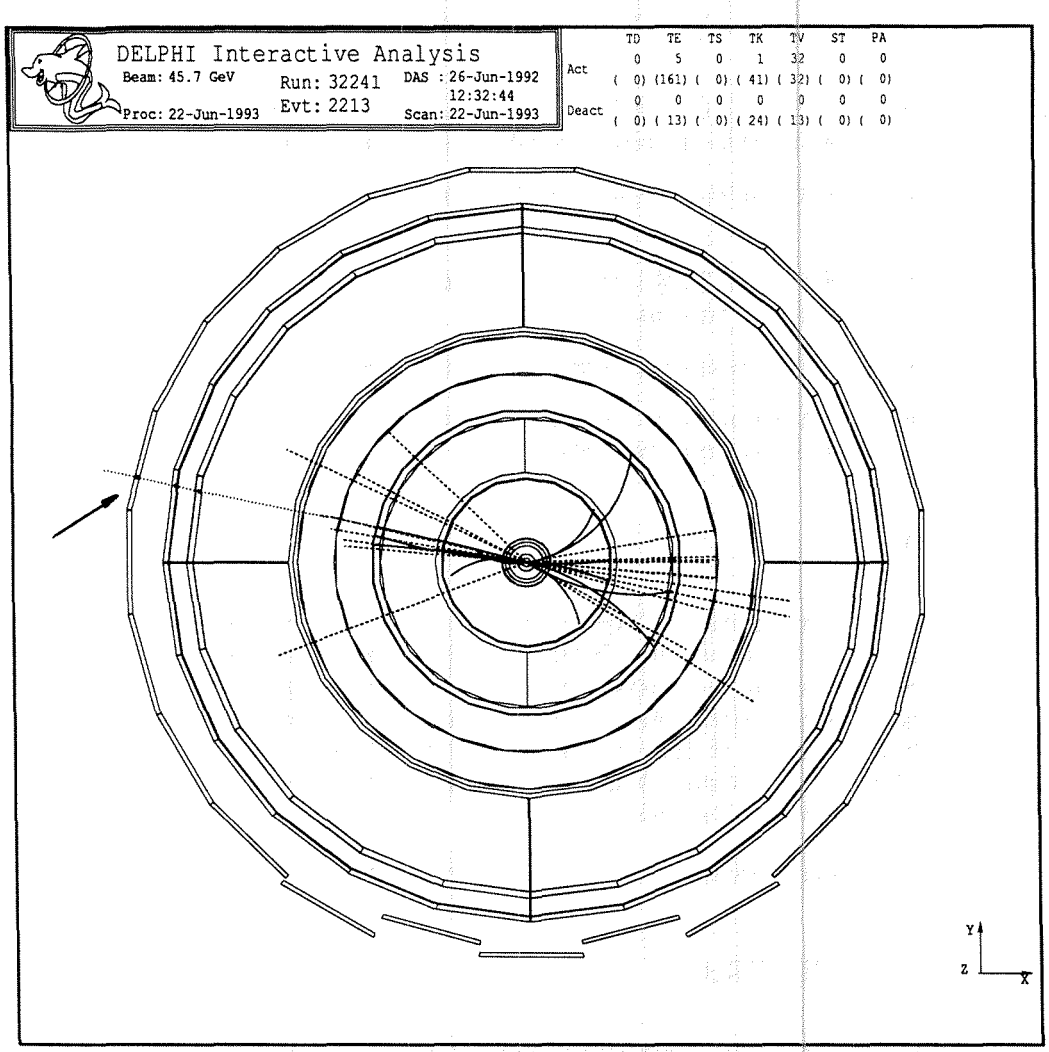

Figure 2.22: Hadronic event in xy view

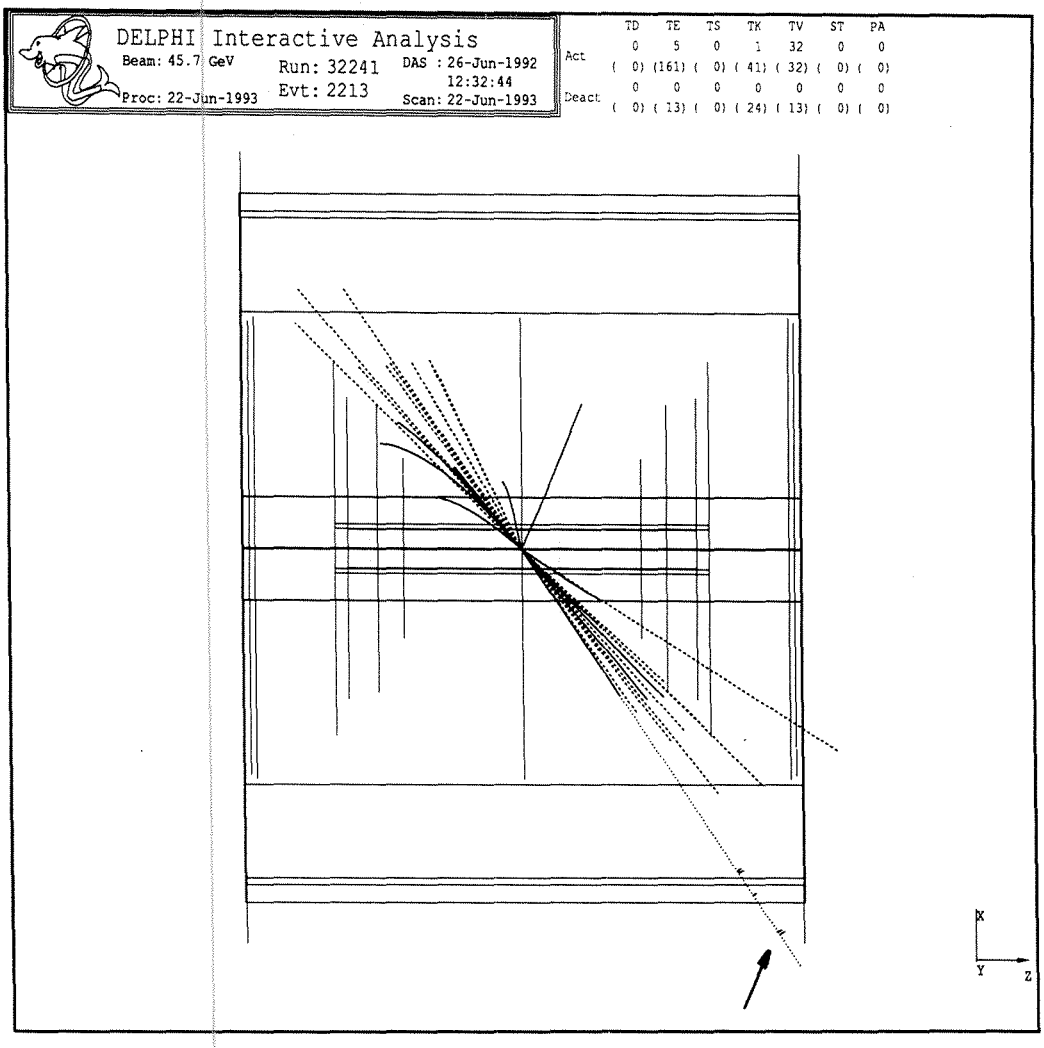

Figure 2.23: Same hadronic event in xz view

Part III

Analysis of inclusive b quark events

Chapter 3

Muon identification in DELPHI

Muons are minimum ionising particles with a lifetime of 2.197 10^{-6}s. Therefore energetic muons do not decay inside DELPHI and reach the outside of the detector. Muons leave a track in the tracking chambers, deposit a small amount of energy in the electromagnetic and hadron calorimeters and give space point hits in the muon chambers located in and outside the hadron calorimeter. In contrast to the two track topology of muon pair events, hadronic events contain about 20 charged particles and the muon signal has to be disentangled from other tracks. The hadron calorimeter, which consists of $\simeq$ 1 m of iron, stops most of the latter ones. Non-muons deposit their energy before or within the HAC, whereas muons of energy above 2-3 GeV will reach the muon chambers. However, still a variety of processes exists by which background signals appear in the muon chambers. They can be classified in the following categories.

- "Sail-through" refers to contamination from hadrons that pass through the $\simeq$ 1 m depth of the calorimeter iron without interacting. The probability that a particle has not yet interacted at a penetration depth x in the iron is given by $P(x) = e^{\frac{-x}{\lambda}}$ where the interaction length $\lambda \simeq 16.8$ cm for iron. The first muon planes are inserted in the barrel after 90 cm, thus 5.36 interaction lengths, corresponding to a sail-through probability of 0.5 %. The probability that a hadron reaches the second plane of muon chambers (110 cm iron) without any interaction is 0.14 %. In practice, the probability is higher due to particles passing through cracks near module boundaries in the iron.

- Secondary particles, produced by a hadron that interacts in the iron and exit the calorimeter within the multiple scattering cone, is termed "punch-through". The multiple scattering cone is inversely proportional to the momentum.

- Finally, kaons and pions can decay in flight to muons, which may be detected in the muon chambers and confused with a "prompt" muon. With the term "prompt", muons from the decay of a heavy (b or c quark) meson are meant. In simulations of $q\bar{q}$ events, 18 % of the muons are "non-prompt" muons.

Muon chamber hits from all three processes may either be wrongly identified as muons, or wrongly associated to genuine muon tracks in the tracking chambers, degrading their fit quality.

The identification proceeds by fitting tracks extrapolated from the centre of DELPHI, to hits seen in the muon chambers. By requiring good associations we seek to separate genuine muons from the above mentioned backgrounds. The chi-squared per degree of freedom for MUB and MUF muons (full line) and non-muon (dashed line) tracks is shown in Fig.3.1.

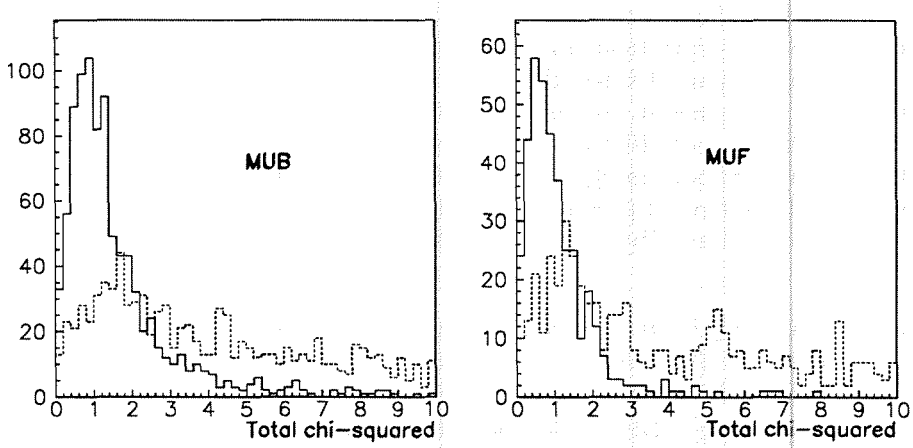

Figure 3.1: Total χ^2 per degree of freedom in MUB (left) and MUF (right). Muons are shown by the full line, non-muons by the dashed line.

An additional method to distinguish muons from hadrons is to require hits outside the calorimeter iron. Indeed, both barrel and forward muon detectors have their inner layers of chambers inserted in the body of the HAC. Punch-through particles will have a tendency to register hits here, and yet not to traverse the remaining ~ 20 cm of iron to the outer chambers. The number of outer planes hit by muons (full line) and energetic non-muons(dashed line) is shown in Fig.3.2.

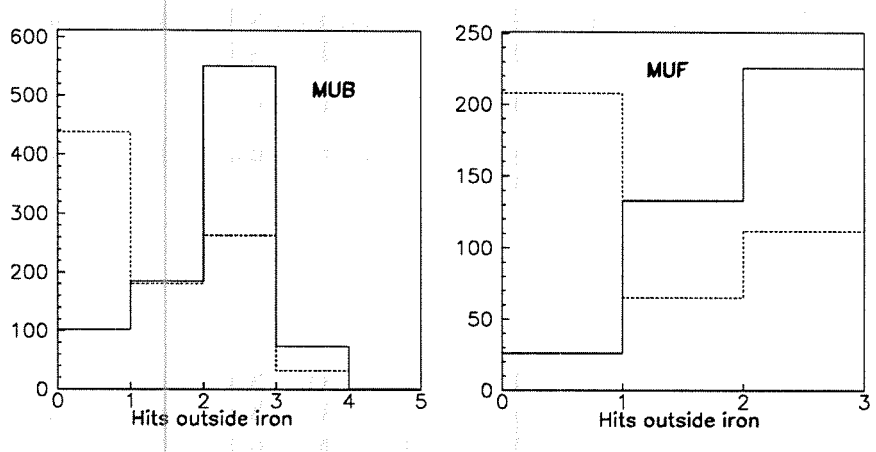

Figure 3.2: Number of hits outside iron in MUB (left) and MUF (right). Muons are shown by the full line, non-muons by the dashed line.

The muon chambers are not the only detectors in DELPHI that can be used for identifying muons in jets. The hadron calorimeter responds differently to hadrons and muons. Hadrons deposit more energy in the HAC, the deposition has a wider transverse profile and they are less penetrating, i.e. the energy is located in the first layers of the HAC. The latter feature is the one used in a muon identification algorithm based on the HAC: the module PXHAID [42] performs a muon identification on the basis of the energy deposition in the last two layers (of the four) of the HAC. The efficiency of the algorithm in a hadronic environment is around 50 % and the muon purity of the sample is around 65 %. The same module can also perform a VETO based on the energy deposition in the 4 layers. Especially in combination with the muon identification based on the muon chambers, this routine is applicable when either a very loose muon identification is useful (such as in J/ψ studies) or when a very pure sample is required (muon chambers + HAC veto). An upgrade of the HAC (a better

segmentation of the readout) is foreseen to be installed during the shutdown of 1993 and will improve the identification properties of this detector. In the muon identification algorithm described below, only the muon chambers are used, not the HAC veto.

The identification of muons can be treated in four steps:

- the extrapolation of central tracks through the calorimeters to the muon chambers is done in the extrapolation package EXX;
- A fit of the muon chamber hits to the extrapolated tracks is done in DELANA via the mass identification routine EMMASS;
- the muon blocklet on the DST is refitted in MUCFIX;
- specific criteria are applied to optimise the signal to noise ratio in hadronic events; this is done in MUFLAG.

3.1 Extrapolation

The tracks which have been reconstructed in the central tracking detectors are extrapolated through the electromagnetic and hadron calorimeters to obtain a prediction of the impact point of the track in the muon chamber planes. This is done by the EXX package in DELANA. Energy loss is taken into account, measurement errors of the tracking are propagated, and the effect of multiple Coulomb scattering on the hitpoints is calculated, i.e. the variances and covariances. It is important to notice that the multiple scattering is not introduced by changing the track direction step by step.

Energy loss parametrisations of muons in lead (electromagnetic calorimeter) and iron (hadron calorimeter) are used. In all other regions and material of the detector the energy loss is neglected (notably in the coil and in the cables). A detailed description of the package is given in [37].

3.2 EMMASS

EMMASS, a module inside DELANA, fits the tracks seen in the central tracking detectors of DELPHI to the space points produced by the muon chambers. A full description of the module can be found in [38]. When the DELANA processing is done, i.e. all hits and tracks are reconstructed, EMMASS is activated. The EMMASS procedure executes the following steps.

- The module loops over all tracks that have been extrapolated to the muon chambers. All reconstructed muon chamber hits (TE's) in a region close to the extrapolated track are collected and will be considered as a possible association. A TE element is classed as close to the extrapolated track if the following quantity R is less than 50 for MUB and less than 200 for MUF [1].

$$R = \left(\frac{(T1_{\mathrm{ex}} - T1_{\mathrm{muc}})}{\delta T1}\right)^2 + \left(\frac{(T2_{\mathrm{ex}} - T2_{\mathrm{muc}})}{\delta T2}\right)^2 \qquad (3.1)$$

  Here the coordinates $T1$ and $T2$ denote Rϕ and z in the barrel region and x and y in the endcap region. The subscript ex refers to the extrapolation, muc to the muon chamber hits. The errors $\delta T1$ and $\delta T2$ are the extrapolation and measurement errors added in quadrature. The extrapolation errors are given on 2 (MUF) or 3 (MUB) muon chamber reference surfaces and are calculated in the extrapolation package.

- For each track with one or more associated TE's, a χ^2 is calculated. It is constructed from the measured hit points ($R\phi$ and z coordinates in the barrel and x, y coordinates in the endcaps) , the errors in the muon chambers and the predicted impact point plus direction (θ, φ) together with the covariance matrix of the track, which takes into account the propagated measurement error and the multiple scattering. Both the extrapolated track and the measured points are adjusted until the best match is found.

  The space points that give the best match with the extrapolated track are chosen. The best match is defined in terms of the lowest χ^2 per degree of freedom. If the χ^2 per degree of freedom is higher than 100, one layer is dropped and the fitting procedure is performed again. If this yields no improvement, another layer is dropped. If no more layers can be dropped the best of the previous results is kept.

- EMMASS proceeds on a track by track basis. The same physical hit in the muon chambers can be assigned to more than one track. These hits with multiple associations are termed "ambiguities". If all tracks have been processed, EMMASS looks for such hits and an algorithm is applied to assign the track the hit belongs to. The best association is defined as the solution with the highest number of associated layers. If two solutions exist with the same number of associated layers, the track with the best χ^2 is chosen. A hit, belonging to e.g. two tracks, will be flagged by a 1 on the track which has the best association. The same hit on the losing track will be marked by a 0, but this track is not refitted without the ambiguous hit and the χ^2 of the track still contains the contribution of the losing hit.

[1] The latter cut has also been set to 50 for the DELANA_C processing of 1992 data.

The tracks that have muon hits associated by the former procedure, will have a "muon blocklet" on the DST. Such a blocklet contains the EMMASS fit information and the following quantities can be retrieved:

- the number of associated layers;
- the EMMASS χ^2;
- the number of degrees of freedom for the χ^2 fit, i.e. twice the number of associated layers;
- the residuals in $T1$, $T2$, θ and φ between the extrapolated and fitted tracks in the plane of the muon chambers at the layer closest to the interaction point. Also the extrapolated track errors are given at that surface.
- the muon chamber χ^2_{muc}. This is the sum of the layer χ^2_{lay} of the associated layers and is defined as:

$$\chi^2{}_{\mathrm{muc}} = \sum_{\mathrm{layers}} \chi^2_{\mathrm{lay}} = \sum_{\mathrm{layers}} \frac{(T1_{\mathrm{fit}} - T1_{\mathrm{muc}})^2}{\sigma^2_{T1_{\mathrm{muc}}}} + \frac{(T2_{\mathrm{fit}} - T2_{\mathrm{muc}})^2}{\sigma^2_{T2_{\mathrm{muc}}}}$$

  The subscript 'fit' refers to the fitted track. The muon chamber χ^2_{muc} takes into account the contribution of the space points. The extrapolation χ^2_{ex} takes into account the contribution of the impact point of the extrapolated track at the muon chambers. The muon chamber χ^2_{muc} and the extrapolation χ^2_{ex} sum to the total χ^2.

$$\chi^2 = \chi^2_{\mathrm{muc}} + \chi^2_{\mathrm{ex}}$$

- the hit pattern, i.e. a sequence of associated layers to the same track;
- for each associated layer the fitted and measured coordinates $T1$ and $T2$ and the measurement errors of the coordinates $T1$ and $T2$;
- for each associated layer the layer chi-squared;
- for each associated layer a flag indicating whether, in case of ambiguities, the hit has been assigned to the track or not.

3.3 MUCFIX

3.3.1 Introduction

EMMASS is a general purpose procedure, run centrally inside DELANA and intended as a starting point for all analyses involving muons. However, not all

analyses have the same requirements on background rejection and identification efficiencies. E.g. a track in a di-muon event will be identified as a muon if this track has an EMMASS association. In a hadronic environment, this muon requirement is too loose and the tagging of b-events through their semileptonic muonic decay mode requires additional muon identification criteria. Even different analyses in the semileptonic b-physics cannot use the same muon tag. E.g. J/ψ studies demand high efficiencies, whereas lifetime measurements need a high purity muon sample.

One would expect that putting appropiate cuts on the EMMASS chi-squared and hit patterns should be enough to construct the various tags and obtain the different purity and efficiency requirements. This is not the case. The philosophy of dropping "bad hits" was first introduced in the PXMUID muon identification algorithm [41] and is also used in MUCFIX. During the EMMASS fit, a muon chamber hit is assigned to a central track by a very loose association criterium (3.1) . Since in most of the cases more than one hit is assigned to a central track, it happens that one "bad" hit degrades the χ^2. Dropping a hit by a user defined criterium and refitting the track without that hit can be done in MUCFIX. Dropping such bad hits will improve the signal to background ratio. The severity of the definition of a "bad hit" depends of the analysis one wants to perform.

Another argument for refitting tracks on the DST through MUCFIX is the fact that the DELANA processing is never perfect. Bugs in the DELPHI track fitting and extrapolation and some systematics (e.g. offsets in hit reconstruction) are often discovered after the processing and can now be corrected on DST level. It is clear that those effects should be corrected prior to the muon hit association.

Also the assigned errors on the DST can be changed inside MUCFIX to obtain the correct resolution. Monte Carlo can be tuned to the data by introducing inefficiencies and mapping the MC errors to the data. After all corrections are made, MUCFIX repeats the EMMASS fit with cuts set by the user.

3.3.2 MUCFIX performance

The inputs to MUCFIX are the existing DST muon blocklet, the identifier of the track to which the blocklet is associated and a set of steering flags. MUCFIX outputs the refitted blocklet. MUCFIX redoes the complete extrapolation of the track to the muon chambers by using the perigee information of the track. This is a set of track parameters plus error matrix, which are obtained from a fit to the hit points recorded in the central tracking detectors, at the closest approach of the track to the origin. A complete description of MUCFIX can be found in [39].

User Features

The user can tune and perform cuts on the DST muon blocklet information before the refit is done by MUCFIX.

1. **Error scaling** The resolution of the barrel muon chambers is about 3 mm in the $R\phi$ and 1.8 cm in the z coordinate. For MUF the resolution is about 4 mm in the drift coordinate and 5 mm in the delay line coordinate. Resolution plots for 1991 muon pairs are shown and discussed in appendix A. The assigned resolution of the muon chambers, can be checked by examining the χ^2 probability distributions, PROB(χ^2,n). It is defined as

$$PROB(\chi^2, n) = \int_{\chi^2}^{\infty} \chi^2(z; n) dz,$$

with $\chi^2(z; n)$ the χ^2 distribution with n degrees of freedom. It is thus the probability for obtaining in a new minimisation with similar measurements and the same model, a higher value for χ^2. The errors of the DELANA processing and the Monte Carlo are not always well tuned. This results in a non-uniform probability density distribution. Furthermore, the fit distributions in the simulation are too optimistic and need to be degraded to match the data distributions. Therefore it is possible to multiply the nominal errors in MUCFIX by a given factor prior to refitting. Both the delay and anode line errors can be tuned independently. The χ^2 probability distributions for 1991 DELANA_E muons in di-muon events in MUB and MUF before (upper) and after (lower) MUCFIX processing are shown in Fig.3.3. The errors are adjusted until a reasonably flat χ^2 probability distribution is obtained. The peak at low probabilities is due to non-gaussian tails in the residuals.

   The tuning of the Monte Carlo data to the real data is illustrated in Fig.3.4, which show the total χ^2 distributions for MUB and MUF 45 GeV/c muons in Monte Carlo (full line) and 1991 data (data points).

   The nominal errors in the data and Monte Carlo and the chosen scales for $R\phi, z, x$ and y are shown in Table 3.1 for the 1990 and 1991 processing.

2. **Dropping Ambiguities** If certain hits belong to several tracks, EMMASS applies an algorithm to decide which track the hit most likely belongs to, but the returned χ^2 of the tracks contains the contribution of this ambiguous hit. MUCFIX allows the tracks with losing ambiguities to be refitted with the ambiguous hit removed. The decision of what constitutes a losing ambiguity can be re-decided inside MUCFIX.

   The association of muon chamber hits to central tracks is illustrated by the following figures. In simulated hadronic events 94.5% of the genuine

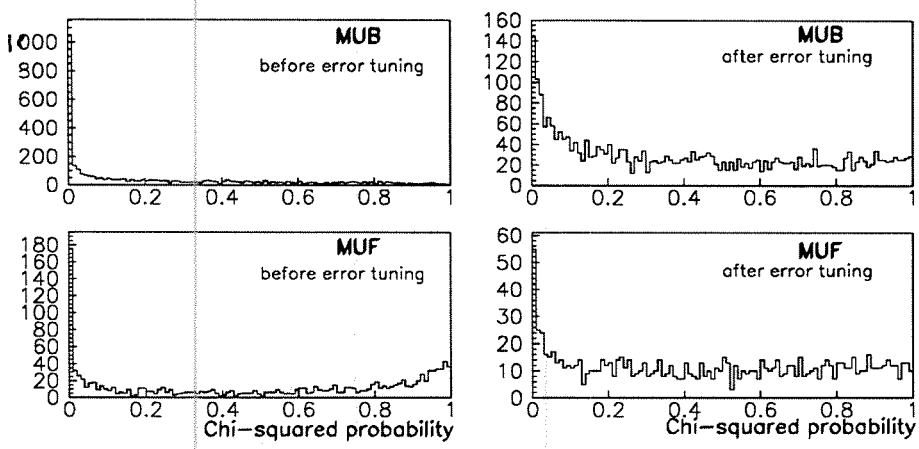

Figure 3.3: Probability distribution of χ^2 in MUB and MUF before (left) and after (right) MUCFIX corrections.

Year	Coordinate	Assigned Data Error	Assigned MC Error	Scale for Data	Scale for MC
1990	$R\phi$	0.5	1.2	0.70	0.35
	z	2.5	2.4	0.65	0.75
	Anode	1.0	1.0	0.80	1.25
	Cathode	2.0	2.0	0.40	0.75
1991	$R\phi$	0.35	0.5	0.90	0.80
	z	2.0	2.4	0.90	1.00
	Anode	0.5	0.5	0.90	0.70
	Cathode	1.0	1.0	0.50	0.73

Table 3.1: Assigned errors (in cm) and chosen scales in the 1990 data, final hadronic processing and the 1991 data delana_E processing. $R\phi$ and z are the anode and delay line errors in MUB, anode and cathode are the anode and delay line errors in MUF.

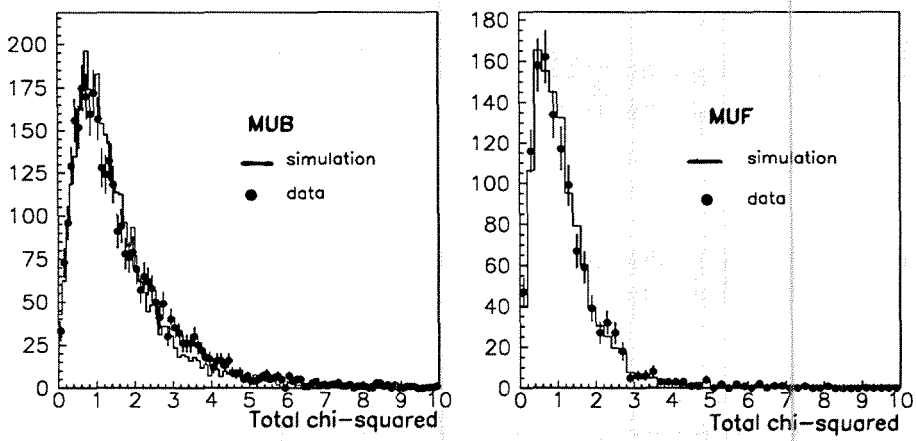

Figure 3.4: Total χ^2 distribution per degree of freedom in MUB (left) and MUF (right).

Year	MUB	MUF ECA	MUF ECC
1990	1.0 %	4.7 %	4.7 %
1991	1.1 %	13.1 %	5.7 %

Table 3.2: Layer inefficiencies for 1990 and 1991 measured with respect to the MC.

muons in MUB and 92.5% in MUF have associated muon blocklets, this percentage being only 3% in MUB and 8.5% in MUF for background tracks. After ambiguity resolution, 93.5% for MUB and 90.5% for MUF of the genuine muons have associated muon blocklets, for background tracks this is 2.4% in MUB and 4.1% in MUF. If a track contains one losing ambiguity, then in 95% of the cases for MUB, 99% of the cases for MUF, all the associated hits to that track are ambiguous and the track will be removed as a muon candidate.

3. **Dropping Bad Layers** Tails are present in the χ^2 distributions of the real data. These are due to bad hit points. Such a bad hit can come from nearby background processes or badly measured coordinates. These tails can be eliminated by masking the bad hit points having an individual layer χ^2_{lay} above a certain cut value and refitting the track with those hits removed. The number of associated layers per track is reduced, but in hadronic events this is compensated by a much better χ^2 discrimination between signal and background.

4. **Layer inefficiencies** In practice, when a muon traverses a muon chamber, there is a chance that a hit will not be registered (voltage trip, dead regions). This inefficiency is taken into account in MUCFIX for the Monte Carlo by assigning a layer inefficiency percentage to each layer. This inefficiency is calculated by fitting the associated layer distribution of the data to the Monte Carlo and is assumed to be layer independent. This fitted layer inefficiency for MUB and MUF in 1990 and 1991 is given in Table 3.2. For the MUF an endcap dependent inefficiency was introduced, since during the 1991 run Endcap A (ECA) was suffering from a hardware readout problem. The associated layer distribution for 1991 muon pairs in MUB and MUF, before and after layer inefficiencies corrections, is shown in Fig.3.5. The histogram is the MC, the points are the data.

   In the muon identification, described below, larger inefficiencies are used because of the perturbation to the associated layer distribution of the data by the bad layer dropping.

   In the barrel region an additional global inefficiency is used, because a complete sector in MUB can be dead due to voltage tripping and therefore

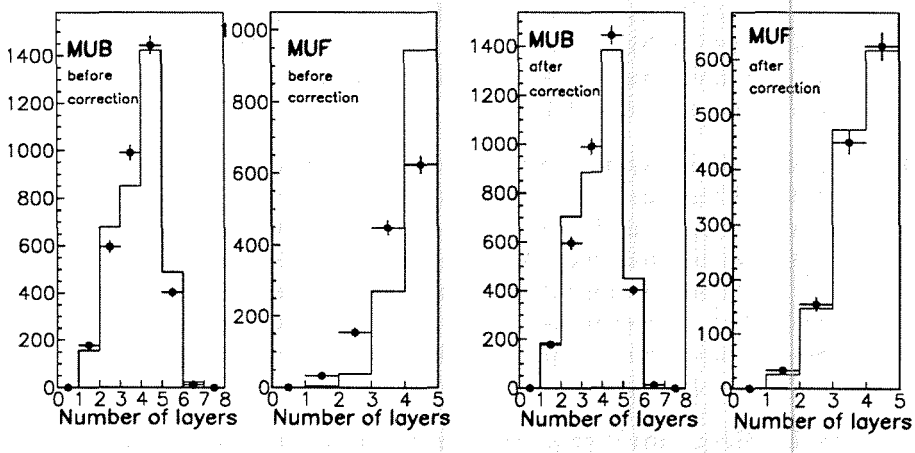

Figure 3.5: Associated layer distribution in MUB and MUF before (left) and after (right) inefficiency correction. The points are the data, the histogram is the MC.

radial tracks will occasionally register no hits at all.

1990 : 2.6%

1991 : 1.1%

Systematics

Several sources of systematic errors have been found in the 1990 and 1991 data sets and have been cured in MUCFIX. I mention them briefly below. A detailed description of them can be found in appendix B.

1. Error in $R\phi$ extrapolation (1990,1991) in MUB
2. Error in z extrapolation (1990,1991) in MUB
3. MUB T_0 shift (1990,1991)
4. Badly calibrated Delay Lines (1990) in MUB
5. Quadrant and endcap alignment (1990) in MUF
6. Smearing of MUF Monte Carlo hit points (1990, 1991)
7. Bug in Track Errors in MUF (1990,1991)

3.4 MUFLAG

MUFLAG is a routine for identifying muons in DELPHI. The routine uses tracks extrapolated from the central detectors to the muon chambers and the data in the barrel and forward muon chambers. It starts from muon information available on the DST and allows for these data to be refitted in a way suitable for the tag. The identified muons in the event are flagged. It was developed for the analysis of 1991 hadronic data and designed for the identification of muons in jets. It owes much in philosophy to the PXMUID algorithm [41], the algorithm used for 1990 and the first 1991 analyses.

3.4.1 MUFLAG structure

Here, the logic of the MUFLAG [40] algorithm is sketched.

1. For each event the user calls MUFLAG, specifying which tag type the routine is to use. At present there are three options: Standard tag, Tight tag and Loose tag. (See next section for details)

2. For each tag type, MUCFIX is initialised with different refit options. For example, a Tight tag will have a more stringent definition of what constitutes a bad hit than a Loose tag. Thus MUFLAG will refit tracks under conditions suitable for a specific tag philosophy.

3. Each track with a muon blocklet is refitted in turn by MUCFIX, using the tag specific tunes and settings. All points are used in the refit, including those which EMMASS judged to be losing ambiguities. For Monte Carlo events, the layer and global inefficiency options are not enabled at this stage [2].

   The result of the refit overwrites the existing blocklet for those tracks successfully refitted; tracks producing an error in the refit keep the original blocklet; tracks which fail the refit are discounted from further consideration. (This may happen when all the layers are dropped as 'bad hits', or no combination of layers is found which satisfies the cuts set inside the fitting routine.)

4. All the refitted tracks in the event are then examined for ambiguities. If degenerate hits are found, an algorithm is applied to decide which track the hit belongs to. An ambiguity resolving routine is supplied within MUFLAG, but it is possible for the user to employ other logics. The routine supplied in MUFLAG to resolve ambiguities uses the same algorithm as the one applied in EMMASS. The track with the greatest number of associated layers wins the hit; if this procedure does not uniquely select a track, the global fit χ^2 is considered.

   The result of these decisions is flagged within the provisional blocklet, and tracks with losing ambiguities are marked for a further refit. If all the hits on a track are losing ambiguities, then that track is eliminated as a muon candidate.

5. A second refit, this time without the losing ambiguous hits, is made for those tracks requiring one. In addition to tracks with such degenerate

[2] This is because inefficiencies introduced by MUCFIX to the Monte Carlo are governed by a random generator. As MUCFIX refits each track separately this could lead to inconsistencies in the handling of ambiguities.

hits, all potential muons in Monte Carlo events will be refitted again, this time with the activation of layer and global inefficiencies.

The results of this second refit are treated as in the first, and final refit muon blocklets are produced.

6. From the information in the refit muon blocklets, tag variables are constructed. These may be the χ^2's, number of associated layers, residuals etc. already existing in the blocklet, or more complicated functions of these, devised by the user.

7. According to the tag type, cuts on these variables are made for each candidate track. Those passing are flagged as muons to the user.

More detailed information on the MUFLAG algorithm can be found in [40].

3.4.2 Tags and Performance

Samples

Different samples of muons and non-muons were used for tuning and developing the algorithms and for measuring their performance. In this section the different samples used for this purpose are described. For all sets of the 1990 and 1991 data, A well operating TPC, forward chambers, barrel and forward muon chambers are required. All 1990 data and MC samples are taken from the processing with DST version 240, the 1991 data and MC samples are taken from the DELANA_E processing (DST version 270).

- **$\mu^+\mu^-$- sample**

  Muon pair events are selected according to an identification in HAC and HPC or FEMC in order not to bias the muon sample. Vertex and acolinearity cuts were made to eliminate cosmic muons and τ pair events [43]. Two charged particles, both having momentum above 15 GeV/c, are required. After runselection 3098 events are left in 1991 and 1686 events in 1990. This sample forms a pure muon sample with a mean momentum of the muons of 45 GeV/c and is used for tuning the muon chamber errors of data and MC and for studying the layer inefficiencies.

  In the muon pair simulation, 15973 events were used for the 1991 simulation and 3789 for the 1990 simulation.

- **$\tau^+\tau^-$- sample, 1 versus 3 prong events**

In $\sim$ 24 % of the τ events one of the τ's decays to a single charged track while the other decays to three charged non-lepton tracks. The 4 tracks were required to come from the interaction region, have a momentum above 1 GeV/c, and one of them has an isolation angle greater than 155^0. The three tracks opposite the isolated track is a pure non-muonic sample of mean momentum 12 GeV/c. In 1991, after runselection 1078 events are left, in 1990 317 events are left.

- **K^0_S Events**

  The decay mode of the $K^0_S \rightarrow \pi^+\pi^-$ is another sample of non-muons. The selection was made for the 1991 data only, by searching for two track vertices with an effective requirement on the opening angle of the tracks to reject photon conversions. After runselection 3514 events remained. The assumed pions are of mean momentum $\sim$ 5 GeV/c.

- **Hadronic Events**

  A sample of $\sim$ 30 000 hadronic events in data and Lund Parton Shower Monte Carlo was selected by standard hadronic cuts. Those passing the runselection and having a track with a momentum above 3 GeV/c and with an associated muon blocklet inside the muon chamber acceptance, were isolated. The mean momentum of the selected tracks was $\sim$ 7 GeV/c. In addition, a kinematic cut of 0.6 GeV/c was made on the transverse momentum of the track with respect to the reconstructed jet axis, as to bias the sample towards prompt muons. With this cut, the muon sample purity on MC after the EMMASS association was found to be $\sim$ 50%. On this sample, the fitted distributions were studied, the tunings were considered and the MC-data agreement was checked. If all tunings seemed satisfactory, the performance of the tagging algorithm was determined on a larger sample of Monte Carlo events.

Present MUFLAG Tags

The three tags at present provided within MUFLAG are called 'Standard', 'Tight' and 'Loose'. These have been developed with a hadronic environment in mind. The Standard tag is intended to provide mid-range, well understood efficiencies with little contamination, suitable for analyses such as the measurement of $\Gamma_{b\bar{b}}$, $A^{FB}_{b\bar{b}}$ etc. In the analyses described in this work, the Standard tag will be used for all muon identification. The purpose of the Tight tag is to yield high purity samples, useful for lifetime measurements. The Loose tag has the premium on efficiency, but still with acceptable backgrounds, to be used for J/ψ, ψ', etc ...searches, or perhaps in combination with a veto from the HAC.

In this section, the data samples, the logic and components of each tag are described. The data and Monte Carlo distributions of the key variables are presented. The error tunings for the 1990 and 1991 data have been redone with respect to the "official" MUFLAG version (the one of 1-8-93). Also another χ^2 will be used in the Standard (and Loose) MUB tag than in the official version. It was necessary to do this in order to have a good tagging rate, after the incorporation of the bug-fixes of the extrapolation package. For the standard cuts of the MUFLAG package, the reader is referred to ref.[40].

The Standard and Loose tags use the same refit options, and the final cuts are such that the Standard tag is a subset of the Loose tag. In the refit, bad hits are dropped according to a $\chi^2_{\text{bad hit}}$, which is for MUB:

$$\chi^2_{\text{bad hit}} \equiv \left(\frac{R\phi_{\text{fit}} - R\phi_{\text{muc}}}{\sigma^{R\phi}_{\text{muc}}} \right)^2 \tag{3.2}$$

For MUF this variable is:

$$\chi^2_{\text{bad hit}} \equiv \left(\frac{x_{\text{fit}} - x_{\text{muc}}}{\sigma^{x}_{\text{muc}}} \right)^2 + \left(\frac{y_{\text{fit}} - y_{\text{muc}}}{\sigma^{y}_{\text{muc}}} \right)^2 \tag{3.3}$$

For MUB and MUF data the cut is made at $\chi^2_{\text{bad hit}} > 10$, which implies a layer inefficiency in the Monte Carlo of 4.4% (1991) for MUB and 12% and 23.7% for endcap A and C respectively. This layer inefficiency is the previously mentioned feature of MUCFIX, whereby a layer is assigned a certain chance of not registering a hit. Here it does not simulate the intrinsic efficiency of the chambers, but the effect of the badly measured layers present in the data but not in the Monte Carlo, which are lost in the bad hit drop.

Note that (3.2) only involves the azimuthal coordinate. This emphasis on $R\phi$ will be continued into the final cuts, and is an approach adopted from the PXMUID algorithm. When developing PXMUID for the 1990 data it was found that the z distributions had more extended tails than the azimuthal distributions, and, as a consequence, cuts on variables incorporating both coordinates yielded low efficiencies. These tails were mainly due to bad chambers (cured in MUCFIX), and the situation is improved in the 1991 data. Still, even then, tails in the distributions mean that almost twice as many hits are dropped with a $\chi^2_{\text{bad hit}}$ based on z, than on $R\phi$. Efficiency, accuracy considerations and agreement between data and Monte Carlo, therefore compel us to use $R\phi$ alone.

The tracks in the event having been refitted, the EMMASS χ^2_{global} and χ^2_{ex} are immediately available. The number of degrees of freedom for the former is

twice the number of associated layers. The equivalent quantity for the latter is not well defined; as a working variable we choose to use $N_{\rm ex}$, devised for PXMUID, where:

$$N_{\rm ex} \equiv \begin{cases} 1 \text{ if the number of associated layers} = 1 \\ 2 \text{ if the number of associated layers} = 2 \\ 4 \text{ if the number of associated layers} > 2 \end{cases} \tag{3.4}$$

In addition, for the barrel muon chambers, further chi-squared's are constructed. The extrapolated azimuthal chi-squared, $\chi^2_{\rm ex\ azth}$ is taken at the muon chamber layer closest to the interaction point and is defined as:

$$\chi^2_{\rm ex\ azth} \equiv \left(\frac{R\phi_{\rm fit} - R\phi_{\rm ex}}{\sigma^{R\phi}_{\rm ex}}\right)^2 + \left(\frac{\phi_{\rm fit} - \phi_{\rm ex}}{\sigma^{\phi}_{\rm ex}}\right)^2 \tag{3.5}$$

where the subscript 'ex' refers to the extrapolated track.

The total azimuthal chi-squared, $\chi^2_{\rm global\ azth}$, is defined as:

$$\chi^2_{\rm global\ azth} \equiv \chi^2_{\rm ex\ azth} + \sum \left(\frac{R\phi_{\rm fit} - R\phi_{\rm muc}}{\sigma^{R\phi}_{\rm muc}}\right)^2 \tag{3.6}$$

where the sum runs over the layers with associated hits. The number of associated layers is used as the number of degrees of freedom.

The other relevant tagging variable is the number of hits outside the iron, that is in layers $4-7$ for MUB and $3-4$ for MUF.

These variables are demanded to pass all of the following cuts to satisfy the Standard tag:

MUB Standard Cut	MUF Standard Cut
≥ 1 hit outside iron	≥ 1 hit outside iron
$\chi^2_{\rm global\ azth}\ p.d.f. \leq 7$	$\chi^2_{\rm global}\ p.d.f. \leq 5$
$\chi^2_{\rm ex}\ p.d.f. \leq 7$	$\chi^2_{\rm ex} \leq 5$

Thus there is a stringent requirement on track penetration, together with cuts on the χ^2's which are away from the centres of the distributions, thereby minimizing the effects of any bad Monte Carlo agreement. As can be seen in Fig.3.7 and Fig.3.8, the cut on the extrapolation χ^2 is very loose. This cut will mainly remove tracks that are wrongly associated to muon chamber hits.

The Loose tag cuts still further away from the distribution centre:

MUB Loose Cut	MUF Loose Cut
$\chi^2_{\text{global azth}}\, p.d.f. \leq 12$	$\chi^2_{\text{global}}\, p.d.f. \leq 7$
$\chi^2_{\text{ex}}\, p.d.f. \leq 12$	$\chi^2_{\text{ex}}\, p.d.f. \leq 7$

Note that there is no hit pattern requirement.

The Tight tag has the emphasis on purity, and results from stricter, albeit less well tuned cuts. Bad hits in MUF are dropped according to (3.3), but now both coordinates are used for MUB:

$$\chi^2_{\text{bad hit}} \equiv \left(\frac{R\phi_{\text{fit}} - R\phi_{\text{muc}}}{\sigma^{R\phi}_{\text{muc}}}\right)^2 + \left(\frac{z_{\text{fit}} - z_{\text{muc}}}{\sigma^{z}_{\text{muc}}}\right)^2 \tag{3.7}$$

For MUB data the cut is made at $\chi^2_{\text{bad hit}} > 8$, which requires a layer inefficiency in the Monte Carlo of 15.0% (1991), and for MUF data at $\chi^2_{\text{bad hit}} > 10$, which requires a layer inefficiency of 12% and 23.7% (1991). No further variable is used in addition to χ^2_{global}. To be identified by the Tight tag a track must satisfy:

MUB Tight Cut	MUF Tight Cut
≥ 1 hit outside iron	≥ 1 hit outside iron
$\chi^2_{\text{global}}\, p.d.f. \leq 2.5$	$\chi^2_{\text{global}}\, p.d.f. \leq 2.0$

The standard tag variables for muons in muon pair events (45 GeV/c), are shown in figure 3.7 for MUB tracks, in figure 3.8 for MUF tracks. The same variables, but now for muons in hadronic events, are shown in figure 3.9 for MUB

tracks, in figure 3.10 for MUF tracks, with $p > 3\,\mathrm{GeV/c}$ and $p_t > 0.6\,\mathrm{GeV/c}$. Satisfactory agreement between data and Monte Carlo is observed, apart from the MUF hadronic case, where the data is less penetrative, and the chi-squareds more spread, than in the Monte Carlo. The agreement improves with p_t and is good for muon pairs. For muons from a prompt b decay, which have a high pt, the agreement between data and MC is good. The disagreement at low p and p_t is attributed to bad modelling of punch-through in the simulation and perhaps due to a bad estimation of the amount of material in the forward region. It can also be seen by comparing the number of hits outside the iron, that the data is less penetrative than the Monte Carlo, but globally the number of tracks with at least one hit outside the iron agrees rather well between data and MC. The punch-through background is concentrated in the low momentum region. Hence, this kind of background can be probed by comparing the number of tagged muons in data and MC in the high and low momentum region. This will be done in the next analysis.

Performance

Using the available data samples, an estimate was made of the muon identification efficiency, ϵ_{muid}, and misidentification efficiency, $\epsilon_{\mathrm{misid}}$, of each MUFLAG tag. These are defined:

$\epsilon_{\mathrm{muid}} \equiv$ The probability that any muon track in the angular and momentum acceptance intervals will be tagged as a muon

$\epsilon_{\mathrm{misid}} \equiv$ The probability that any non-muon track in the angular and momentum acceptance intervals will be tagged as a muon

As angular acceptance intervals, the regions $0.026 \leq |\cos\theta| \leq 0.616$ (for MUB) and $0.743 \leq |\cos\theta| \leq 0.930$ (for MUF) were used; that is the regions around the '90° crack', the '40° hole', and the region below 20° were eliminated. The latter region is not well equipped with tracking detectors. All tracks were required to have momenta $\geq 3\,\mathrm{GeV/c}$. In evaluating ϵ_{muid}, the track had to represent a muon coming from a heavy quark decay; that is, only prompt muons are considered and those from pion decays etc. are excluded.

The momentum dependence of the average χ^2 per degree of freedom was examined, which should be flat as a function of the momentum for muons if all errors are correctly taken into account. This revealed a problem in the extrapolation of tracks to the forward muon chambers. These distributions for MUB and MUF are shown in Fig.3.6.

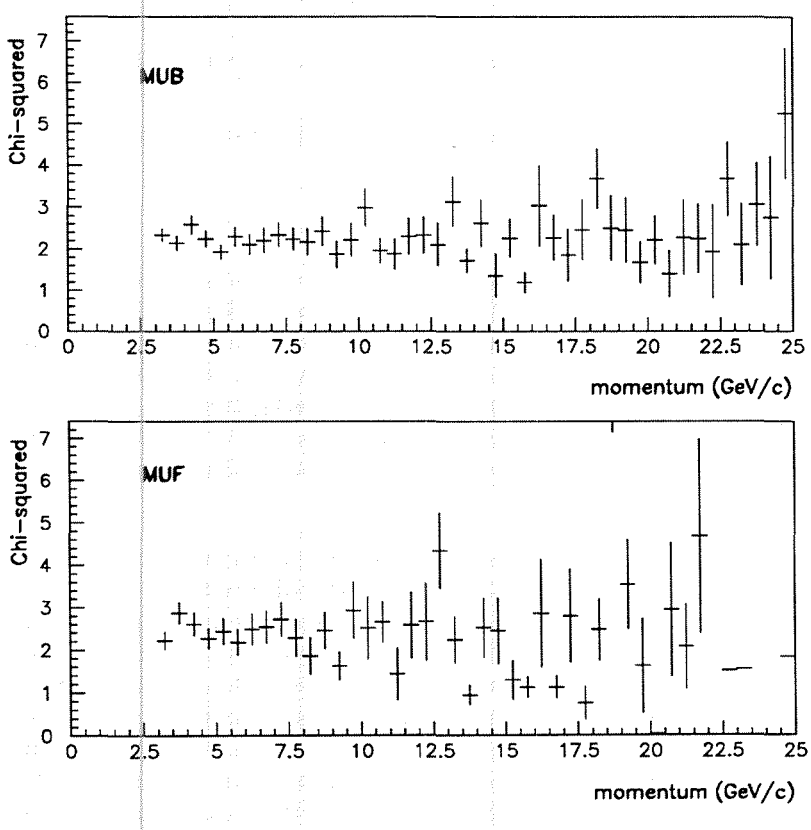

Figure 3.6: Mean χ^2 per degree of freedom versus momentum for MUB (upper) and MUF (lower).

Kind of cut	Kind of tag	total sample	muons
		Number of events	Number of events
No cut	Standard MUB	2566	1099
hit pattern cut		1740	975
χ^2 cuts		1238	903
No cut	Standard MUF	1406	480
hit pattern cut		876	450
χ^2 cuts		589	435

Table 3.3: Effect of standard cuts on a 1991 $q\bar{q}$ Monte Carlo Sample

In Monte Carlo hadronic events, the muon purity of a tagged sample increases from $\sim$ 42% in MUB ($\sim$ 32% in MUF) to $\sim$ 73% in MUB ($\sim$ 74% in MUF) when one applies the Standard Cuts. The elimination of background tracks for the standard tag, after each cut in a variable, is illustrated in Table 3.3. The hit pattern requirement reduces the background by 50% and 10% (6%) of the prompt muons are rejected by this cut in MUB (MUF). The χ^2 cut removes another 60% of the background and only 8% of the prompt muons.

In Table 3.4 the muon identification efficiency is shown for the different samples.The data $\mu^+\mu^-$, Monte Carlo $\mu^+\mu^-$ and Monte Carlo $q\bar{q}$ were used to measure ϵ_{muid}. The efficiency of identifying muons in muon pair events in data and MC agrees quite well. The efficiency of identifying a muon is $\sim$ 3 a 4% lower in hadronic events than in muon pair events. In hadronic events, the muons have lower momenta and consequently are less penetrative than in muon pair events. In both selection cuts, the hit pattern cut and the χ^2 cuts, more muons are rejected in hadronic events than in muon pair events. The lower efficiency of the χ^2 cut is attributed to the high multiplicity of hadronic events and hence the higher probability for misassociations.

In Table 3.5 the misidentification rate is shown for the different samples. The τ 1 vs. 3, K^0_S and Monte Carlo $q\bar{q}$ samples were used to measure ϵ_{misid}. Within statistical error, the misidentification rate does agree between data and MC. However, these three sample are not expected to have all the same misidentification rate. The particles in the used data samples (τ 1 vs. 3, K^0_S) are pions, in contrast to the $q\bar{q}$ events, where also kaons contribute to the sail-through. The three samples have also different momentum distributions, which will induce different punch-through probabilities.

Sample		Standard Tag	Tight Tag	Loose Tag
		ϵ_{muid}	ϵ_{muid}	ϵ_{muid}
$\mu^+\mu^-$ data	MUB 1991	86.5 ± 0.6	67.8 ± 0.8	95.7 ± 0.3
	MUF 1991	87.8 ± 0.9	76.7 ± 1.2	95.6 ± 0.6
$\mu^+\mu^-$ MC	MUB 1991	84.8 ± 0.3	72.1 ± 0.5	95.4 ± 0.2
	MUF 1991	86.0 ± 0.5	75.6 ± 0.8	93.0 ± 0.3
$q\bar{q}$ MC	MUB 1991	81.2 ± 1.1	66.2 ± 1.6	92.3 ± 0.8
	MUF 1991	81.7 ± 1.6	63.3 ± 2.4	88.4 ± 1.5
$\mu^+\mu^-$ data	MUB 1990	83.2 ± 0.8	60.0 ± 1.0	92.9 ± 0.6
	MUF 1990	90.0 ± 1.4	76.0 ± 2.0	93.9 ± 1.2
$\mu^+\mu^-$ MC	MUB 1990	85.1 ± 0.5	81.0 ± 0.6	94.0 ± 0.4
	MUF 1990	92.8 ± 0.6	77.0 ± 0.9	95.2 ± 0.5
$q\bar{q}$ MC	MUB 1990	79.0 ± 1.3	65.4 ± 1.5	88.0 ± 1.2
	MUF 1990	86.9 ± 1.5	65.3 ± 2.1	88.0 ± 1.7

Table 3.4: Muon identification efficiencies for the MUFLAG tags in the 1991 and 1990 data and Monte Carlo. Values are given as percentage probabilities, errors are statistical.

Sample		Standard Tag	Tight Tag	Loose Tag
		ϵ_{misid}	ϵ_{misid}	ϵ_{misid}
$q\bar{q}$ MC	MUB 1991	0.79 ± 0.04	0.47 ± 0.03	1.54 ± 0.05
	MUF 1991	0.94 ± 0.06	0.53 ± 0.05	1.65 ± 0.08
τ 1 vs. 3	MUB 1991	0.8 ± 0.3	0.5 ± 0.2	1.9 ± 0.3
	MUF 1991	1.2 ± 0.5	0.8 ± 0.4	2.0 ± 0.6
$K^0_S \to \pi^+\pi^-$	MUB 1991	0.5 ± 0.1	0.4 ± 0.1	1.2 ± 0.2
	MUF 1991	0.8 ± 0.3	0.5 ± 0.2	1.9 ± 0.5
$q\bar{q}$ MC	MUB 1990	0.97 ± 0.04	0.81 ± 0.04	1.75 ± 0.06
	MUF 1990	1.44 ± 0.07	0.92 ± 0.06	3.05 ± 0.12
τ 1 vs. 3	MUB 1990	1.6 ± 0.5	1.4 ± 0.6	2.2 ± 0.6

Table 3.5: Muon misidentification efficiencies for the MUFLAG tags in the 1991 and 1990 data and Monte Carlo. Values are given as percentage probabilities, errors are statistical.

3.5 Conclusion

In this chapter the procedure by which muons are identified in DELPHI is explained. A detailed study was made of the muon association and the performance of the muon chambers. Systematic errors and bugs were traced down and are corrected on DST level. This could be done very accurately by redoing the EMMASS refit on the DST by MUCFIX. A large effort was spent on estimating the correct muon chamber errors and getting a reasonable agreement between data and Monte Carlo on the muon identification variables, like χ^2's and muon chamber efficiencies. An algorithm was developed for identifying muons in hadronic events, where we seek an optimum between efficiency and purity. This algorithm has been implemented in the "general" muon identification routine MUFLAG. The performance of this muon identification algorithm is studied on different samples of Monte Carlo and data. The Monte Carlo simulation reproduces, within statistical error, the same figures as measured directly from dedicated data samples. For a muon identification efficiency of $\sim 81\%$, a misidentification probability of $\sim 0.8\%$ is obtained with the standard tag. This corresponds to a muon purity of the selected sample of 73%.

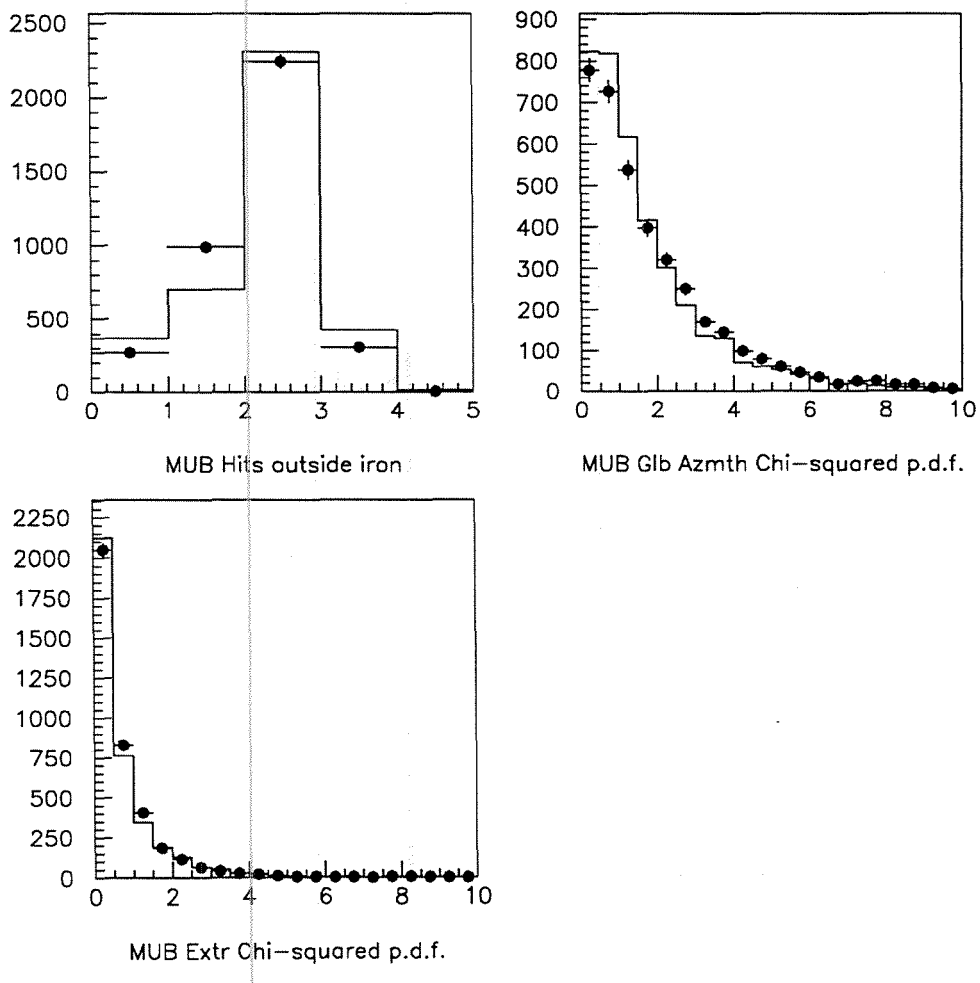

Figure 3.7: Standard and Loose MUB tagging variables in 1991 muon pairs: hits outside iron (Monte Carlo as histogram) (a), $\chi^2_{\text{global azth}}\, p.d.f.$ (b). $\chi^2_{\text{ex}}\, p.d.f.$ (c)

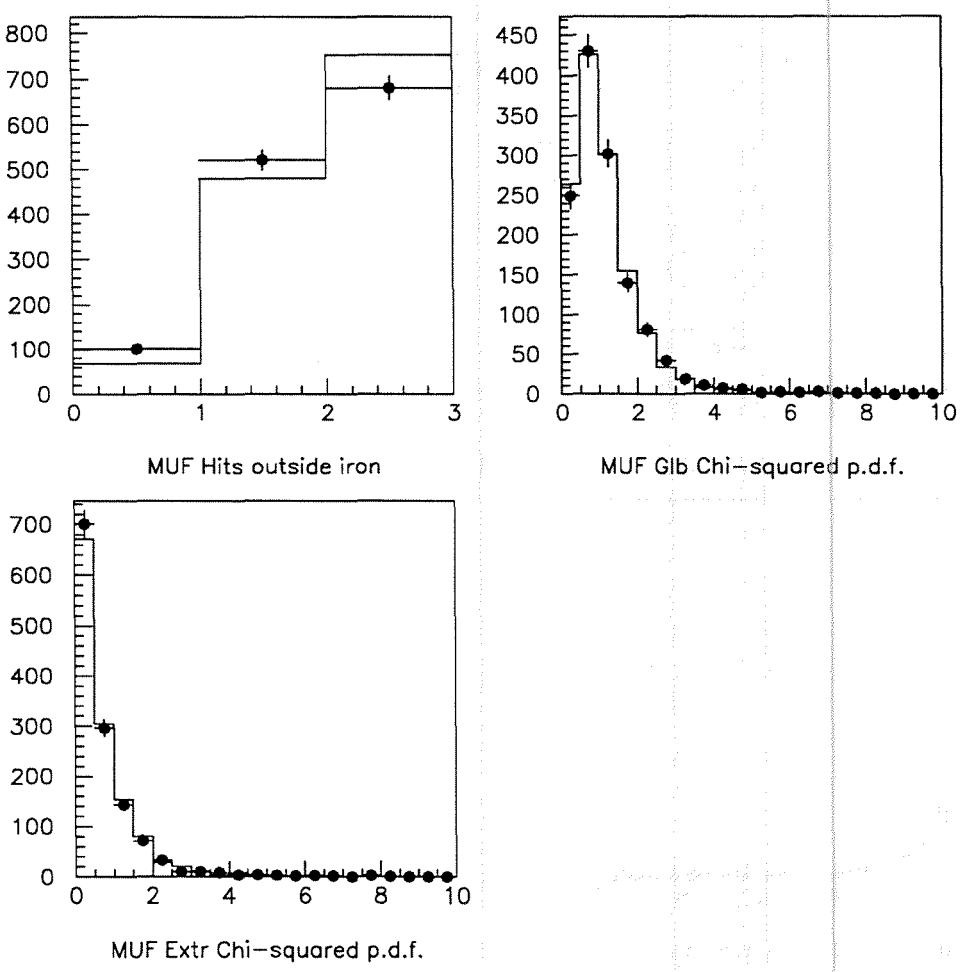

Figure 3.8: Standard and Loose MUF tagging variables in 1991 muon pairs: hits outside iron (Monte Carlo as histogram) (a), $\chi^2_{\rm global}$ *p.d.f.* (b), $\chi^2_{\rm ex}$ *p.d.f.* (c).

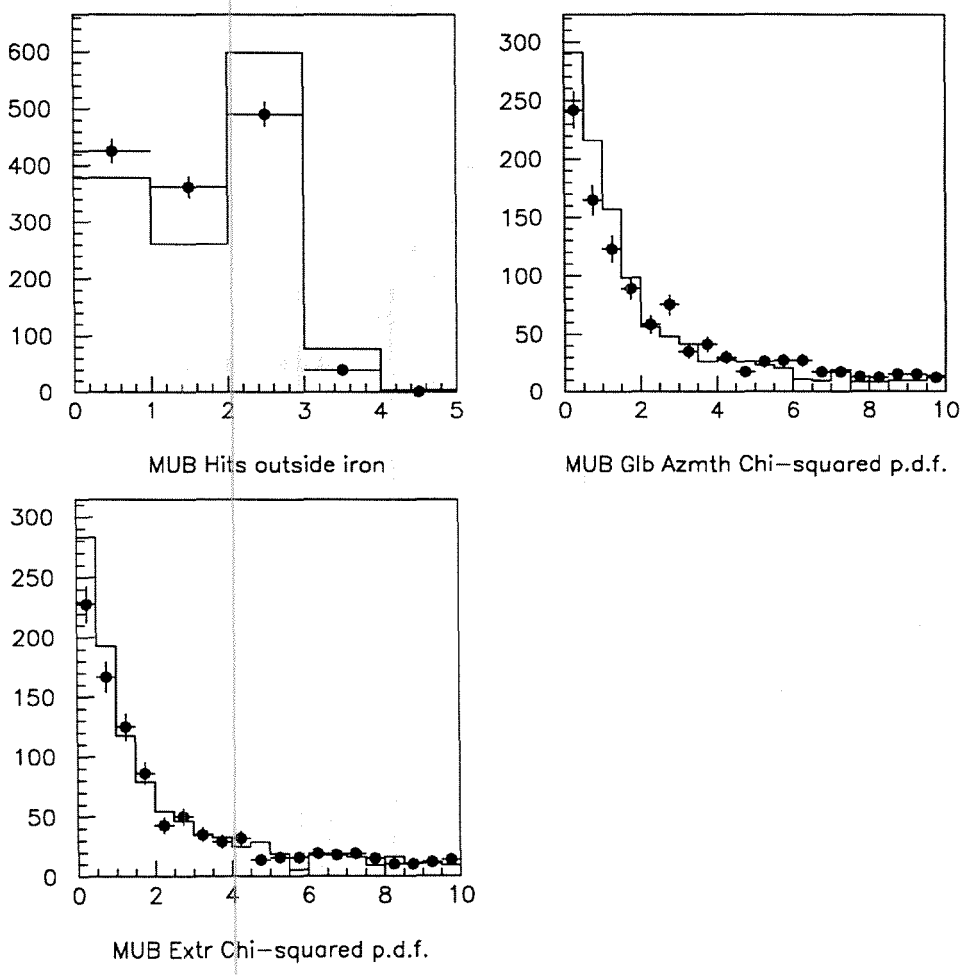

Figure 3.9: Standard and Loose MUB tagging variables in 1991 hadronic events: hits outside iron (Monte Carlo as histogram) (a), $\chi^2_{\text{global azth}}$ $p.d.f.$ (b). χ^2_{ex} $p.d.f.$ (c)

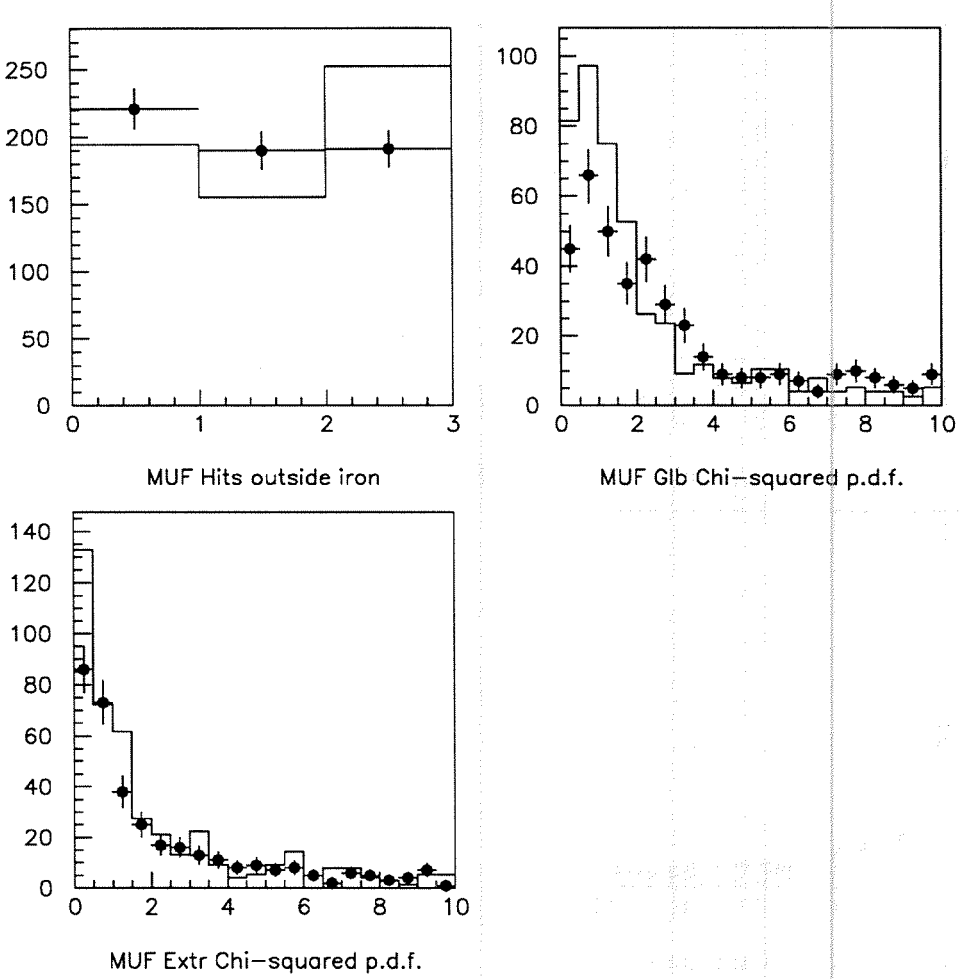

Figure 3.10: Standard and Loose MUF tagging variables in 1991 hadronic events hits outside iron (Monte Carlo as histogram) (a), χ^2_{global} *p.d.f.* (b), χ^2_{ex} *p.d.f.* (c).

Chapter 4

Heavy quark tagging

The event sample used in the following analyses, is the decay of the Z^0 in a quark-antiquark pair. In this chapter, the selection of this sample is described. Some algorithms for the reconstruction of the quark direction are discussed. Different tagging methods that can be used for enriching the hadronic sample in bottom quark events are explained.

4.1 Hadronic event selection

The hadronic events are selected by criteria based on the number of charged particles. The tracks were required to fulfill the following criteria:

- The track has a momentum between 0.1 and 50 GeV/c.
- The track lies inside the angular region $20^o < \theta < 160^o$.
- The relative momentum error $\frac{\Delta p}{p}$ of the track is less than 1.
- The track extrapolates back to the nominal crossing point within 5 cm in $R\phi$ and 10 cm in z.
- The track length is greater than or equal to 30 cm.

An event is classified as a hadronic event if the event fulfills the following criteria:

- There are at least 7 tracks fulfilling the above mentioned track criteria.
- The number of tracks with momentum above 0.2 GeV/c, is at least 5.
- The sum of the energy of the charged particles is larger than or equal to 3 GeV in each of the two hemispheres $\cos\theta < 0$ and $\cos\theta > 0$.
- The total charged particle energy in the event is greater than or equal to 15 GeV.

The efficiency of this event selection is $91.7 \pm 0.2\%$. The selected event sample has a negligible ($< 0.3\%$) contamination of $\tau^+\tau^-$ pairs, $\gamma\gamma$ interactions and beam-gas scattering.

4.1.1 Reconstruction of the quark direction

The direction of flight of the original quarks, which corresponds to the direction of flight of a jet of particles, can be approximated by different variables: the thrust axis, sphericity axis or jet axis. The characteristic feature of a jet is that all particles in the jet have limited transverse momenta with respect to the jet axis and hence also with respect to each other.

- The *Thrust axis* is defined as the unit vector $\vec{T}$ which maximises the thrust, T, defined as

$$T = max\left(\frac{\sum_i \vec{p}_i.\vec{T}}{\sum_i |\vec{p}_i|}\right),$$

where the sum of the momenta $\vec{p}_i$ is taken over all charged tracks. The value of the thrust varies from 0.5 for an isotropic event to 1 for an event with narrow back-to-back jets. Since the b quark is characterised by a hard fragmentation, the B hadron direction approximates very well the b quark direction as shown by the LUND Monte Carlo in Fig.4.1.a. In heavy quark events, the thrust axis is a reasonable approximation of the direction of flight of the heavy hadrons in the majority of the events. The angular difference between the B hadron direction and the thrust axis is shown in Fig.4.1.b. The tail in this distribution is due to events where the B hadron has little energy due to radiation of a hard gluon in the final $b\bar{b}$ system. If the quarks radiate a hard gluon, events with more than two jets are produced and the B hadrons will not be back-to-back. Hence the thrust axis can not reconstruct accurately the direction of both hadrons. The thrust axis can be used to divide the event in two hemispheres defined by

the plane perpendicular to the thrust axis through the interaction point. Each hemisphere will then contain particles coming from the quark or from the antiquark.

- The *sphericity* is another global event variable, which characterises the event shape. It is defined as

$$S = \frac{3}{2} min \left(\frac{\sum_i |\vec{p}_i \times \vec{S}|^2}{\sum_i |\vec{p}_i|^2} \right),$$

where the sum i is taken over all tracks and the unit vector $\vec{S}$ is the vector which minimises the momentum sum. $\vec{S}$ is called the sphericity axis. The sphericity axis is similar to the thrust axis, but is more strongly affected by high momentum tracks, since it depends on the square of the momenta. The value of the sphericity S will range from 0 for narrow 2-jet events to 1 for an event where the tracks are isotropically distributed.

- *The Minimal Invariant Mass algorithm (MIM)* is a cluster algorithm developed by the JADE collaboration[44], which starts by combining all particles i and j into pairs by adding their 4-momentum vectors p_i, p_j. Their invariant mass is calculated under the assumption that the masses of particles i and j are negligible with respect to their energy:

$$m_{ij}^2 = 2E_iE_j(1 - \cos\theta_{ij}).$$

Here are E_i, E_j the energies of the two particles i and j, θ_{ij} is the angle between their momentum vector. This m_{ij} is then scaled to $y_{ij} = m_{ij}^2/W^2$, with W^2 the total invariant mass squared of all particles being considered. The pair with the smallest invariant mass is replaced by one pseudoparticle with four momentum $(p_i + p_j)$ and the procedure is repeated until all y_{ij} values are greater than a certain cut-off value y_{cut}. The remaining pseudoparticles or particles are called the jets of the event. The y_{cut}-value that will be used is 0.01.

- *The LUCLUS [17] clustering algorithm*: The distance measure d_{ij} between two particles with momenta $\vec{p}_i$ and $\vec{p}_j$ is chosen as

$$d_{ij}^2 = \frac{4p_i^2p_j^2\sin^2\frac{\theta_{ij}}{2}}{(p_i + p_j)^2}$$

For small relative angles θ_{ij} this becomes

$$d_{ij} \simeq \frac{|\vec{p}_i \times \vec{p}_j|}{|\vec{p}_i + \vec{p}_j|}$$

and can be interpreted as the transverse momentum of either particle with respect to the direction given by the sum of the particle momenta. The scheme of combination is the same as described in the MIM algorithm. The two clusters with smallest relative distance d are joined if $d < d_{join}$, with d_{join} some predetermined distance. The default value is used, namely $d_{join} = 2.5$ GeV.

The angular difference between the B direction and the jet axis direction for the MIM algorithm is shown in Fig.4.2. When using the LUCLUS algorithm this distribution looks very similar. The MIM algorithm will be used because the agreement between data and Monte Carlo in terms of number of jets is somewhat better with this algorithm than with the LUCLUS algorithm. A slightly better b purity of our sample is obtained when using the MIM algorithm.

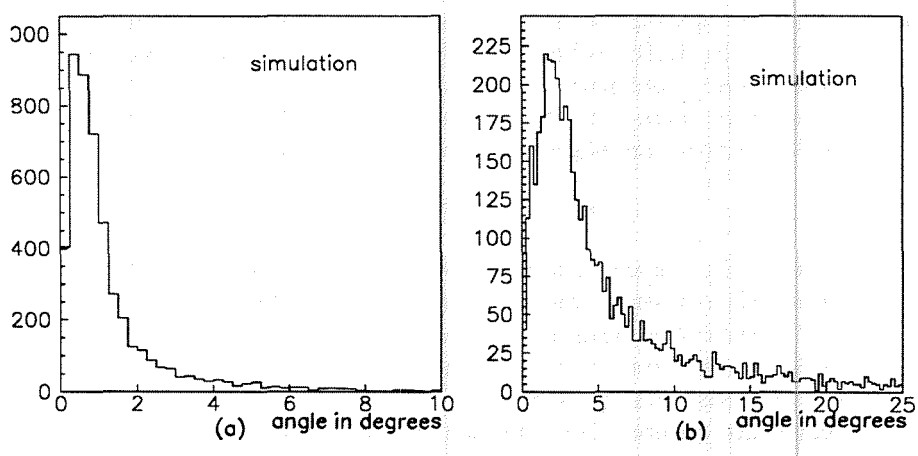

Figure 4.1: a) Angular difference between B direction and b direction.
b) Angular difference between B direction and thrust-axis.

4.1.2 Event selection

In addition to the hadronic event selection, a few cuts are made on event variables:

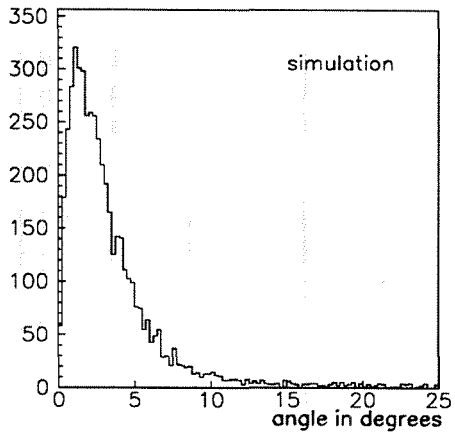

Figure 4.2: Angular difference between B direction and jet direction.

- Only events that are well contained in the detector are accepted: the direction of the thrust axis $|\cos\theta_{thrust}|$ should be less than 0.85 for 1990 data and less than 0.90 for 1991 and 1992 data.
- The event is required to have at least two reconstructed jets.
- When using a muon from a semileptonic decay, the jet the muon belongs to should have an energy greater than 4 GeV.

4.2 Heavy quark enriched sample

Since quarks cannot be isolated, their properties must be inferred from the hadronic jets initiated by the quarks.

- Due to the large mass of the b-quark and therefore a small probability to extract $b\bar{b}$ pairs from the vacuum, the presence of a B hadron indicates the presence of a b-parent quark. The B hadrons have a high mass and therefore their decay products will have large momenta in the restframe of the B hadron. This large momenta are boosted in the centre of mass

system of the event and will lead to high transverse momenta with respect to the flight direction of the B hadron.

- The fragmentation of heavy quarks, compared to light quarks, is expected to be much harder[1] (see chapter 1) and hence the heavy quark hadron will have a large fraction of the energy of the event.

- The mean lifetime of B hadrons is about 1.5 ps[76] and together with its rather hard fragmentation, the mean decay length of a B hadron at the Z^0 mass is about 2.8 mm.

4.2.1 Lepton tag

The first two characteristics are used for tagging b quarks that decay semileptonically [45, 46, 47, 54, 56]. Tracks from B decays will tend to have a large total momentum (p) and a large momentum component transverse to the jet axis (p_t). Leptons from the semileptonic decay of the B hadron are therefore selected by demanding a high p and p_t.

The following semileptonic decay chains for heavy quarks are considered:

$b \rightarrow l^- \bar{\nu}_l c$

prompt lepton from b decay

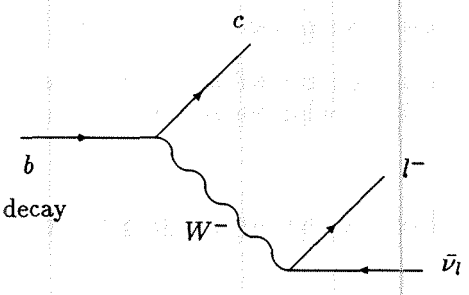

[1] A hard fragmentation means that the hadrons will get a high fraction of the momentum of the initial quark.

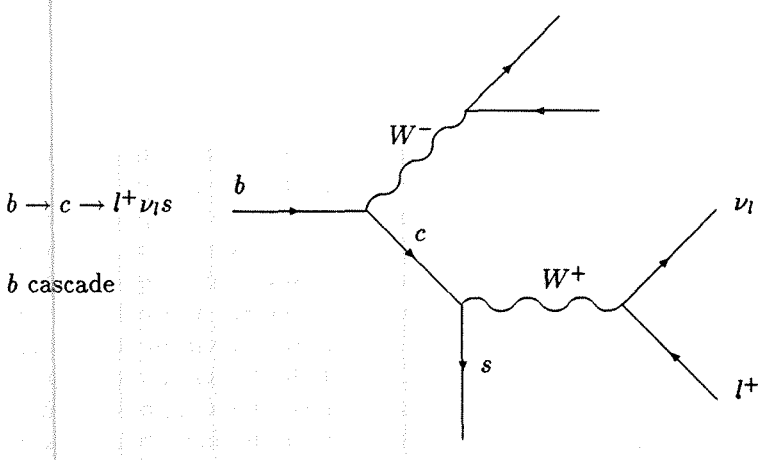
$b \to c \to l^+\nu_l s$
b cascade
b
W^-
c
W^+
s
ν_l
l^+

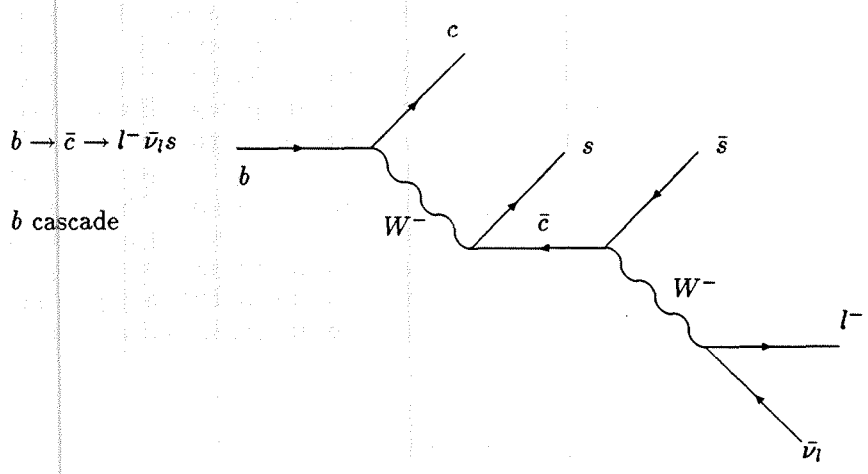
$b \to \bar{c} \to l^-\bar{\nu}_l s$
b cascade
b
c
W^-
s
$\bar{c}$
$\bar{s}$
W^-
l^-
$\bar{\nu}_l$

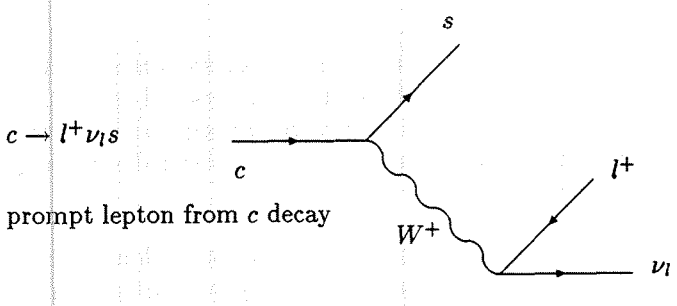
$c \to l^+\nu_l s$
prompt lepton from c decay
c
s
W^+
l^+
ν_l

p_t definition

In a hadronic sample, the fraction of b events that contains a lepton, can be enriched by cuts on the p_t value of the lepton with respect to the jet axis. The transverse momentum of the lepton with respect to the jet axis, which has been reconstructed by combining *all* tracks, hence also the lepton, will be named pt_{in}. If the lepton momentum vector has been subtracted from the total momentum vector of the jet axis it belongs to, the transverse momentum with respect to this new jet axis is called pt_{out}. It appears that a cut on pt_{out} is more efficient than a cut on pt_{in} to separate the b events that contain a prompt lepton from the other b and *udsc* events. This can be understood as follows: in the quantity pt_{in} the momentum of the lepton, which is harder in the case of a semileptonic b decay, will pull the jet axis towards the direction of the lepton and hence decrease its pt. Hence, for a given efficiency, we have a better $b \rightarrow \mu$ purity for a cut in pt_{out} than for a cut in pt_{in}. The b purity of the sample versus the efficiency of tagging a prompt muon from a b quark is shown in Fig.4.3.a. However, if we consider the b purity versus the efficiency of tagging a b quark, this difference disappears: pt_{in} gives a better purity/efficiency than pt_{out} for the b cascade. The purity versus efficiency for tagging a b event is shown in Fig.4.3.b. The $b \rightarrow \mu$ purity is thus the fraction of events containing a *prompt* b muon, whereas the b purity is the fraction of all kind of b events (also muons from e.g. the cascade b contribution or even muons from pion and kaon decay in a b quark event). The b sample purity as a function of a cut in pt_{in} and pt_{out} is shown in Fig.4.4. We will continue to use the definition of pt_{in} and use pt_{out} for estimating the contribution of the pt definition to the systematic error.

4.2.2 Boosted sphericity tag

The boosted sphericity product is another quantity which characterises the shape of the events and can be used to select a b enriched sample. Due to their larger mass, b events will be characterised by particles with a larger spread in transverse momenta than *udsc* events. The above defined sphericity S is used to quantify this property.

After selecting two jet events, the jets are boosted along their jet axes towards their hypothetical B hadron restframe by a boost β. The boost β is tuned via MC simulations in order to optimise the separation between the b events and the non-b events ($\beta = 0.96$). The sphericities S_1, S_2 of the two jets are then calculated in their reference restframe. The boosted sphericity product is defined as the product of S_1 and S_2. The observed $S_1.S_2$ distribution is fitted to the $S_1.S_2$ distribution of the b's and the one of the non-b's [49, 50].

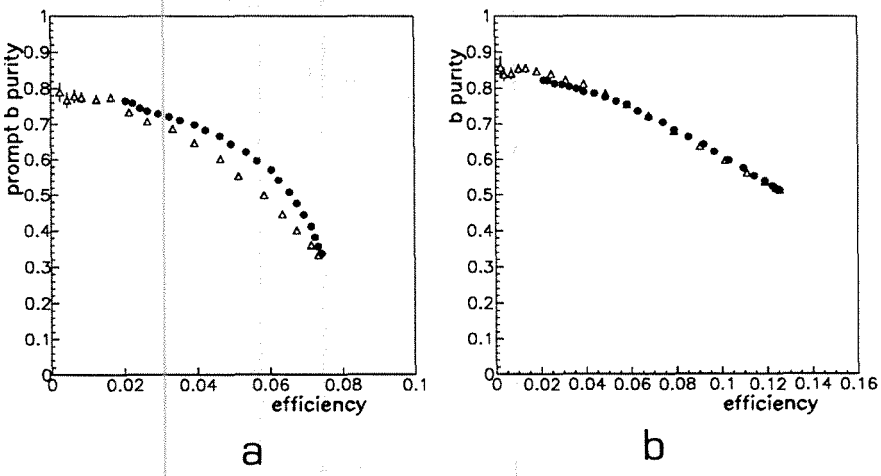

Figure 4.3: a)($b \rightarrow \mu$) purity of the tagged sample versus efficiency for pt_{in}(triangles) and pt_{out}(dots).
b) b purity of the tagged sample versus efficiency for pt_{in}(triangles) and pt_{out}(dots).

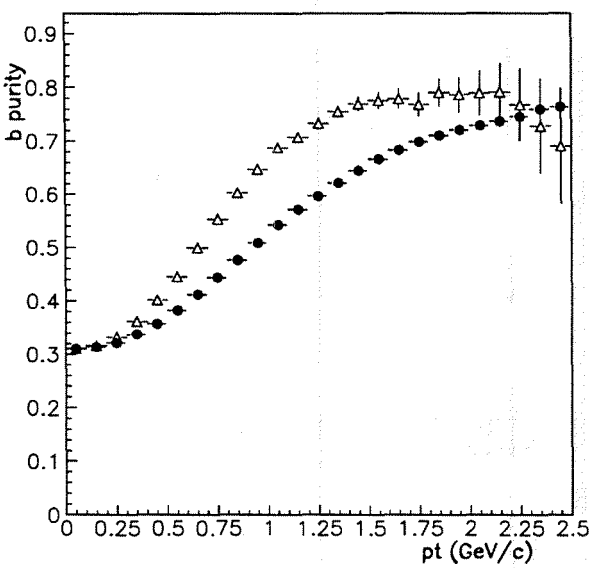

Figure 4.4: b purity of the tagged sample as a function of a cut in pt_{in}(triangles) and pt_{out}(dots).

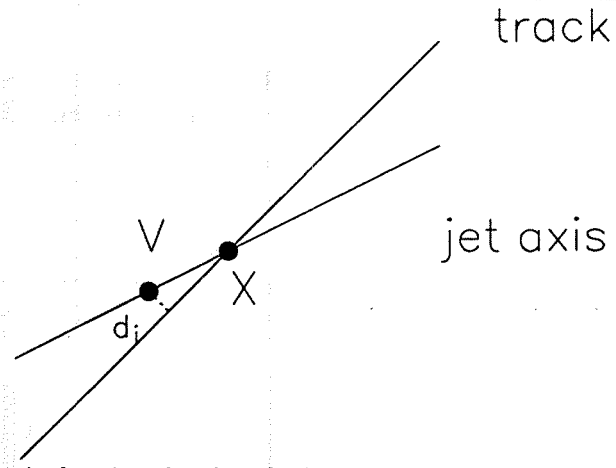

Figure 4.5: Schematic drawing showing the impact parameter definition.

4.2.3 Impact parameter tag

Due to the relatively long lifetime of the B hadron, its decay products will not point back to the primary vertex. The impact parameter, d_i, of a charged particle is defined as the distance of closest approach of the extrapolated track to the assumed production point V in the $r\phi$ plane;

$$d_i = L_i \sin\theta_B \sin(\phi_i - \phi_B),$$

where L_i is the decay length (the distance from V to X on Fig.4.5), ϕ_B and θ_B are the azimuthal direction and polar angle of the decaying B hadron, ϕ_i is the azimuthal angle of the track.

Experimentally, the sign of the impact parameter is defined as the sign of the vector cross product of the projection on the $r\phi$ plane of the track vector at the point of closest approach and the vector from the centre of the interaction region to the point of closest approach.

In the next analysis, the lifetime signed impact parameter is used, which differs from the geometric impact parameter only in its sign. The sign is positive if the extrapolated track intersects the B direction before reaching the point of closest approach, negative otherwise. If the geometry of the production and decay could be reconstructed perfectly, the lifetime signed impact parameter would always be positive. The B direction is estimated by the jet axis to which the particle belongs. The centre of the interaction region is given by the beamspot. It was determined run by run by using $\mu^+\mu^-$ events. It was found that the x and y projections of the interaction region were well represented by Gaussian distributions with $\sigma_x = 140\ \mu m$ and $\sigma_y = 15\ \mu m$. The lifetime signed impact parameter for uds, c and b events are shown in Fig.4.6. The full histogram

represents all events. On the left plot, the *uds* and *c* events are shown, on the right plot the *b* events are shown by the filled histogram. The *b* events dominate the high impact parameter region.

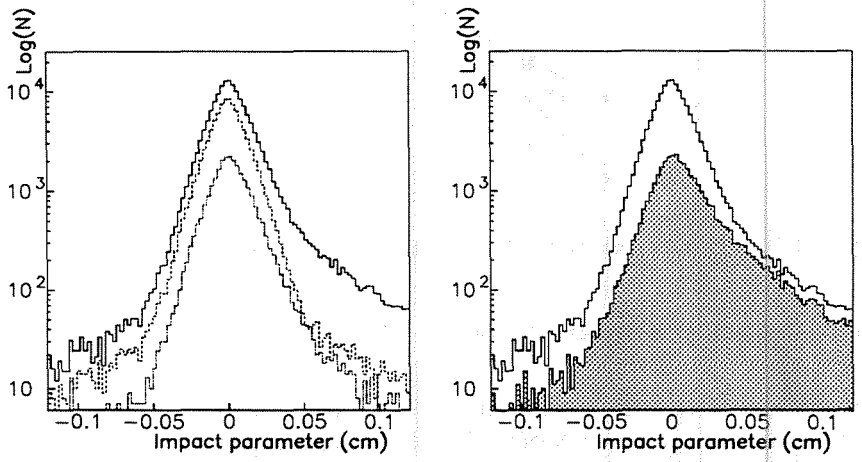

Figure 4.6: Lifetime signed impact parameter for all (full), uds (dashed) and c (points) events (left); *b* events are shown in the right plot by the filled histogram.

4.2.4 B lifetime tag

Another tag based on the lifetime of the B hadron, is to reconstruct the secondary vertex (B decay point) and to measure the distance between this vertex and the primary vertex. This requires a careful approach in fitting primary and secondary vertices. We will not go into detail on this tag method, because we will not use it in this work.

4.2.5 Combined tags

The efficiency for *b* tagging can be improved by using two or more of the tags described above. Different tag variables are input to an algorithm to separate the *b*, *c* and *uds* flavours. A classification of the different classes can be achieved by using a neural network [52] or by a multi-dimensional analysis [53].

Two independent tags can be used in each of the two hemispheres of the event. This has the nice feature that the efficiency of one tag can be determined, by using the tag in the other hemisphere. An analysis based on the lepton and the impact parameter tag is described in chapter 5.

Chapter 5

Measurement of $\Gamma_{b\bar{b}}$ and the b forward-backward asymmetry

5.1 Measurement of $\Gamma_{b\bar{b}}$ and the b forward-backward asymmetry using the semileptonic decay into muons

The branching ratio $\Gamma_{b\bar{b}}$ and the forward-backward asymmetry for bottom quarks A_{FB}^{b} are determined by selecting their semileptonic decay into muons. This analysis has been performed for the latest 1990 hadronic processing and the DELANA_E processing of the 1991 data. After the selection of events with a well functioning TPC, forward chambers and muon chambers, one is left with a sample of $\sim$ 87000 (1990) + 205000 (1991) hadronic events. The MC sample for 1990 consists of 47802 hadronic ($q\bar{q}$) Parton Shower events and dedicated event samples for $b \rightarrow \mu X$, $b \rightarrow c \rightarrow \mu X$ and $c \rightarrow \mu X$, corresponding to an equivalent of $\sim$ 167000, 57000 and 216000 hadronic events respectively. The MC sample for 1991 consists of $\sim$ 350000 hadronic Parton Shower events. No dedicated MC samples were used for the 1991 analysis.

After the results of a first analysis were published [56, 54], a reanalysis has been done using the latest corrections to the muon identification chain as described in chapter 3.

First hadronic events, that contain at least one muon, are selected. The muons produced by b decay have large transverse momentum with respect to the jet axis. This allows to separate the b quark events from other background channels. The flavour origin of the muons as well as the hadronic background are taken from the Monte Carlo. The Monte Carlo sample is divided into five classes:

- f_b, muons from prompt b decay ($b \rightarrow \mu$ and $b \rightarrow \tau \rightarrow \mu$)
- f_{bc}, muons from b cascade ($b \rightarrow c(\bar{c}) \rightarrow \mu$)
- f_c, muons from prompt c decay ($c \rightarrow \mu$)
- f_μ, muons from hadronic decays (π's,K's)
- f_{back}, misidentification background.

The charge of the muon in the semileptonic b decay, reflects the charge of the original quark. In particular, b quarks yield prompt μ^-. The variables used are the momentum p and the transverse momentum p_t with respect to the jet axis, which is determined using the MIM algorithm (see section 4.1.1) for charged particles only.

5.1.1 Sample composition

Muons are selected according to the criteria described in chapter 3. To exclude regions with poor geometrical acceptance the muon is accepted if the polar angle θ_μ is within the following intervals.

For 1990 data,

$$0.03 < |\cos\theta_\mu| < 0.60 \text{ (barrel)}$$

$$0.71 < |\cos\theta_\mu| < 0.86 \text{ (forward)}$$

For 1991 data, the polar acceptance could be extended, because the tracking reconstruction efficiency was improved in the forward region:

$$0.03 < |\cos\theta_\mu| < 0.60 \text{ (barrel)}$$

$$0.71 < |\cos\theta_\mu| < 0.93 \text{ (forward)}$$

The momentum distribution of all identified muons for data (points) and MC (histogram) is shown in Fig.5.1 for 1990 and 1991 data. A momentum greater than 3 GeV/c is required. The MC and data are normalised to the number of hadronic events. In 1990, there was a discrepancy between data and MC,

especially at low momenta the number of tagged muons in MC was much higher than in the data. It was attributed to a bad description of the hadronic background (punch-through) in the tagged muon sample in the MC. A weight was assigned to the misidentified muons in the MC to correct for it. The bad description of the punch-through was confirmed by an independent analysis using the hadron calorimeter. It was shown that the simulation of the development of the hadronic shower did not agree with the data. This discrepancy was corrected for in the 1991 MC.

The $\cos\theta$ dependence of tagged muons in hadronic events in data and simulation is shown in Fig.5.2. The tagging efficiency is lower in endcap A than in endcap C. For muon pairs the detection efficiency is the same in both endcaps. Possibly this can be due to a higher amount of sail-through particles in C, because there was not yet a forward RICH installed (hence, less material) in endcap C. The Monte Carlo describes it rather well.

The muon identification efficiency and contamination can be estimated from the simulation. Moreover, cross-checks were made on special data samples.

- Muon pair events have been used to measure the efficiency. The relevant values can be found in the chapter on muon identification (see Table 3.4 and Table 3.5). The difference in central value of the efficiency in the muon pair data and the muon pair Monte Carlo is taken as an estimate of the efficiency uncertainty. This uncertainty is estimated to be 3%. The efficiency in hadronic events is $\sim$ 4% lower than the muon identification efficiency in muon pair events. This is attributed to the lower momenta of the muons and the ambiguities in hadronic events.

- The purity of the tagged sample can be studied with the three prong topology of the τ decay, and the decay of a K^0_S into 2 pions. Unfortunately, for 1990 and 1991, those data samples have low statistics and consequently give still large errors. The amount of background in hadronic events as compared with the simulation, can also be probed by counting the number of muons, normalised to the number of hadronic events, in the low p_t ($p_t < 0.5$ GeV/c) region.

The composition of the tagged sample for momenta between 3 and 35 GeV/c, is given in Table 5.1 for the different classes. The composition depends on the jet algorithm used: if neutral particles are included in the jet reconstruction algorithm, the efficiency for tagging prompt muons is $\sim$ 5% higher.

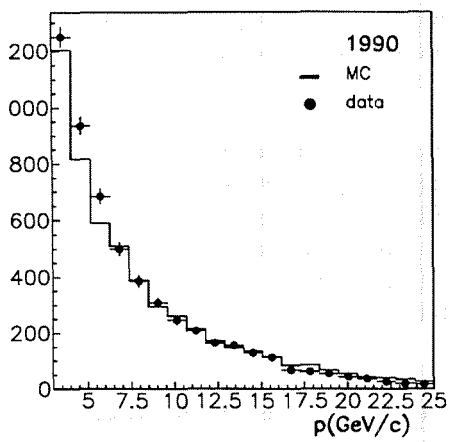

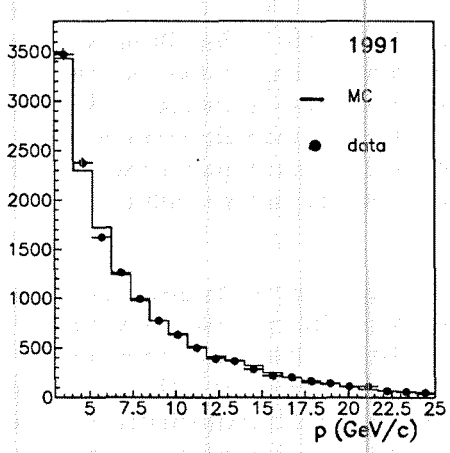

Figure 5.1: Momentum distribution of particles tagged as muon in 1990 (left) and 1991 (right) hadronic events.

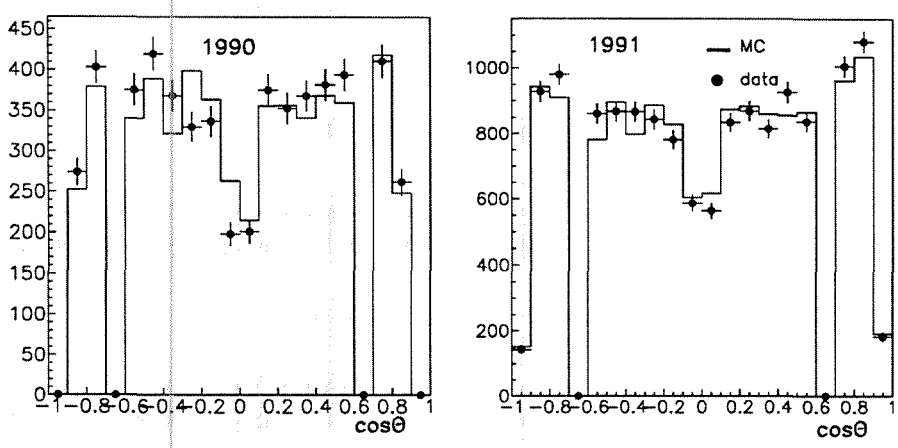

Figure 5.2: $\cos\theta$ distribution of particles tagged as muon in 1990 (left) and 1991 (right) hadronic events.

Source	no pt_{in}-cut	$pt_{in} < 0.5$ GeV/c	$pt_{in} > 0.6$ GeV/c	$pt_{in} > 1$ GeV/c
f_b	0.252	0.084	0.531	0.714
f_{bc}	0.146	0.143	0.116	0.075
f_c	0.152	0.181	0.112	0.061
f_μ	0.105	0.142	0.051	0.032
f_{back}	0.345	0.450	0.190	0.118

Table 5.1: Muon sample composition according to the 1991 MC.

5.1.2 Fitting procedures

A binned maximum likelihood fit in the two-dimensional $p - p_t$ distribution is used to obtain the branching ratio and the asymmetry of the b quark.

Branching ratio

The following quantities are free parameters in the fit:

- R_b : The ratio of the partial width of the b quarks to the total hadronic width, multiplied by the semileptonic decay branching fraction of the b quarks into muons:
$$R_b = \frac{\Gamma_{b\bar{b}}}{\Gamma_{had}} \times BR(b \to \mu)$$
- R_c : The ratio of the partial width of the c quarks to the total hadronic width, multiplied by the semileptonic decay branching fraction of the c quarks into muons:
$$R_c = \frac{\Gamma_{c\bar{c}}}{\Gamma_{had}} \times BR(c \to \mu)$$
- $R_{h\to\mu}$: The fraction of $q\bar{q}$ events that will give rise to a non-prompt muon in the final state.
- $R_{h\to\text{misid}}$: The fraction of $q\bar{q}$ events that will yield a misidentification in the final state.

All these parameters are normalised to the values of the simulation (or equivalently to the standard model). The likelihood function is defined as:

$$L = \sum_{i,j=1}^{i=n,j=m} -2N_d(i,j)\log F(i,j),$$

with i the bin index of the p and j the bin index of the p_t distribution. The probability distribution F is constructed as:

$$F(i,j) = R_{norm}[R_b\,(N_{b\to\mu}(i,j) + N_{b\to c\to\mu}(i,j)) + R_c\,N_{c\to\mu}(i,j)$$
$$+R_{h\to\mu}\,N_{h\to\mu}(i,j) + R_{h\to\text{misid}}\,N_{h\to\text{misid}}(i,j)]$$

R_{norm} is the ratio of the number of hadronic events in the data to the number of hadronic events in the Monte Carlo. The number of data events in bin i,j is described by a sum of number of events of the different classes of that

bin: $N_{b\to\mu}(i,j), N_{b\to c\to\mu}(i,j), N_{c\to\mu}(i,j), N_{h\to\mu}(i,j)$ and $N_{h\to\text{misid}}(i,j)$. Furthermore, the probability distribution should be normalised to 1. The following equality holds:

$$\sum_{i,j} N_{data}(i,j) = \sum_{i,j} F(i,j)$$

This latter equation is used to eliminate one of the free parameters.

Asymmetry

The method is based on counting the number of events in the forward ($\theta < 90^o$) and backward ($\theta > 90^o$) hemispheres with respect to the initial electron direction. The direction of the b quark is taken to be the thrust axis (oriented by the jet containing the muon) of the charged particles in the hadronic event. The orientation of the b quark is then calculated by multiplying $-\cos\theta_{thrust}$ with the muon charge. A forward event is thus defined as a μ^- in the forward hemisphere ($\theta_{thrust} < 90^o$) or a μ^+ in the backward hemisphere ($\theta_{thrust} > 90^o$). The asymmetry is determined from

$$A_{FB}^b = \frac{N_{forw}^b - N_{back}^b}{N_{forw}^b + N_{back}^b}.$$

The number of forward b events N_{forw}^b is obtained by fitting the $p - p_t$ distribution to the 5 classes described above. Three more free parameters are added, namely:

- A_{FB}^b, the b quark asymmetry
- A_{FB}^c, the c quark asymmetry
- A_{FB}^h, the asymmetry of the resulting background

The likelihood function is defined as

$$L = -\sum_{i,j=1}^{i=n,j=m} -2N_{data}^{forward}(i,j)\log F^{forward}(i,j)$$

where $F^{forward}$ is defined as

$$F^{forward}(i,j) = R_{norm}\,[(1+A_{FB}^b)R_b\,N_{b\to\mu}(i,j) + (1+A_{FB}^{bc})R_b\,N_{b\to c\to\mu}(i,j)$$

$$+(1+A_{FB}^c)R_c\,N_{c\to\mu}(i,j)+(1+A_{FB}^h)R_{h\to\mu}\,N_{h\to\mu}(i,j)+(1+A_{FB}^h)R_{h\to\text{misid}}\,N_{h\to\text{misid}}(i,j)]$$

	Fit Method $p_t > 0$ GeV/c
$R_{h\to\text{misid}}$	0.95
R_c	1.029 ± 0.057
R_b	1.030 ± 0.025

Table 5.2: Result for 1991 data, p > 3 GeV/c

The number of hadrons in the data is normalised to the number in the simulation. To normalise the probability distribution to 1, the following equality holds:

$$\sum_{i,j} N_{data}^{forward}(i,j) = \sum_{i,j} F^{forward}(i,j)$$

From this equality, one more parameter is eliminated in the fitting procedure.

5.1.3 Determination of $\Gamma_{b\bar{b}}$

It is assumed that the decay of light hadrons into muons is correctly reproduced by the MC, i.e. $R_{h\to\mu}$ is always fixed to 1. Due to the generality of the fitting program, the branching ratio can be measured by three different methods:

1. In principle, a fit of the whole momentum and transverse momentum spectrum can yield R_b, R_c and $R_{h\to\text{misid}}$ at once. However, there are strong correlations in the low p, p_t region. Any problem with the MC in representing correctly the shape of the background propagates in the result of the partial width. This method does not work for the 1990 data, but for the 1991 data it gives compatible results with the other methods that are discussed below. The parameters obtained for 1991 data are given in Table 5.2.

2. To eliminate the background correlations, the background is first determined by a fit with R_b and R_c fixed to 1 in the low p_t region ($p_t <$ 0.5 GeV/c). Once the hadronic background is determined, it is fixed to the obtained value and R_b and R_c are fitted in the high pt region ($p_t > 0.6$ GeV/c). The result on R_b is very stable as a function of p_t. The results are tabulated in Table 5.3. The p_t and p distributions, showing the data points, the fit (histogram) and the different contributions are shown in Fig.5.3 for 1990 data and in Fig.5.4 for 1991 data. The five different muon sources are shown separately: the lowest lying histogram represents the muons from π and K decays, on top of this the misidentified hadrons are shown, the next contributions are the prompt muons

1990	Fit Method $p_t > 0.6$ GeV/c	Fit Method $p_t > 0.9$ GeV/c
$R_{h\to\text{misid}}$	0.97	0.97
R_c	1.083 ± 0.083	1.111 ± 0.137
R_b	1.015 ± 0.041	1.016 ± 0.040
1991	Fit Method $p_t > 0.6$ GeV/c	Fit Method $p_t > 0.9$ GeV/c
$R_{h\to\text{misid}}$	0.98	0.98
R_c	0.976 ± 0.053	0.951 ± 0.118
R_b	1.021 ± 0.029	1.040 ± 0.032

Table 5.3: Result for 1990 and 1991 data, p > 4 GeV/c (1990), p > 3 GeV/c (1991).

from c decays (double hatched) and the muons from the b to c cascade (hatched). The muons originating from a prompt b decay are shown by the blank histogram.

3. The sensitivity to R_c is very poor as can be seen in Table5.3 and its value is within statistical errors equal to 1. R_c is fixed to 1 and R_b is determined in the very high p_t region ($p_t > 0.8$ GeV/c). For a cut in p_t of 0.8 GeV/c, we obtain the value $R_b = 1.052 \pm 0.038$ and $R_b = 1.021 \pm 0.022$ for 1990 and 1991 data respectively. The dependence of R_b on the p_t value is shown in Fig.5.5.

The Peterson fragmentation parameter ϵ_b, used in the 1990 Monte Carlo and 1991 Monte Carlo, are 3 10^{-3} and 6 10^{-3}, respectively. The analysis is performed for different values for ϵ_b, by reweighting the MC sample of muons according to the z-value of the b event. If the hadronic background is fixed in the low p_t region and the b fraction is determined in the high p_t region, the method was found not to be sensitive to this ϵ_b parameter, because the ϵ_b effect is compensated by a different hadronic background scaling in the fit. However, for 1991 data a fit to the total p, p_t spectrum can be performed and their a minimum was found, both in the χ^2 and the likelihood value (the likelihood is here defined as being negative), for $\epsilon_b = 6.10^{-3}$. From another analysis of 1991 and 1992 data, ϵ_b has been determined to be $0.0059 \pm 0.0005(stat)$ [58]. In the analysis, we used $\epsilon_b = 5\ 10^{-3}$ in the 1990 MC and $\epsilon_b = 6\ 10^{-3}$ in the 1991 MC.

The partial width result for 1990 data is:

$$R_b = 1.052 \pm 0.038(stat)$$

This corresponds to a value of

$$\frac{\Gamma_{b\bar{b}}}{\Gamma_{had}} BR(b \to \mu) = 0.02283 \pm 0.00083(stat).$$

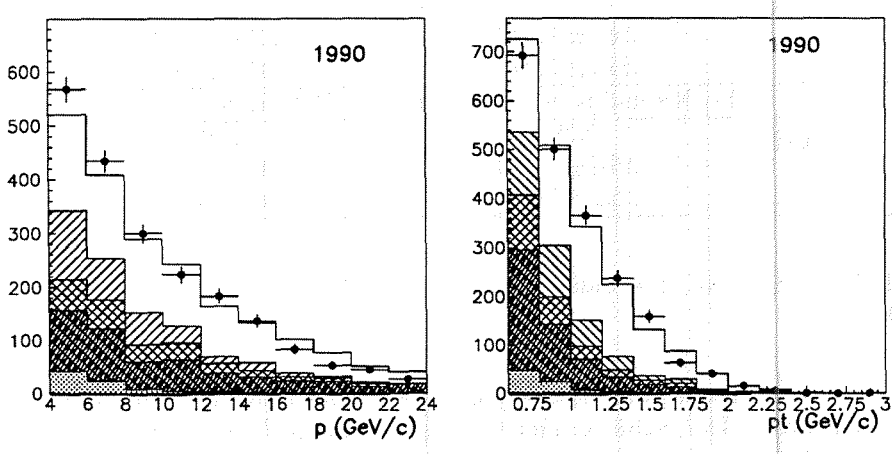

Figure 5.3: p (left) and p_t (right) distributions of muons $p_t > 0.6$ GeV/c for 1990 data.

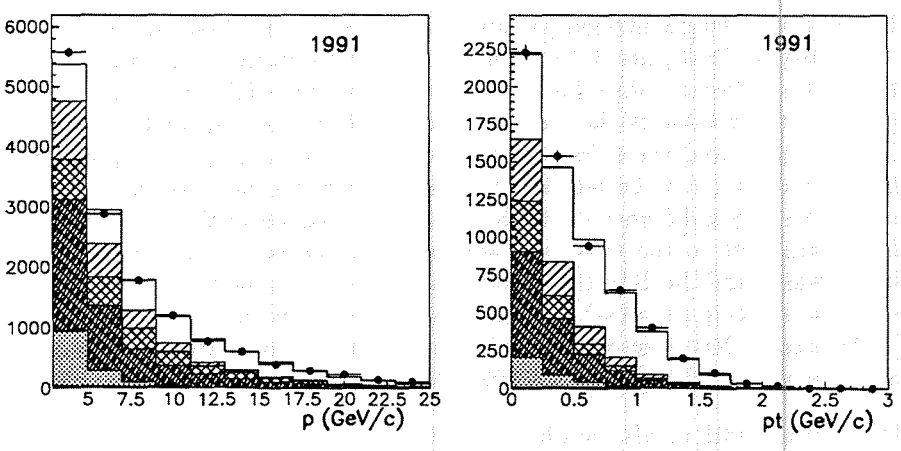

Figure 5.4: p (left) and p_t (right) distributions of muons $p_t > 0$ GeV/c for 1991 data.

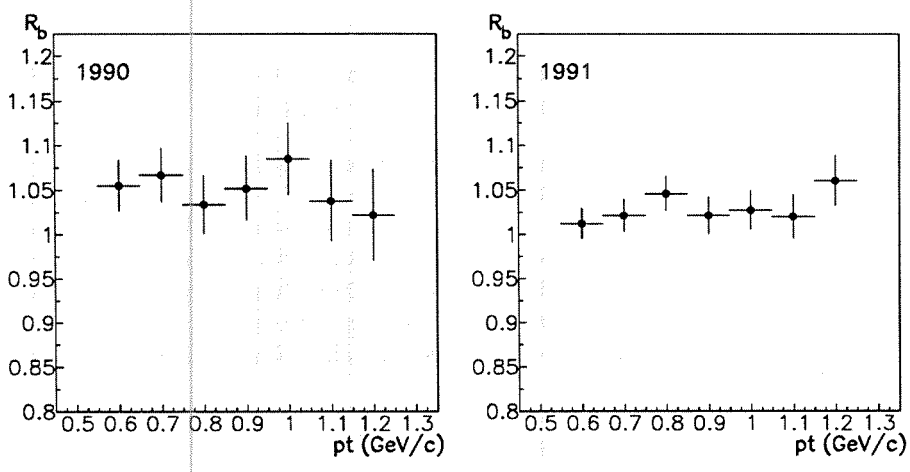

Figure 5.5: p_t dependence of R_b for 1990 (left) and 1991 (right) data.

The partial width result for 1991 data is:

$$R_b = 1.021 \pm 0.022(stat),$$

corresponding to a value of

$$\frac{\Gamma_{b\bar{b}}}{\Gamma_{had}} BR(b \to \mu) = 0.02216 \pm 0.00048(stat).$$

Combining the 1990 and 1991 results, the following value is found:

$$\frac{\Gamma_{b\bar{b}}}{\Gamma_{had}} BR(b \to \mu) = 0.02232 \pm 0.00048(stat)$$

Systematic error

The systematic error is evaluated by changing the variables, that may affect the partial width, by a certain amount, redoing the analysis and quoting the variation of the central value as contribution to the systematic error. The systematic error as tabulated below is obtained for the 1991 data for the analysis where R_c is fixed to unity and the b fraction is determined in the high p_t region.

The results are summarised in Table 5.4. The following systematic errors were studied:

- The mean semileptonic branching fraction of c into muons was varied: This inclusive branching ratio has a 1 σ error of 11 %.
- The fraction of leptons produced from B cascade decays was changed by 15%. CLEO measured the $BR(b \rightarrow c \rightarrow e)$ as $(9.7 \pm 0.8 \pm 0.6)\%$, at the Υ peak. Production of Λ_b and B_s states at LEP has the effect of altering this branching ratio, since the Λ_c and D_s states, arising dominantly from Λ_b and B_s decays, have smaller semileptonic branching fractions than the mixture of c hadrons from $B^{\pm}$ and B^0 decays. Therefore, an additional systematic error was added to the measured value of the semileptonic rate at the $\Upsilon(4S)$.
- The hadronic background was changed by 20 %.
- The Peterson fragmentation parameter ϵ_b was allowed to vary in the range $0.3\,10^{-3}$ to $0.7\,10^{-3}$.
- An uncertainty of 3 % on the efficiency of muon identification was included for remaining differences between data and the Monte Carlo simulation on the behaviour of the detector and the passage of muons through the calorimeters.
- The finite Monte Carlo statistics is not taken into account when doing the fit and is quoted as systematic error.
- The stability of the method has been verified by changing the condition of the fit. The muon minimum momentum was changed from 3 to 5 GeV/c and the bin size was changed.
- The analysis was redone using the pt_{out} variable instead of the pt_{in} variable.
- It was checked that the branching ratio determined from the barrel only and the forward region only, agreed within statistical error.

This measurement of the partial width using the semileptonic decay mode into muons, yields the result:

$$\frac{\Gamma_{b\bar{b}}}{\Gamma_{had}} BR(b \rightarrow \mu) = 0.02232 \pm 0.00048(stat) \pm 0.00135(syst).$$

Note that this measurement is dominated by the systematic error.

Source	Variation	error on R_b
direct charm	0.11	0.010
b cascade	0.15	0.015
hadronic background	0.20	0.015
μ-id efficiency	0.03	0.030
fragmentation ϵ_b	$4\ 10^{-3}$	0.020
p_t definition		0.030
varying p and p_t cut		0.025
binning of fit		0.010
finite Monte Carlo statistics		0.020
Total		0.062

Table 5.4: Systematic errors to R_b

5.1.4 Determination of the b forward-backward asymmetry

The same strategy as defined in 5.1.3 is followed to estimate the b forward-backward asymmetry. The asymmetry of the background A_{FB}^h is determined in the low p_t region by fixing A_{FB}^b and A_{FB}^c to its SM values. Fits show that the asymmetry of the background is indeed zero within one standard deviation. After having determined A_{FB}^h, the A_{FB}^b asymmetry is determined, together with R_b in the high p_t region. The asymmetry of the bc cascade class is set to $A_{FB}^{bc} = -c_1 A_{FB}^b$, with $c_1 = 0.77$, calculated with the JETSET Monte Carlo. It is due to the fact that the b quark may decay either into a c quark or into a $\bar{c}$ quark. The contributions of these two processes cancel partly, because of the opposite sign of the produced muons. The A_{FB}^c asymmetry is set to $A_{FB}^c = -c_2 A_{FB}^b$, where $c_2 = 0.88$ on the peak, as was determined from KORALZ [66].

By using this method, the forward-backward asymmetry is calculated in the detector acceptance. To obtain the asymmetry for the full solid angle, we have to correct for the limited acceptance. This correction is described in appendix C. It takes the value $Cor = 1.136$ for 1990 and $Cor = 1.107$ for 1991 data. For the 1990 data, the total hadronic sample is used, i.e. all data at all centre of mass energies. For 1991, only the data at a center of mass energy $\sqrt{s} = 91.28\,GeV$ are used. We do not dispose of enough events to measure the asymmetry as a function of the centre of mass energy. In 1991, the measured asymmetry is more stable as a function of the transverse momentum cut if the analysis is restricted to the muons with a momentum greater than 4 GeV/c. The stability of the A_{FB}^b measurement as a function of p_t is shown in Fig.5.6.

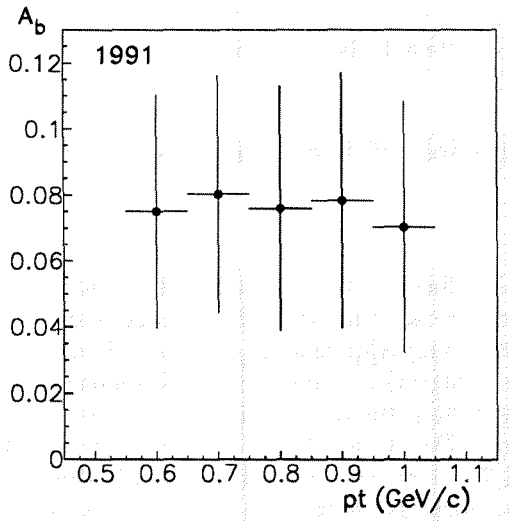

Figure 5.6: p_t dependence of the asymmetry A_{FB}^b for 1991 data.

The measured, acceptance corrected, asymmetry for 1990 and 1991 for a p_t cut of 0.8 GeV/c is:

$$1990 : A_{FB}^b = 0.105 \pm 0.048(stat) 1991 : A_{FB}^b = 0.076 \pm 0.038(stat) \quad (5.1)$$

Combining the 1990 and 1991 data, we measure an observed b asymmetry of

$$A_{FB}^b = 0.087 \pm 0.030(stat).$$

The relation between the quark asymmetry and the measured asymmetry is sensitive to the mixing in the $B_d^0 \bar{B}_d^0$ and $B_s^0 \bar{B}_s^0$ system. Therefore the experimentally determined asymmetry has to be corrected by a factor $(1 - 2\chi)^{-1})$, where χ is the mixing parameter. Using the LEP average of $\chi = 0.115 \pm 0.011$ [70, 71, 75], we finally obtain:

$$A_{FB}^b = 0.113 \pm 0.039(stat) \pm 0.004(mix)$$

Systematic errors

The following sources of systematic errors have been taken into account and their contributions to the asymmetry uncertainty are summarised in Table 5.5.

- The same analysis was repeated using pt_{out} instead of pt_{in}. The asymmetry changed by 0.6 %.
- The Peterson fragmentation parameter ϵ_b was changed in the range 4.10^{-3}–8.10^{-3}. This gives an almost negligible contribution to the total systematic error.
- The c fraction in the sample was changed by 11 %.
- The hadronic background was changed by 20 %.
- The factor c_1 was varied for the b cascade contributions.
- The factor c_2 was varied for the c asymmetry.
- The binning of the fit was changed.
- The contribution due to the finite Monte Carlo statistics was estimated to 0.4%.

Using the semileptonic decay mode into muons, the mixing corrected b asymmetry for 1990 and 1991 data is:

$$A_{FB}^b = 0.113 \pm 0.039(stat) \pm 0.013(syst) \pm 0.004(mix)$$

Source	Variation	Error on A^b_{FB}
p_t definition		0.006
fragmentation	$\epsilon_b = 4 - 8\ 10^{-3}$	0.0012
direct charm	0.11	0.003
hadronic background	0.20	0.003
c_2	$0.6 - 1.0$	0.0035
c_1	$0.6 - 1.0$	0.002
binning of fit		0.003
finite Monte Carlo statistics		0.004
Total		0.010

Table 5.5: Systematic errors to the b forward-backward asymmetry

Fit to the angular distribution

It it also possible to fit directly the angular distribution of the muons. The direction of the b quark is taken to be the thrust axis of the charged particles in the hadronic event. The orientation of the b quark is then calculated by multiplying $-\cos\theta_{thrust}$ with the muon charge. The distribution of the polar angle of the thrust axis is directly compared with the prediction of the standard model:

$$\frac{d\sigma}{d\cos\theta_b} \propto (1 + \cos\theta_b{}^2 + \frac{8}{3} A^b_{FB} \cos\theta_b) \tag{5.2}$$

A sample enriched in b quarks by asking a transverse momentum greater than 1 GeV/c is used. The background contribution (as given by the MC) is subtracted from the raw angular distribution and the observed asymmetry is then given by

$$A^b_{obs} = f_b A^b_{FB} + f_{bc} A^{bc}_{FB} + f_c A^c_{FB},$$

with f_b, f_{bc}, f_c, the fractions of prompt b, cascade bc and prompt c decay in the background subtracted sample with momentum greater than 1 GeV/c.

$$A^b_{obs} = f_b A^b_{FB} - f_{bc} c_1 A^b_{FB} - f_c c_2 A^b_{FB},$$

with $c_1 = 0.77$ and $c_2 = 0.88$.

A likelihood fit is performed on the angular distribution, using the expression (5.2) as probability distribution. The advantage of the likelihood fit is that no acceptance correction is needed and the raw angular distribution can be fitted after the background has been subtracted.The fractions f_b, f_c and f_{bc} are taken from the Monte Carlo. The result of this fit is

$$1990 \text{ all data} : A^b_{obs} = 0.075 \pm 0.040\ (stat)$$

$$1991 \text{ on peak} : A^b_{obs} = 0.054 \pm 0.029\ (stat)$$

This corresponds to a measured asymmetry of

$$1990 \text{ all data} : A^b_{FB} = 0.113 \pm 0.061\ (stat)$$

$$1991 \text{ on peak} : A^b_{FB} = 0.077 \pm 0.042\ (stat)$$

These results agree very well with the results that are obtained with the likelihood fit to the p, p_t distribution (5.1). The same results are obtained by performing a χ^2 fit, after having corrected for the angular acceptance of the detector. The acceptance corrected distributions, superimposed by the χ^2 fit are shown in Fig.5.7. The systematic errors are the same as listed in Table 5.5.

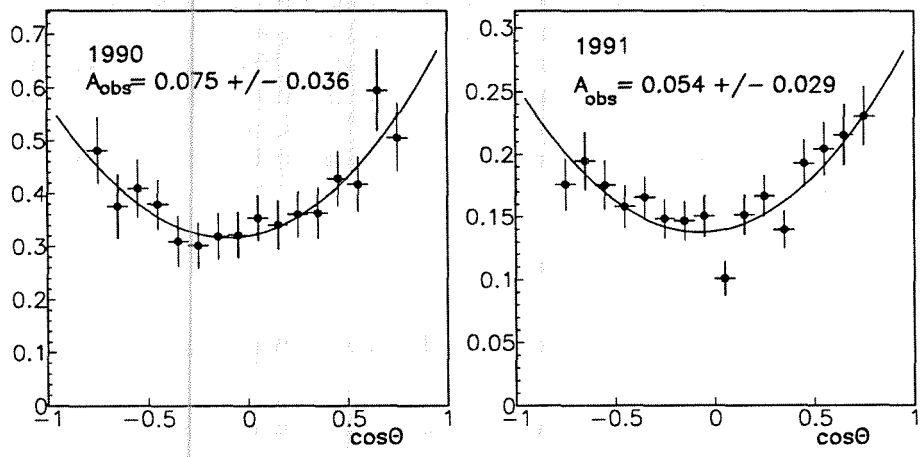

Figure 5.7: Angular distribution for $p_t > 1.$ GeV/c for 1990 and 1991 data.

5.2 Measurement of $\Gamma_{b\bar{b}}$ using a mixed tag method

The method for measuring $\Gamma_{b\bar{b}}/\Gamma_{had}$ which will be explained below, belongs to the category of double tag techniques. The advantage of such a method is the possibility to measure tagging efficiencies directly from the data. The method is based on the long lifetime of the B hadrons and on their heavy mass. The technique uses both the information from the high resolution microvertex detector and the transverse momentum of the muons. It uses all hadronic data and is less sensitive to the Monte Carlo simulation than the semileptonic methods.

Each hadronic event is geometrically split into two independent hemispheres according to the plane perpendicular to the thrust axis. The analysis is restricted to events, that are well contained in the barrel region, $|\cos\theta_{thrust}| < 0.70$, the angular acceptance of the microvertex detector. Only events for which all the barrel tracking detectors are at maximum efficiency are considered, i.e. the microvertex, the inner detector, the TPC and the outer detector. In addition, well functioning barrel muon chambers are required. The analysis has been performed on a sample of 198K hadronic events of the 1991 DELANA_E data and 584K hadronic events of the 1992 DELANA_C data. After the $\cos\theta_{thrust}$ cut, 119K hadronic events remained for the 1991 data, 396K for the 1992 data.

5.2.1 The microvertex tag

In this analysis, extra conditions are required on the track quality:

- The track has to be associated to at least 2 microvertex hits.
- The χ^2 p.d.f. of the fit of the track to the microvertex hits, has to be less than 2 if the number of microvertex hits equals 2.
- The χ^2 p.d.f. of the fit of the track to the microvertex hits, has to be less than 4 if the number of microvertex hits is greater than 2.

For each good track with momentum greater than 0.75 GeV/c, the projected lifetime signed impact parameter δ is calculated with respect to the beamspot (see chapter 4 on b tagging). The effective separation of a track from the primary vertex is better determined if the impact parameter is normalised to its resolution. The significance S is defined as the ratio:

$$S = \frac{\delta}{\sigma(\delta)}$$

The error on the impact parameter $\sigma(\delta)$ includes the contribution from both the track resolution and the beamspot size projected transverse to the track. It is defined as

$$\sigma^2(\delta) = \sigma_\epsilon^2 + \sigma_{B_x}^2 \sin^2\phi + \sigma_{B_y}^2 \cos^2\phi,$$

with σ_ϵ the impact parameter track error calculated from the track error matrix, ϕ is the azimuthal angle of the track and $\sigma_{B_{x,y}}$ the beamspot sizes in x and y. To suppress contributions from long-lived hadrons, such as Λ's and K's, tracks with an impact parameter $|\delta| > 1$ mm are rejected. The significance distribution for hadronic events in data (dots) and MC (histogram) is shown in Fig.5.8. The b events in the MC dominate the high significance region and are shown by the hatched histogram.

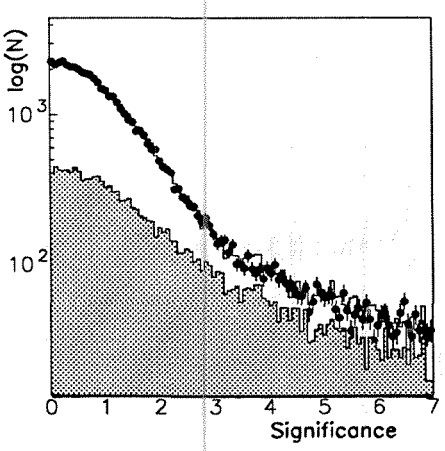

Figure 5.8: Significance distribution of data (dots) and MC (histogram)

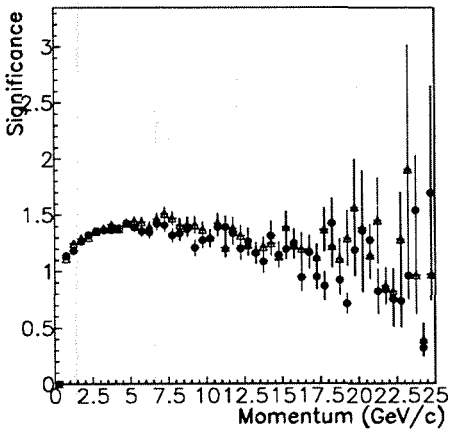

Figure 5.9: Momentum dependence of the mean significance.

The momentum, ϕ and θ dependence of this variable is shown in Figs.5.9 and 5.10. The dots are the data, the triangles are the MC. In the azimuthal distribution, obvious peaks for events oriented along the x-axis are seen. This results from the small size of the beamspot in y, which allows the significant impact parameter tracks to be more easily identified in this direction. The mean significance as a function of θ is rather flat, except at the edges of the acceptance region of the microvertex detector. Around $\theta = 90^o$, the mean significance for MC is slightly higher than in the data.

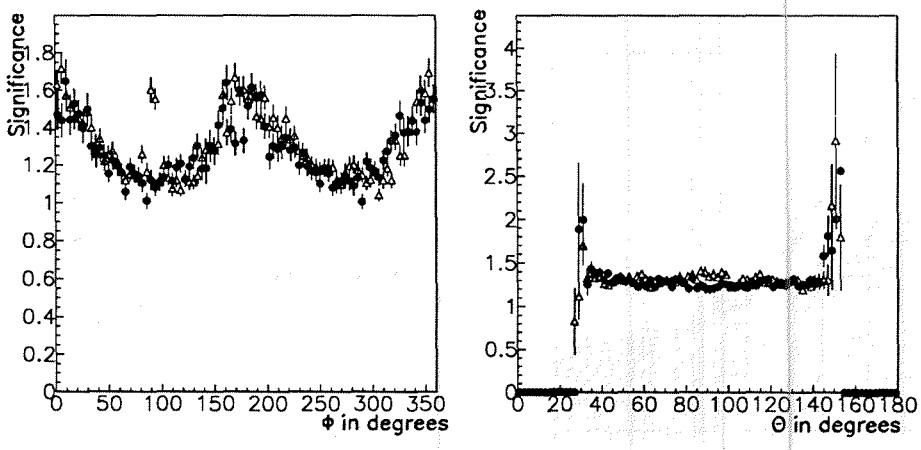

Figure 5.10: ϕ (left) and θ (right) dependence of the significance for 1991 data (dots) and 1991 MC (triangles).

The multiplicity is defined as the number of tracks per hemisphere with significance above 2. The DELANA_E MC, used for the 1991 data, was generated with a lifetime $\tau_B = 1.2$ ps for all B hadron species except the B baryons, which were produced with a lifetime of 1.3 ps. A correction to the decay distance of the B mesons is applied, such that the lifetime corresponds to 1.47 ps, the LEP average [76]. The agreement between data and Monte Carlo for the multiplicity of all hadronic events is shown in Fig.5.11.a. There is a slight disagreement between data and MC for high multiplicities. The filled histogram is the b multiplicity, which dominates at high multiplicities. The multiplicity distribution of one hemisphere for the three classes: b (filled dots), c (triangles) and uds (open dots) are shown in Fig.5.11.b. The three classes are well separated. It will be shown that the analysis is not sensitive to the detailed agreement of data and Monte Carlo events for the multiplicity.

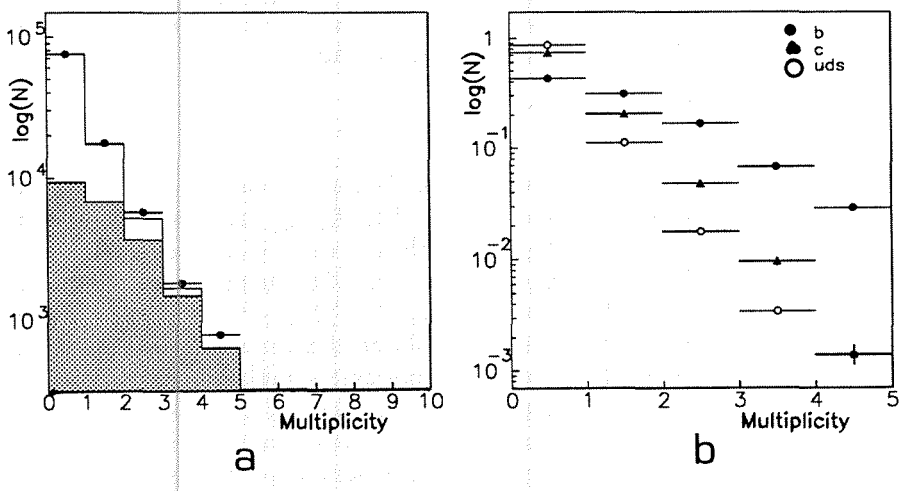

Figure 5.11: a)Multiplicity distribution of 1991 MC (line) and 1991 data (dots), the filled histogram are the b hemispheres.
b) Multiplicity distribution of b (filled dots), c (triangles) and uds (open dots) hemispheres.

5.2.2 The lepton tag

The tagging of b quarks by their semileptonic decay into muons is discussed in detail in the previous section. Samples of different b composition are selected by applying cuts on the transverse momentum pt_{in} of the muon. The sample composition is obtained by fitting the muon momenta and transverse momenta of the data to the MC. The procedure is explained in section 5.1.3.

5.2.3 Fitting procedure

The data are divided in three categories:

- *High p_t lepton sample* is the sample of the events tagged by a high transverse momentum muon ($p_t > 1$ GeV/c). This is an enriched b sample of around 80% b purity.
- *Low p_t lepton sample* is composed of the events tagged by a low transverse momentum muon ($p_t < 1$ GeV/c). This is a sample of composition roughly 50% b events, 25% c events and 25% *uds* events.
- *Hadronic sample:* all hadronic events.

It is assumed that he relative composition of the high p_t and low p_t samples is known with respect to the hadronic sample: if f'_b, f'_c, f'_{uds}, are the b, c and *uds* fractions of the high p_t sample, f''_b, f''_c, f''_{uds}, the b, c and *uds* fractions of the low p_t sample and f_b, f_c, f_{uds} the b, c and *uds* fractions of the hadronic sample, then the ratios $\alpha' = f'_b/f_b, \alpha'' = f''_b/f_b, \beta' = f'_c/f_c, \beta'' = f''_c/f_c, \gamma' = f'_{uds}/f_{uds}, \gamma'' = f''_{uds}/f_{uds}$ are fixed to the composition as obtained from a fit from the data to the Monte Carlo. The c fraction in the hadronic sample is fixed to its SM value, i.e. $\Gamma_{c\bar{c}}/\Gamma_{had} = 0.171$. Using the three samples, f_b and the multiplicity distributions for the b, c and *uds* hemispheres can be extracted. We do not rely at this stage on any MC related to the impact parameter distributions. The hemisphere multiplicity distributions are binned in 5 bins. Hemispheres with multiplicity bigger than 4 are collected in bin 5 to avoid bins with low statistics. The c and *uds* events have to be in a different class, because the D mesons have a longer lifetime than the hadrons from *uds* events. If the classes c and *uds* would be joined into one class *udsc*, the high and low p_t samples would not be characterised by the same *udsc* multiplicity distribution, because the fraction of D mesons is different in the two samples.

In total, there are 13 free parameters in the fit. the multiplicity distributions for b, c and *uds* events are each normalised to 1:

- f_b, the b fraction in the hadronic sample.
- $M_b^{hem}(i)$, the hemisphere multiplicity distribution of b hemispheres.
- $M_c^{hem}(i)$, the hemisphere multiplicity distribution of c hemispheres.
- $M_{uds}^{hem}(i)$, the hemisphere multiplicity distribution of uds hemispheres.

The following relation holds between the parameters

$$\sum_{i=1,5} M_b^{hem}(i) = \sum_{i=1,5} M_c^{hem}(i) = \sum_{i=1,5} M_{uds}^{hem}(i) = 1$$

In addition, the following equations should remain fulfilled during the fitting procedure:

$$\begin{aligned} \alpha' f_b + \beta' f_c + \gamma' f_{uds} &= 1 \\ \alpha'' f_b + \beta'' f_c + \gamma'' f_{uds} &= 1 \\ f_b + f_c + f_{uds} &= 1 \end{aligned}$$

For all bins i, the following equalities hold:

$$\begin{aligned} M_{hpt}^{hem}(i) &= \alpha' \mathbf{f_b} M_b^{hem}(i) + \beta' f_c M_c^{hem}(i) + \gamma'(1 - \alpha' \mathbf{f_b} - \beta' f_c) M_{uds}^{hem}(i) \\ M_{lpt}^{hem}(i) &= \alpha'' \mathbf{f_b} M_b^{hem}(i) + \beta'' f_c M_c^{hem}(i) + \gamma''(1 - \alpha'' \mathbf{f_b} - \beta'' f_c) M_{uds}^{hem}(i) \\ M_{had}^{hem}(i) &= \mathbf{f_b} M_b^{hem}(i) + f_c M_c^{hem}(i) + (1 - \mathbf{f_b} - f_c) M_{uds}^{hem}(i) \end{aligned} \quad (5.3)$$

In (5.3) there are 15 equations, but 3 of them are linear combinations of 4 others. One has 13 parameters and only 12 independent equations, therefore the c multiplicity distributions has been parametrized in terms of the b distribution. An exponential form, as determined from the MC, was used:

$$M_c^{hem}(i) = p_1 exp(-p_2) M_b^{hem}(i)$$

The parameter p_1 is completely fixed by the relation $\sum_i M_c^{hem}(i) = 1$. The parameter p_2 was allowed to vary in a 10% range around the Monte Carlo value. The ratio $M_c^{hem}(i)/M_b^{hem}(i)$ as taken from the MC, together with the parametrisation is shown in Fig.5.12.

This set of equations is solved by constructing a χ^2 function. The right-hand side of the equations (5.3), $F_{hpt}(i)$, $F_{lpt}(i)$ and $F_{had}(i)$, is the probability that a hemisphere of that sample belongs to bin i. The function that has to be minimised, is:

$$\sum_i [\frac{(M_{hpt}^{hem}(i) - F_{hpt}(i))^2}{\sigma^2_{M_{hpt}}} + \frac{(M_{lpt}^{hem}(i) - F_{lpt}(i))^2}{\sigma^2_{M_{lpt}}} + \frac{(M_{had}^{hem}(i) - F_{had}(i))^2}{\sigma^2_{M_{had}}}]$$

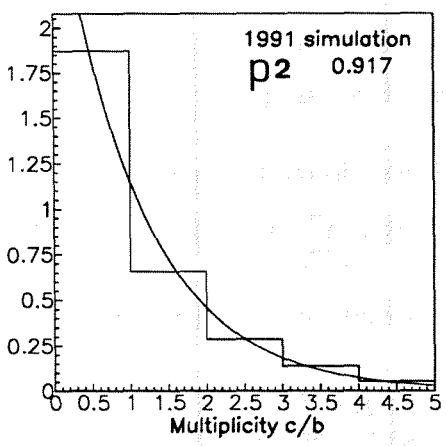

Figure 5.12: The ratio $M_c^{hem}(i)/M_b^{hem}(i)$

5.2.4 Determination of the partial width

The method has been tested on the 1991 and 1992 Monte Carlo samples. The level of accuracy which can obtained for the b, c and uds multiplicities is shown in Fig.5.13 and Fig.5.14. The multiplicity distributions as taken from the Monte Carlo are shown by the triangles, the multiplicity distributions obtained by this method is shown by the dots. The fit method reproduces the input b fraction within 1%.

The $Z^0 \rightarrow b\bar{b}$ event fraction after applying the hadronic event selection was found to be $1.2 \pm 0.1\%$ higher than at the generation level in the Monte Carlo simulation. The data are corrected accordingly and a 0.2% systematic error is included for this effect.

The 1991 data yield the result:

$$R_b = \frac{\Gamma_{b\bar{b}}}{\Gamma_{had}} = 0.2173 \pm 0.0097(stat),$$

$$\chi^2/ndf = 1.93$$

The fit of the three samples, is shown in Fig.5.15. The filled histogram is the

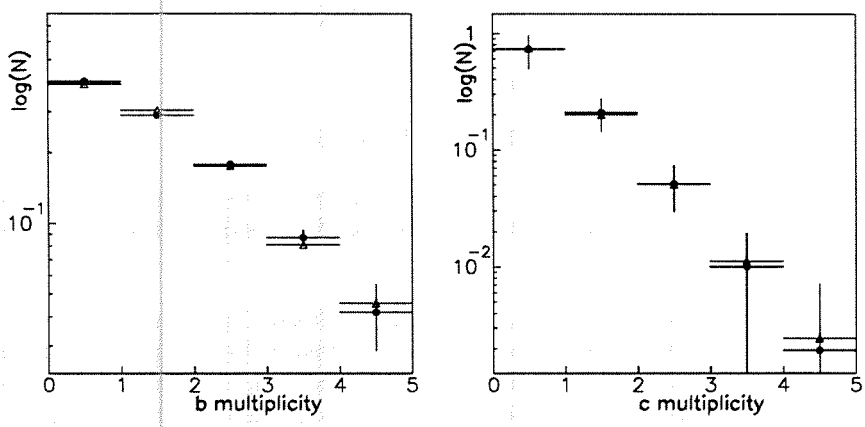

Figure 5.13: b and c multiplicity distribution of MC (triangles) and fit (dots)

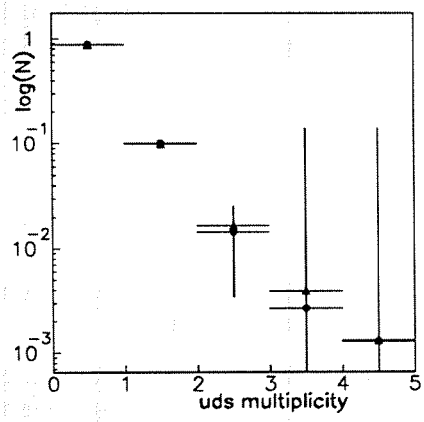

Figure 5.14: *uds* multiplicity distribution of MC (triangles) and fit (dots)

b multiplicity, the hatched part is the c multiplicity and the rest is the uds multiplicity.

The 1992 data yield the result:

$$R_b = \frac{\Gamma_{b\bar{b}}}{\Gamma_{had}} = 0.2197 \pm 0.0064(stat),$$

$$\chi^2/ndf = 0.42$$

The fit of the hadronic sample is shown in Fig.5.16.

The relatively large statistical error as compared to other recent measurements is due to the error propagation of the b and the uds multiplicity distributions to the b fraction.

The systematic errors can be split in three classes: the systematic error related to the fit method, the systematic error caused by the uncertainty in the lepton sample composition, and the one related to the uncertainty on the c fraction. The advantage of this method is that no lifetime related systematic error has to be included. Indeed, if the impact parameter distributions are taken from the MC, a certain lifetime of the B and D hadrons has been assumed. In this method, the multiplicity distributions are extracted directly from the data, without any lifetime assumption. Another systematic error which is eliminated with this method, is the uncertainty on the multiplicity of b events. Since the branching fractions of the different decay channels of B hadrons are still poorly determined, the number of particles produced in B decays is not well known.

Checks on the fitting method

The following checks were done:

- The analysis was repeated with other significance cuts: for $S > 1.5$ and for $S > 2.5$. R_b changed by at most 0.002.
- The analysis was redone with other track selection criteria. Tracks with an impact parameter greater than 1.5 mm were rejected. R_b changed by 0.0007.
- The cut on the thrust axis was narrowed to $|\cos\theta_{thrust}| < 0.65$, the track quality cuts were varied. This changed R_b by maximally 0.0015.
- Above the assumption is made that the c multiplicity can be parametrised by the b multiplicity multiplied by an exponential. This ratio has a reduced sensitivity to the resolution of the detector and the beamspot. The value of

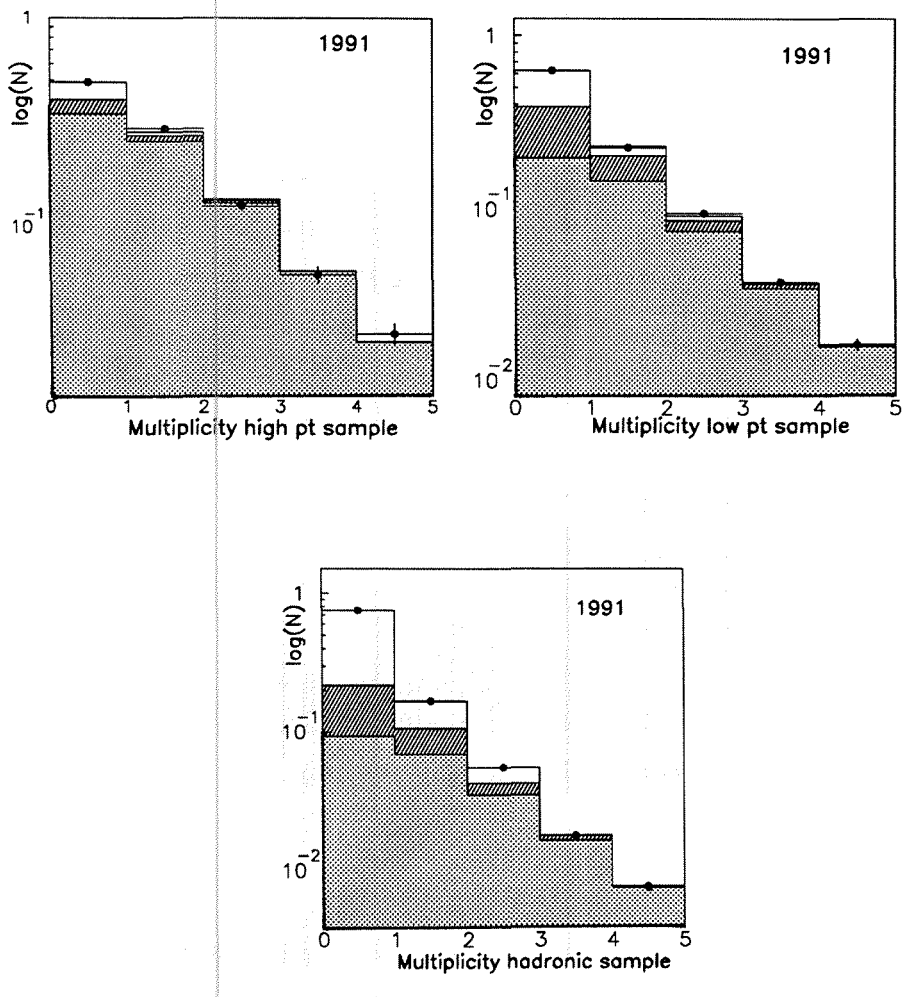

Figure 5.15: Multiplicity distributions for 1991 data of low p_t sample, high p_t and hadronic sample. The dots are the data, the histogram is the fit.

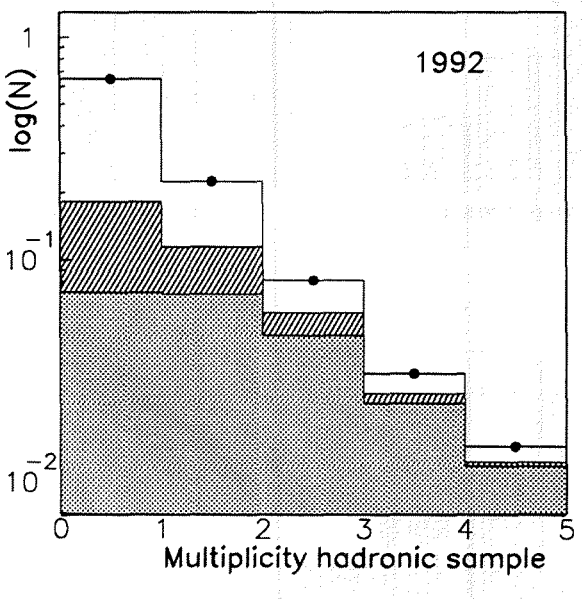

Figure 5.16: Multiplicity distribution of hadronic sample for 1992 data.

the exponent, which is fitted, is sensitive to the difference in lifetime of the B and D hadrons. The uncertainty is estimated by performing the analysis on the Monte Carlo with the same parametrisation, and comparing the central value with the analysis done with the c distribution as given by the MC. R_b changed by 0.002.

c uncertainties

The charm fraction is fixed to its Standard Model value, changing the charm fraction by +11% varies R_b by -0.004.

Uncertainty in relative sample composition

The uncertainty on the muon sample composition propagates into the measurement of the partial width. The same systematic uncertainties were assumed as in the single muon tag analysis.

- The uncertainty in the semileptonic branching ratio of the c quark into muons is assumed to be 11%. Changing this semileptonic branching ratio by +11%, changes the b fraction in the high and low p_t sample by -0.47% and -0.8% respectively. The c fraction in the high and low p_t sample rises by +0.5% and +1.3%, respectively.
- The uncertainty in the semileptonic branching ratio of the b quark is taken to be +10%. This raises the b fraction in the high and low pt sample by $\sim$ 1.1%.
- The b cascade contribution has an uncertainty of +15%. This has almost no effect on the high p_t sample composition, but changes the b fraction in the low p_t sample by +1.15%.
- An uncertainty of +20% has been taken for the background in the muon sample. The b fraction diminishes by 1.35% in the high p_t sample and by 1.5% in the low p_t sample. The amount of misidentified hadrons in the b events, has almost no effect on the R_b measurement (changing the background in the b events by +20%, lowers R_b by 0.0004).
- The efficiency of the muon identification has been varied by 3%.
- The Peterson fragmentation parameter ϵ_b was changed from 0.4 10^{-3} to 0.8 10^{-3}. The events were reweighted according to their z-value.

	error on R_b
sample composition	
background	0.0040
$b \rightarrow c \rightarrow \mu$	0.0044
$b \rightarrow \mu$	0.0021
$c \rightarrow \mu$	0.0028
μ efficiency	0.0001
b fragmentation	0.0020
total sample composition	0.0072
fit method and events selection	
fit method and event selection	0.0033
c uncertainties	
c parametrisation	0.0018
c fraction	0.004
Total	0.0090

Table 5.6: Systematic error on $\Gamma_{b\bar{b}}/\Gamma_{had}$

The above uncertainties will change the sample compositions of the high and low p_t samples by maximally 1.5% and will influence the $\Gamma_{b\bar{b}}/\Gamma_{had}$ measurement as shown in Table 5.6. Note that the uncertainties on the different b and c branching ratios are taken conservatively in order to be compatible with the previous analysis. Recently, the different errors on b and c branching ratios all went down to $\sim$ 6 % and this will improve the systematic error considerably.

Combining the 1991 and 1992 measurements of $\Gamma_{b\bar{b}}/\Gamma_{had}$, yields the result:

$$\Gamma_{b\bar{b}}/\Gamma_{had} = 0.2190 \pm 0.0053(stat) \pm 0.0090(syst)$$

The large statistical error is due to the propagation of the error on the b and uds multiplicity distribution to the error on $\Gamma_{b\bar{b}}/\Gamma_{had}$.

5.3 Discussion of the results

5.3.1 The partial width into bottom quarks

Two different methods were discussed for extracting the b partial width of the Z^0 resonance. The first one (section 5.1.3), using a single lepton tag, determines the product of the partial width and the b semileptonic branching ratio into

muons.

$$\Gamma_{b\bar{b}}/\Gamma_{had} BR(b \rightarrow \mu) = 0.02232 \pm 0.00048(stat) \pm 0.00135(syst)$$

This measurement is dominated by the systematic error, especially by the modelling of the semileptonic decays in the Monte Carlo. When extracting $\Gamma_{b\bar{b}}/\Gamma_{had}$ from this measurement, one has to introduce an additional systematic error due to the uncertainty on the semileptonic $b \rightarrow \mu$ branching ratio. No attempt was made to extend this method to the so-called "double" lepton tag, where events containing two leptons are classified separately and are used to determine the $b \rightarrow c \rightarrow l$ and the $b \rightarrow l$ branching ratios in the same fit. The statistics of collected data (1990-1991) was, at the time when this analysis was performed, still rather low to perform such a double lepton tag analysis. This has now been done for the 1991-1992 DELPHI semileptonic analysis [58]. The preliminary result for 1991-1992 DELPHI data is

$$\Gamma_{b\bar{b}}/\Gamma_{had} = 0.222 \pm 0.009(stat) \pm 0.004(syst).$$

In a second analysis, using an impact parameter method, the b partial width was determined to be

$$\Gamma_{b\bar{b}}/\Gamma_{had} = 0.2190 \pm 0.0053(stat) \pm 0.0090(syst).$$

This measurement has a smaller systematic error as compared to the first method, therefore it is more promising for future measurements. The error on this measurement is comparable to the one of the double lepton tag analysis of 1991-1992. However, when introducing the more recent uncertainties on b and c branching fractions, the systematic error will further go down.

The hadronic width of the Z^0 has been measured with high precision at LEP [13]. Using the value of $\Gamma_{had} = 1740.3 \pm 5.9$ MeV, the partial width of the Z^0 into a bottom quark-antiquark pair is

$$\Gamma_{b\bar{b}} = 381 \pm 21 \text{MeV}$$

Both measurements are in agreement with the SM value $R_b = 0.217$, which is for a top mass of 150 GeV and a Higgs mass of 300 GeV. From this measurement, it is also ruled out that the b quark does belong to a weak isospin singlet. If the b quark would have an isospin $I_3^b = 0$, $\Gamma_{b\bar{b}}$ would have a value of ~ 30 MeV.

5.3.2 Inclusive semileptonic branching ratio of b quarks into muons

Combining the results of the two analyses, the b semileptonic branching ratio into muons is estimated to

$$BR(b \to \mu) = 10.19 \pm 0.33(stat) \pm 0.51(uncorr.syst) \pm 0.09(corr.syst)\%$$

Hereby, the statistical error of the two measurements is assumed to be uncorrelated (This is not really the case, because the events containing a semileptonic decay are used in both analyses, but these events are only a small fraction of the total sample in the mixed analysis.). Both measurements have a common systematic error: the uncertainty on the sample composition. The systematic error of both measurements is split in an uncorrelated part and a completely correlated systematic error. The errors are propagated by using a 2*2 error matrix of the two measurements.

5.3.3 The b forward-backward asymmetry and the effective weak mixing angle

The b asymmetry as determined from the 1990 and 1991 data is determined to be (section 5.1.4)

$$A_{FB}^{b} = 0.113 \pm 0.039(stat) \pm 0.013(syst) \pm 0.004(mix)$$

At the Z^0 resonance, neglecting QED and QCD effects and the mass of the b quark, the b asymmetry can be written as:

$$A_{FB}^{0}(M_Z^2) = \frac{3(1-4\sin^2\theta_{eff})}{1+(1-4\sin^2\theta_{eff})^2} \times \frac{(1-\frac{4}{3}\sin^2\theta_{eff})}{1+(1-\frac{4}{3}\sin^2\theta_{eff})^2}. \qquad (5.4)$$

The measured asymmetry is related to A_{FB}^{0} by

$$A_{FB}^{b} = A_{FB}^{0} + \Delta_E + \Delta_{QED} + \Delta_{QCD}.$$

The ZFITTER program [74] is used to determine the QED (Δ_{QED}), QCD (Δ_{QCD}) and energy (Δ_E) corrections in the framework of the SM. The following input parameters were taken:

$$\begin{aligned} M_{Higgs} &= 300 \text{ GeV/c}^2 \\ M_{top} &= 150 \text{ GeV/c}^2 \\ \alpha_s^{LEP} &= 0.123 \\ M_Z &= 91.187 \pm 0.007 \text{ GeV/c}^2 \end{aligned}$$

	Δ_b asymmetry
Δ_{QED}	-0.004
Δ_{QCD}	-0.003
Δ_E	$+0.002$

Table 5.7: b asymmetry corrections

The 1991 data were taken at a centre of mass energy of 91.27 GeV/c^2, a correction of Δ_E is applied to the b asymmetry to take into account this shift of 100 MeV/c^2 with respect to the Z^0 mass. The Δ_E, Δ_{QED} and Δ_{QCD} corrections are given in Table 5.7.

The measured asymmetry corresponds to an asymmetry at the peak of $A^0_{FB} = 0.118 \pm 0.039 \pm 0.014$. Translating this measurement into a measurement of the effective weak mixing angle, $\sin^2\theta_{eff}$ is determined to be:

$$\sin^2\theta_{eff} = 0.2289 \pm 0.0069(stat) \pm 0.0024(syst)$$

The measurement of the effective weak mixing angle is compatible with the SM predicted value of 0.2330. The DELPHI b forward-backward analysis for 1991 and 1992 data measures an effective weak mixing angle of $\sin\theta_{eff} = 0.2303 \pm 0.0035$.

This measurement of the b forward-backward asymmetry is in good agreement with the SM, which predicts a b asymmetry at the Z^0 peak of 0.087 for a top mass of 150 GeV/c^2, a Higgs mass of 300 GeV/c^2 and a strong coupling constant of 0.123. The prediction changes by 0.005 for a 50 GeV/c^2 variation in the top mass, or a factor of ten variation in the Higgs mass (100 to 1000 GeV/c^2). Our measurement is also in agreement with the preliminary DELPHI measurement of the b asymmetry for 1991 and 1992 data of $0.105 \pm 0.016(stat) \pm 0.011(syst) \pm 0.003(mixing)$ [59].

From the b forward-backward asymmetry it is also clear that the b quark does not belong to an isospin singlet ($I^b_3 = 0$). Indeed, equation (1.44) and (1.45) shows that, an isospin singlet would give a b asymmetry $A^b_{FB} = 0$ at the Z^0 peak. Hence, the b quark must have an isospin partner, the top quark.

	ALEPH 90-92 prel.	DELPHI 91-92 prel.	L3 90-91 prel.	OPAL 90-91 prel.
	[63]	[58]	[69]	[65]
$\Gamma_{b\bar{b}}/\Gamma_{had}$	0.2223	0.222	0.2184	0.221
Stat.error	0.0042	0.009	0.0081	0.004
Uncorr.sys.	0.0033	0.002	0.0045	0.008
Common sys.	0.0046	0.004	0.0059	0.006
LEP average	$0.221 \pm 0.003 \pm 0.002 \pm 0.005$			

Table 5.8: $\Gamma_{b\bar{b}}/\Gamma_{had}$ from lepton tags

	ALEPH 90-91	DELPHI 90-91	L3 91
	[64]	[49]	[50]
$\Gamma_{b\bar{b}}/\Gamma_{had}$	0.228	0.232	0.222
Stat.error	0.005	0.005	0.003
Uncorr.sys.	0.005	0.011	0.002
Common sys.	0.001	0.013	0.006
LEP average	$0.226 \pm 0.002 \pm 0.003 \pm 0.004$		

Table 5.9: $\Gamma_{b\bar{b}}/\Gamma_{had}$ from event shapes

5.4 Comparison with other LEP experiments

In Tables 5.8, 5.9 and 5.10 the measurements of the partial width into bottom quarks from the different LEP experiments are shown with their statistical and systematic error [13]. The measurements of the b partial width are given separately according to the method that was used: the lepton tag, the event shape tag or the lifetime tag. Combining all measurements and assuming the result of the three tagging categories to be entirely uncorrelated, the LEP average is

$$\Gamma_{b\bar{b}}/\Gamma_{had} = 0.2200 \pm 0.0027$$

This measurement is very close to the 1% level, needed for probing new physics. The measurements based on a double tagging of impact parameters, which have the lowest systematic error, are very promising to reach this 1% level.

The LEP measurements for the $b\bar{b}$ quark asymmetry, obtained from analyses using the semileptonic decay mode of the b quark, are tabulated in Table 5.11. The b forward-backward asymmetry from the LEP experiments, based on an

	ALEPH 92	DELPHI 91-92 prel.	DELPHI 91 prel.	OPAL 90	OPAL 91-92 prel.
	[62]	[61]	[53]	[67]	[68]
$\Gamma_{b\bar{b}}/\Gamma_{had}$	0.2192	0.206	0.222	0.222	0.2133
Stat.error	0.0022	0.0066	0.007	0.007	0.0041
Uncorr.sys.	0.0020	0.0037	0.0063	0.008	0.0027
Common sys.	0.0023	0.0047	0.003	0.002	0.0033
LEP average	$0.2169 \pm 0.0018 \pm 0.0015 \pm 0.0027$				

Table 5.10: $\Gamma_{b\bar{b}}/\Gamma_{had}$ from lifetime tags

inclusive measurement, are shown in Table 5.12. In the inclusive measurement, the b events are tagged by an impact parameter technique and the hemisphere jet-charge algorithm is used to obtain the b quark direction. The jet-charge is the momentum weighted charge of all final state hadrons per hemisphere. It reflects the charge of the initial quark. The LEP average for the bottom forward-backward asymmetry is

$$A_{FB}^{b\bar{b}} = 0.094 \pm 0.005 \pm 0.002 \pm 0.003$$

The LEP average of the effective weak mixing angle as obtained from the b asymmetry is 0.2322 ± 0.0011 [13]. The b asymmetry determines the weak mixing angle with almost the same precision as the forward-backward asymmetry of leptons at LEP (0.2318 ± 0.0010). All these measurements are in good agreement with the SM prediction of $\sin\theta_{eff} = 0.2330$.

The $\Gamma_{b\bar{b}}$ measurement can be combined with other electroweak variables and an estimate of the top quark mass can be derived. This was done by the LEP electroweak working group [13]. Combining the measurements of the four LEP experiments, one obtains a prediction for the top quark mass of $M_{top} = 166^{+17+19}_{-19-22}$ GeV/c^2.

	ALEPH l, high p_t 90-92 prel.	DELPHI μ, high p_t 91-92 prel.	L3 l 90-92 prel.	OPAL l 90-91
	[70]	[59]	[71]	[72]
$A_{FB}^{b\bar{b}}(\%)$	8.1	10.2	9.1	9.1
Stat.error	1.0	1.6	1.0	1.8
Uncorr.sys.	0.1	0.9	0.5	0.4
Common sys.	0.3	0.8	0.3	0.6

Table 5.11: $A_{FB}^{b\bar{b}}$ from lepton tags (in %)

	ALEPH 92 prel.	DELPHI 91-92 prel.
	[73]	[60]
$A_{FB}^{b\bar{b}}(\%)$	10.9	11.6
Stat.error	1.2	1.9
Uncorr.sys.	0.5	1.7
Common sys.	0.2	1.0

Table 5.12: $A_{FB}^{b\bar{b}}$ from lifetime tags (in %)

Conclusions

From a sample of about one million Z^0 events, collected by the DELPHI experiment at LEP during the runs of 1990, 1991 and 1992, the hadronic decay mode of the Z^0 resonance is selected and the sample is enriched in bottom quark events. On this sample, precision measurements of bottom quark production in Z^0 decays are carried out. The analyses presented in this work, measure the Z^0 to $b\bar{b}$ branching ratio, the inclusive semileptonic branching ratio of b quarks into muons and the b forward-backward asymmetry.

The analyses use the semileptonic decay of B hadrons into muons. Therefore, a detailed study of the muon identification properties of the DELPHI detector is made. Various systematic errors are traced down and corrected for. A muon identification algorithm is developed, which provides an optimum between muon detection efficiency and muon sample purity in hadronic events. The identification efficiency of muons in these events, is estimated to be 81%, with a misidentification probability of 0.8%. This corresponds to a muon purity of 73%.

The hadronic events are enriched in b events by using the fact that a b quark has a high mass, a hard fragmentation and a long lifetime.

In a first analysis, performed on the 1990 and 1991 data, the product of the branching ratio $b \rightarrow \mu$ with $\Gamma_{b\bar{b}}/\Gamma_{had}$ and the b forward-backward asymmetry is determined. This method is based on a fit of the momenta and transverse momenta of the muons in a hadronic event to the same distributions in the Monte Carlo. The measured values are

$$\frac{\Gamma_{b\bar{b}}}{\Gamma_{had}} BR(b \rightarrow \mu) = 0.02232 \pm 0.00048(stat) \pm 0.00135(syst)$$

$$A_{FB}^{b} = 0.113 \pm 0.039(stat) \pm 0.013(syst) \pm 0.004(mix)$$

In a second analysis, made on the 1991 and 1992 data, the transverse momentum of the muon with respect to the jet axis, is used to determine the

relative b, c and uds compositions with respect to the hadronic composition. By counting the number of tracks with a high impact parameter in the opposite hemisphere with respect to the tagged muon, we are able to extract the $Z^0 \rightarrow b\bar{b}$ branching ratio, in an almost Monte Carlo independent way,

$$\Gamma_{b\bar{b}}/\Gamma_{had} = 0.2190 \pm 0.0053(stat) \pm 0.0090(syst).$$

Combining the two measurements of the b branching fraction, we determine the inclusive semileptonic decay fraction of the b quark. The effective weak mixing angle is determined from the b forward-backward asymmetry.

$$BR(b \rightarrow \mu) = 10.19 \pm 0.33(stat) \pm 0.52(syst)\%$$

$$\sin^2 \theta_{eff} = 0.2289 \pm 0.0069(stat) \pm 0.0024(syst)$$

All the measurements described in this thesis, are in excellent agreement with the Standard Model predictions. It is clear that, with the present experimental accuracy, there is no reason to doubt the validity of the Standard Model as the theory for describing electroweak interactions.

Part IV

Appendices

Appendix A

Muon chamber resolution

The resolution of the muon chambers can be estimated by making the difference of the coordinate of the extrapolated track with the measured coordinate in the muon chamber (residual). This is shown for 1991 muon pair data in Fig.A.1 in the barrel and the forward muon chambers. The resolution of the barrel muon chambers in the $R\phi$ and z coordinate is shown in the two upper plots. The lower two plots are the resolution of the drift coordinate and the delay line coordinate in MUF. The fitted variance is the quadratic sum of the error on the measured coordinate and the error on the extrapolated coordinate. The error on the extrapolated coordinate is the combination of the propagation of the tracking errors and the multiple scattering error. This error on the extrapolated coordinate is dependent on the polar angle and is for a 45 GeV muon between 4 mm and 9 mm for MUB (mean value for $R\phi = 5$ mm, for $z = 5.9$ mm) and between 4 mm and 15 mm (mean value 6.6 mm) for MUF. By taking this mean value as error on the extrapolated track, the following resolutions are obtained:

$$\text{MUB } \sigma_{R\phi} = 3\text{ mm} \tag{A.1}$$

$$\text{MUB } \sigma_{z} = 1.8\text{ cm} \tag{A.2}$$

$$\text{MUF } \sigma_{\text{drift}} = 4\text{ mm} \tag{A.3}$$

$$\text{MUF } \sigma_{\text{delay}} = 5\text{ mm} \tag{A.4}$$

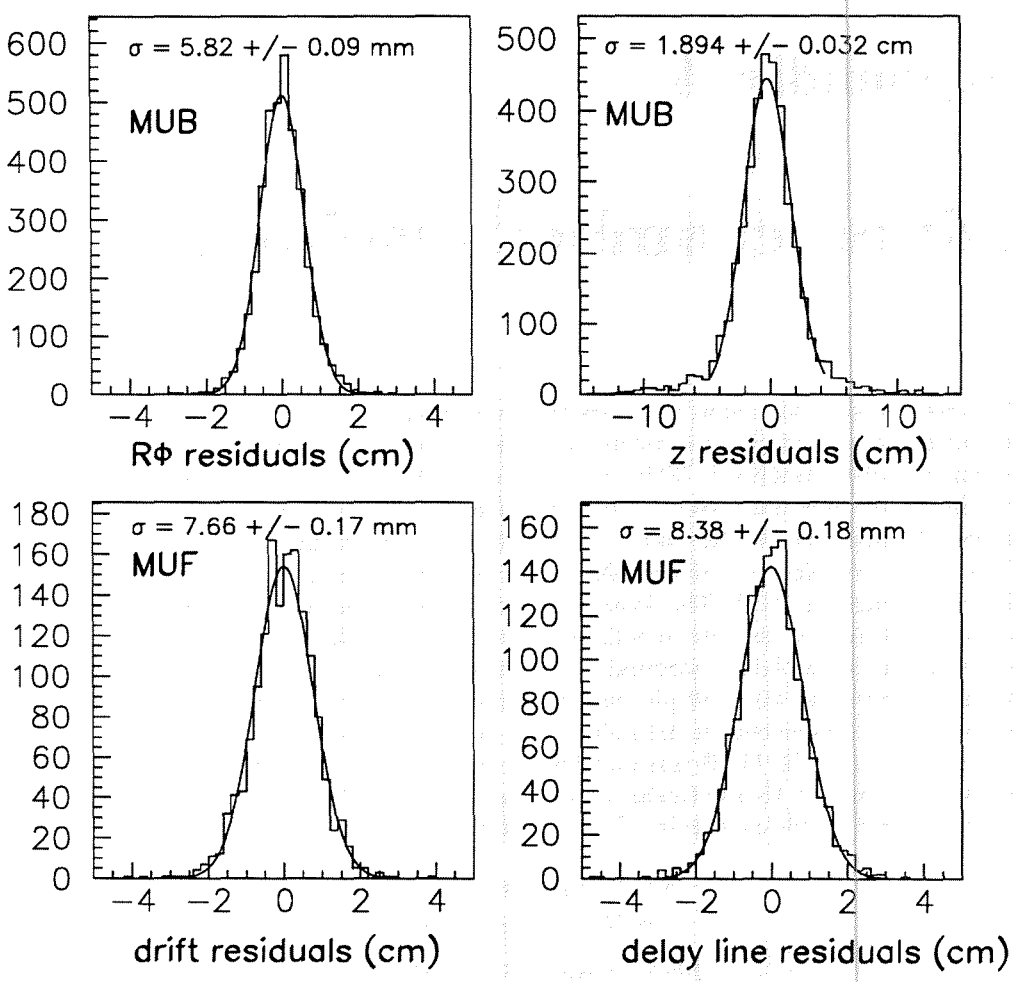

Figure A.1: The residuals in the muon chambers for 1991 muon pair data in MUB and MUF

Appendix B

Correction of systematics

Here, we describe the sources of systematic errors that were found and corrected in the 1990 and 1991 data sets. The final processing of 1990 and 1991 DELANA_E still contains software errors in the extrapolation and fitting. As MUCFIX is redoing the whole extrapolation and association of muon chamber hits, the corrected libraries are picked up at execution level. In addition systematic effects have been observed and can be corrected for.

For the forward region the following corrections are introduced.

1. **Quadrant and endcap alignment (1990)**

   We construct the (extrapolation-hit) variable as the difference of the x (or y) coordinate of the extrapolated hit point at the muon chambers minus the x (or y) coordinate of the muon chamber hit. This distribution should be a gaussian with a mean independent of the impact point. For the 1990 data, a study of the extrapolation-hit distributions for the x and the y coordinate, versus the x and y coordinate respectively shows a discontinuity at $x = 0$ and $y = 0$. For the x-coordinate, this is shown in fig. B.1. This effect is seen in both endcaps. It can show up if each MUF quadrant would be displaced outwards in x and y by 1 cm with respect to the positions recorded in the database. Indeed, investigations showed this to be the case and the error was corrected for the 1991 processings. In MUCFIX, the problem is cured by moving each hit outwards by 1 cm in x and y.

   The plot of $x_{\text{extrapolation}} - x_{\text{hit}}$ versus y (fig.B.2) (and idem for x versus $y_{\text{extrapolation}} - y_{\text{hit}}$) shows a linear behaviour. Again this is seen in both

endcaps. Whether due to an error in the extrapolation, or slight twists in DELPHI, a simple linear correction flattens the distribution.

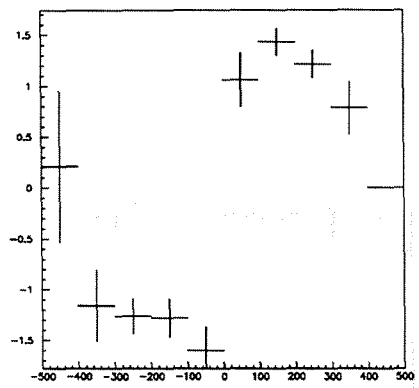

Figure B.1: $x_{\text{extrapolation}} - x_{\text{hit}}$ *versus* x

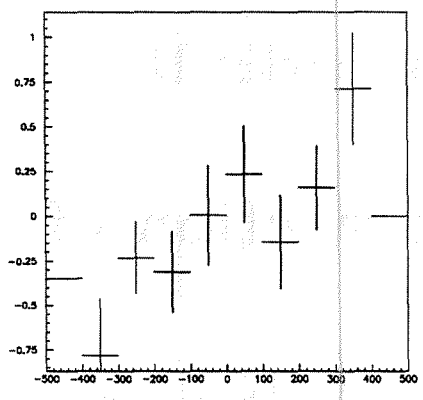

Figure B.2: $x_{\text{extrapolation}} - x_{\text{hit}}$ *versus* y

2. **Smearing of MUF Monte Carlo Hit Points (1990, early 1991)**

   The (extrapolated −hit) distributions of Monte Carlo data in the MUF were found to be too narrow in comparison with those of the data. In the 1990 and early 1991 simulation, the muon chamber hit points are reconstructed with a scatter of only $\sim$ 1 mm. A Gaussian smearing is applied to the hits until agreement is achieved in the (extrapolated − hit) data and Monte Carlo distributions. In figure B.3, this distribution for the coordinate, determined by the anode measurement, is shown for the 1990 Monte Carlo (histogram) and 1990 data (points) before the smearing correction. The same plot is shown in B.4 after the application of the correction.

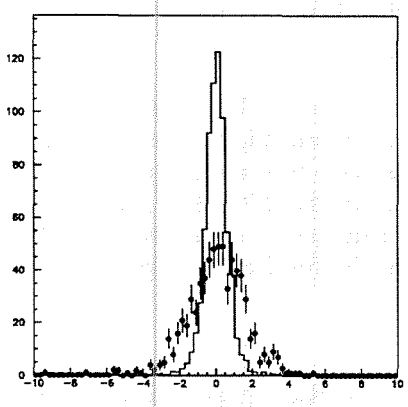

Figure B.3: $anode_{\text{extrapolation}} - anode_{\text{hit}}$ *data and MC before correction*

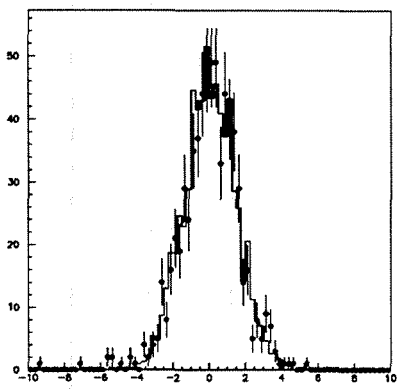

Figure B.4: $anode_{\text{extrapolation}} - anode_{\text{hit}}$ *data and MC after correction*

3. **Bug in Track Errors (1990, 1991)**

   When trying to devise an algorithm for identifying muons in hadronic jets for 1991 data, a significant decrease in efficiency was observed for low momentum forward muons. These low momentum muons (3-7 GeV/c) had an excessively high global χ^2 per degree of freedom. The effect was present in all Monte Carlo and data sets and was traced back to incorrectly calculated multiple scattering errors from the extrapolation through the HCAL in the forward region. Once this bug in the extrapolation package was cured, MUCFIX could reperform the extrapolation and redo the muon hit association, thereby yielding the correctly calculated χ^2's.

Four systematic effects have been discovered in the barrel region data:

1. **Error in $R\phi$ Extrapolation. (1990,1991)**

   Plotting the difference between the muon chamber hits and the DELPHI extrapolation in the $R\phi$ coordinate shows a systematic offset that increases with decreasing momentum and has an opposite sense for positive and negative tracks. This effect is not seen in the Monte Carlo and is most likely

caused by errors in the mapping of the return field. A simple adjustment can be made to the extrapolation of the tracks on the software reference surfaces, prior to translation into the chambers.

2. **Error in z Extrapolation (1990,1991)**

   Plotting the difference between the muon chamber hits and the DELPHI extrapolation in the z coordinate shows a z dependent offset. The causes of this discrepancy are unknown. It has been observed in other detectors and most probably arises from an error in the TPC drift velocity. For muon identification purposes it is sufficient merely to adjust the z of the extrapolation so as to flatten the above distribution. A slightly different correction is required for each data set.

3. **MUB T_0 Shift (1990,1991)**

   The interval between the start of the MUB digitising clocks and the arrival in the readout of hits from an event immediately adjacent to the anode wire is termed the 'T_0'. This is a constant which must be subtracted from all anode signals to give the correct absolute drift time. Its value can be estimated from measurements at the pit, but with low precision on account of the limited statistics. In the 1991 data in particular, a significant discrepancy exists between the correct T_0 and the one used in the offline DELANA processing. Within MUCFIX a correction is made by transforming the hit point back into the chamber frame and moving the drift coordinate 2.5 mm closer to the anode wire. This centers the distribution. Smaller corrections are required for 1990.

4. **Badly Calibrated Delay Lines (1990)**

   Each muon chamber can return up to three signals: one drift time from the anode, t_a, and two times from either end ('near' and 'far') of the delay line, t_n and t_f. These times are converted into distances according to fourth order polynomials, the coefficients of which were determined in Oxford on a cosmic ray test prior to installation in DELPHI.

   If these three signals all originate from a common ionisation, they will obey the following relation:

$$t_n + t_f - 2t_a \simeq t_{dl}$$

   (neglecting anode propagation time) where t_{dl} is the time of propagation of a pulse along the full length of the delay line, also measured in Oxford for each chamber. As t_{dl}'s and delay line coefficients of certain chambers were incorrectly measured, the z-coordinate was badly determined. In the refit this problem was cured by adding or subtracting a constant to the z values of those chambers.

Appendix C

Acceptance correction for the forward-backward asymmetry

In this appendix, we calculate the correction we have to apply to the forward-backward asymmetry in order to correct for the limited detector acceptance. In case of full acceptance, the angular distribution of the b quark is given by

$$\frac{dN}{dx} = A(1+x^2) + Bx, \tag{C.1}$$

with $x = \cos\theta_b$. θ_b is approximated by the polar angle of the thrust axis and $\cos\theta_{thrust}$ is signed by minus the muon charge, such that a μ^-, expected to originate from a b quark, in the forward hemisphere will contribute a positive $\cos\theta_{thrust}$. The forward-backward asymmetry is then given by $A_{FB} = \frac{3}{8}\frac{B}{A}$. We have the following relation:

$$\frac{dN}{dx} \sim (1+x^2) + \frac{8}{3}A_{FB}x, \tag{C.2}$$

and consequently

$$A_{FB} = \frac{N_F - N_B}{N_F + N_B},$$

with N_F and N_B the number of forward (x between 0 and 1) and backward (x between -1 and 0) events. We do not measure $\frac{dN}{dx}$, but a distribution $\frac{dN_{obs}}{dx}$:

$$\frac{dN_{obs}}{dx} = Acc(|x|)\frac{dN}{dx},$$

where $Acc(|x|)$ is the acceptance of the detector, which we assume to be even in x. We measure the asymmetry:

$$A_{FB}^{meas} = \frac{N_F^{meas} - N_B^{meas}}{N_F^{meas} + N_B^{meas}} = \frac{\int_0^1 Acc(|x|)\frac{dN}{dx}dx - \int_{-1}^0 Acc(|x|)\frac{dN}{dx}dx}{\int_{-1}^1 Acc(|x|)\frac{dN}{dx}dx}$$

or

$$A_{FB}^{meas} = \frac{2\int_0^1 Acc(|x|)\frac{8}{3}A_{FB}\,x dx}{2\int_0^1 Acc(|x|)(1+x^2)dx}$$

or

$$A_{FB}^{meas} = \frac{\int_0^1 Acc(|x|)x dx}{\int_0^1 Acc(|x|)(1+x^2)dx}\,\frac{8}{3}A_{FB}$$

The correction factor we have to apply to our measured asymmetry is therefore:

$$Cor = \frac{3}{8}\frac{\int_0^1 Acc(|x|)(1+x^2)dx}{\int_0^1 Acc(|x|)x dx}.$$

We do not need to know the absolute acceptance, only its variation as a function of $\cos\theta_b$. The angular distribution of b and $\bar{b}$ quarks is according to (C.1) given by $(1+x^2)$. Hence we use the angular distribution of all muons $N_{all}(|x|)$ to estimate the acceptance.

$$Acc(|x|) = \frac{N_{all}(|x|)}{1+x^2}$$

The correction factor becomes:

$$Cor = \frac{3}{8}\frac{\int_0^1 N_{all}(|x|)dx}{\int_0^1 \frac{N_{all}(|x|)}{1+x^2}x dx}$$

In terms of our binned histograms, this is:

$$Cor = \frac{3}{8}\frac{\sum_{forw} N_{all}(x)}{\sum_{forw}\frac{N_{all}(x)x}{1+x^2}}$$

Bibliography

[1] F.J.Hasert et al., Phys. Lett. **B46** (1973) 121.

[2] F.J.Hasert et al., Phys. Lett. **B46** (1973) 138.
F.J.Hasert et al., Nucl. Phys. **B73** (1974) 1.

[3] P.Jenni, in Proceedings of the 1987 International Symposium on Lepton and Photon Interactions at High Energy, Hamburg, ed. W.Bartel and R.Ruckl, Nucl. Phys. **B (proc.Suppl.) 3** (1988) 341.

[4] J.Alitti et al., UA2 Coll., Phys. Lett. **B276** (1992) 354.
F.Abe et al., CDF Coll., Phys. Rev. Lett. **65** (1990) 2243.

[5] I.J.R.Aitchison and A.J.G.Hey, *Gauge Theories in Particle Physics*, Adam Hilger(1989).

[6] Review of Particle Properties, Phys. Rev. **D45** (1992) 1.

[7] W.Hollik, *Precision Tests of the Electroweak Theory Part I*, CERN-TH.5661/90

[8] M.Consoli et al., CERN Report "Physics at LEP1", Vol.1 89-08(1989)7.

[9] C.Burgers et al., CERN Report "Physics at LEP1", Vol.1 89-08(1989)55.

[10] A.Djouadi et al., Z. Phys. **C46** (1990) 411.

[11] A.Djouadi et al., Nucl. Phys. **B349** (1991) 48.

[12] M.Boulware and D.Finnell, Phys. Rev. **D44** (1991) 2054.

[13] The LEP Collaborations and the LEP Electroweak Working Group, *Updated Parameters of the Z^0 resonance from Combined Preliminary Data of the LEP Experiments*, CERN-PPE/93-157

[14] N.Isgur and M.B.Wise, Phys. Lett. **B232** (1989) 113.

[15] C.Peterson et al., Phys. Rev. **D27** (1983) 105.

[16] T.Sjöstrand, Int. J. of Mod. Phys. **A3** (1988) 751.

[17] T.Sjöstrand and M.Bengtsson, Comput. Phys. Commun. **43** (1987) 367.

[18] A.Blondel et al., *A determination of the $Zb\bar{b}$ vertex correction from LEP data*, DESY 92-112.

[19] LEP Design Report, CERN Report LEP/84-01 (1984).

[20] The LEP collider-construction, project status and outlook, CERN/LEP-DI-IM-RF/89-41.

[21] Estimates of particle backgrounds at the LEP detectors, CERN/LEP-BI/88-52.

[22] DELPHI Collaboration, Nucl. Instr. and Meth. **A303** (1991) 233.

[23] The DELPHI detector, CERNL/LEPC/83-3 and DELPHI 83-66/1.

[24] The DELPHI detector, CERNL/LEPC/84-16 and DELPHI 84-60 GEN-11.

[25] The DELPHI Microvertex Detector, DELPHI 92-137 PHYS 236.

[26] J.Buytaert, L.De Boeck et al., Nucl. Instr. and Meth. **A310** (1991) 596.

[27] F.Stichelbaut et al., Nucl. Instr. and Meth. **283** (1989) 792.

[28] DELPHI Collaboration, Nucl. Phys. **B367** (1991) 511.

[29] J.A.Fuster et al., *The Online Software for the First and Second Level Trigger of DELPHI*, DELPHI 91-112 DAS 115.

[30] L.Benetau et al., *Architecture and Performance of the DELPHI Trigger system*, DELPHI 92-162 DAS 135.

[31] DELPHI Collaboration, *DELPHI data analysis program (DELANA) user's guide*, DELPHI 89-44 PROG 137.

[32] D.Bertrand and L.Pape, *TANAGRA track analysis and graphics package*, DELPHI 87-95 PROG-98.

[33] DELPHI Collaboration, *DELSIM DELPHI event generation and detector simulation*, DELPHI 89-67 PROG 142.

[34] P.Abreu et al., *Event viewing software, Installation Procedure and user's manual*, DELPHI 89-06 PROG 126 (1989).

[35] T.Sjöstrand, Comput. Phys. Commun. **27** (1982) 243.
T.Sjöstrand, Comput. Phys. Commun. **28** (1983) 229.
T.Sjöstrand and M.Bengtsson, Nucl. Phys. **B289** (1987) 810.

[36] T.Sjöstrand and M.Bengtsson, Phys. Lett. **B185** (1987) 435.
T.Sjöstrand, Comput. Phys. Commun. **39** (1986) 347.

[37] L.Bugge, *Tracking of Charged Particles through the DELPHI calorimeters*, DELPHI 89-4 PROG 125.

[38] N.Crosland, P.Kluit and G.Wilkinson, *EMMASS*, DELPHI 92-17 PHYS 157.

[39] G.Wilkinson and P.Collins, *MUCFIX*, DELPHI 93-13 PHYS 262.

[40] H.De Boeck and G.Wilkinson, *MUFLAG*, DELPHI 93-14 PHYS 263.

[41] H.De Boeck and P.Kluit, Internal DELPHI report, February 1992.

[42] P.Kluit, Internal DELPHI report, 1992.

[43] P.Abreu et al., Nucl. Phys. **B367** (1991) 511.

[44] JADE Collaboration, W.Bartel et al., Z. Phys. **C33** (1986) 23.
S.Bethke et al., Phys. Lett. **B213** (1988) 235.

[45] D.Decamp et al., Phys. Lett. **B244** (1990) 551.
D.Decamp et al., Phys. Lett. **B263** (1991) 325.

[46] M.Z.Akrawy et al., Phys. Lett. **B263** (1991) 311.
P.Acton et al., Z. Phys. **C55** (1992) 191.

[47] B.Adeva et al., Phys. Lett. **B241** (1990) 416.
B.Adeva et al., Phys. Lett. **B252** (1990) 713.
B.Adeva et al., Phys. Lett. **B261** (1991) 177.

[48] J.F.Kral et al., Phys. Rev. Lett. **64** (1990) 1211.

[49] P.Abreu et al., Phys. Lett. **B281** (1992) 383.
P.Abreu et al., Phys. Lett. **B295** (1992) 383.

[50] O.Adriani et al., Phys. Lett. **B307** (1993) 237.

[51] R.Jacobsen et al., Phys. Rev. Lett. **67** (1991) 3347.

[52] P.Abreu et al., Phys. Lett. **B295** (1992) 383.

[53] P.Billoir et al., *B-tagging by Hemisphere: Description of variables and Results on Monte-Carlo*, DELPHI 93-54 PHYS 282.
V.Castillo et al., *Measurement of the $Z^0 \rightarrow b\bar{b}$ branching ratio by hemisphere double tagging*, DELPHI 93-75 PHYS 302.

[54] P.Abreu et al., Phys. Lett. **B276** (1992) 536.

[55] P.Antilogus, H.De Boeck et al., *Measurement of the Forward Backward Asymmetry of* $e^+e^- \rightarrow Z^0 \rightarrow b\bar{b}$ *using prompt muons*, DELPHI 92-96 PHYS 207.

[56] P.Abreu et al., Z. Phys. **C56** (1992) 47.

[57] D.J.Crennell et al., $\Gamma_{b\bar{b}}/\Gamma_{had}$ *and* $< x_E >_B$ *Using the* Z^0 *Semi Leptonic Decay into Muons*, DELPHI 92-105 PHYS 211.

[58] M.Calvi et al., *Determination of* $\Gamma_{b\bar{b}}$ *and* $BR(b \rightarrow l)$ *using semileptonic decays*, DELPHI 93-74 PHYS 301.

[59] P.Antilogus et al., *Measurement of the forward-backward asymmetry of* $e^+e^- \rightarrow Z^0 \rightarrow b\bar{b}$ *using prompt muons*, DELPHI 93-77 PHYS 304.

[60] T.Baroncelli et al., *Inclusive measurement of the forward-backward asymmetry in* $Z \rightarrow b\bar{b}$ *events at LEP*, DELPHI 93-78 PHYS 305.

[61] T.Baroncelli et al., *Measurement of* $\frac{\Gamma_{b\bar{b}}}{\Gamma_{had}}$ *using microvertex and lepton double tags*, DELPHI 93-93 PHYS 320.

[62] ALEPH Collaboration, *A Precise Measurement of* $\Gamma_{Z\rightarrow b\bar{b}}/\Gamma_{Z\rightarrow hadrons}$, CERN-PPE/93-108.

[63] ALEPH Collaboration, *Measurement of the ratio* $\Gamma_{b\bar{b}}/\Gamma_{had}$ *using Event Shapes Variables*, CERN-PPE/93-113, submitted to Phys. Lett. **B.**

[64] ALEPH Collaboration, *A measurement of* $\Gamma_{b\bar{b}}/\Gamma_{had}$ *using leptons*, ALEPH Note 93-135 PHYSIC 93-166.

[65] The OPAL Collaboration, *Measurement of* $\Gamma(Z \rightarrow b\bar{b})/\Gamma(Z \rightarrow hadrons)$ *using impact parameters and leptons,* CERN-PPE/93-155.
The OPAL Collaboration, *Measurement of* $\Gamma(Z \rightarrow b\bar{b})/\Gamma(Z \rightarrow hadrons)$ *using Leptons,* CERN-PPE/93-46.
OPAL Collaboration, P.D.Acton et al., Z. Phys. **C58** (1993) 523.
OPAL Collaboration, *A measurement of* $\Gamma_{b\bar{b}}/\Gamma_{had}$ *Using Single and Double Lepton events*, OPAL Internal Physics Note PN091, 22 February 1993.

[66] S.Jadach and Z.Was, *The Monte Carlo program KORALZ*, CERN TH 5994-91 (1991).

[67] OPAL Collaboration, *An updated Measurement of* $\Gamma(Z \rightarrow b\bar{b})/\Gamma(Z \rightarrow hadrons)$ *Using an Impact Parameter Technique*, CERN-PPE/93-79, submitted to Z.Phys.C.

[68] OPAL Collaboration, *An Updated Measurement of* $\Gamma_{b\bar{b}}/\Gamma_{had}$ *Using Double Lifetime Tagging*, OPAL Note PN104, 7 July 1993.

[69] L3 Collaboration, *Measurement of $R_{b\bar{b}}$ and $Br(b \to l\nu X)$ from b-quark Semileptonic Decays*, L3 Note 1449, July 1993.

[70] ALEPH Collaboration, *$B^0\bar{B}^0$ mixing and $b\bar{b}$ asymmetry for high p_t leptons (update)*, ALEPH Note 93-132 PHYSIC 93-113.

[71] L3 Collaboration, *An Updated Measurement of χ_B, $A_{FB}^{b\bar{b}}$ and $A_{FB}^{c\bar{c}}$*, L3 Note 1448, July 1993.

[72] OPAL Collaboration, *The Forward-Backward Asymmetry of $e^+e^- \to b\bar{b}$ and $e^+e^- \to c\bar{c}$ Using Leptons in Hadronic Z^0 Decays*, CERN-PPE/93-78, submitted to Z. Phys. C.

[73] ALEPH Collaboration, *A Preliminary Measurement of $\sin^2\theta_W^{eff}$ from $A_{FB}^{b\bar{b}}$ in the 1992 lifetime tagged Heavy-Flavour sample*, ALEPH 93-134 PHYSIC 93-115.

[74] D.Bardin et al., Z. Phys. **C44** (1989) 493.
D.Bardin et al., Comput. Phys. Commun. **59** (1990) 303.
D.Bardin et al., Nucl. Phys. **B351** (1991)1.

[75] DELPHI Collaboration, *An improved measurement of $B^0\bar{B}^0$ mixing using semileptonic b decays*, DELPHI 93-80 PHYS 307.
OPAL Collaboration, *Measurements of $B^0\bar{B}^0$ mixing, $\Gamma(Z^0 \to b\bar{b})$ and semileptonic branching ratios for b-flavoured hadrons in hadronic Z^0 decays*, CERN-PPE/93-106,submitted to Z. Phys. C.

[76] U.Gasparini, *Recent results on heavy flavour physics from LEP experiments using 1990-92 data*, DELPHI 93-126 PHYS 341.

Samenvatting

De electromagnetische en de zwakke interacties kunnen beschreven worden met hetzelfde model: het Standaard Model (SM). Het SM beschrijft waarneembare grootheden, zoals vertakkingsverhoudingen, met een storingsreeks in zijn koppelingsconstanten. Daarom is het belangrijk het SM niet alleen te testen op zijn laagste orde termen, maar ook op het niveau van quantumcorrecties (stralingscorrecties), zoals gebeurd is voor QED. Hiervoor is een precisie nodig op de metingen van 1 procent. Alle fysische deeltjes dragen bij tot deze stralingscorrecties, zodat de (nog onbekende) massa's van de top quark en van het Higgs boson een berekenbare bijdrage geven tot meetbare grootheden. Ook alle deeltjes die optreden in uitbreidingen van of alternatieven voor het SM leveren extra bijdragen. De verhouding van de vertakkingsverhouding van het Z^0 boson, de neutrale drager van de zwakke interactie, in $b\bar{b}$ quark paren tot de vertakkingsverhouding van het Z^0 boson in alle soorten quark paren ($R_b = \frac{\Gamma_{b\bar{b}}}{\Gamma_{had}}$) is een interessante grootheid omwille van de top-massa afhankelijkheid die veel kleiner is dan bij andere vervalwijzen van de Z^0. Hierdoor is R_b gevoelig aan alle "nieuwe" fysica. De voorwaarts-achterwaartse asymmetrie van b quarks in Z^0 vervallen is belangrijk omwille van zijn grote gevoeligheid aan de effectieve menghoek (Weinberg hoek).

De versneller LEP (Large Electron Positron collider) werd gebouwd om heel precies de theorie van de electro-zwakke interactie te testen. De massamiddelpuntsenergie is gelijk aan de massa van de Z^0 resonantie, die in grote aantallen ($\sim$ duizend per uur) geproduceerd worden. Het is een cirkelvormige versneller, die electronen en positronen frontaal laat botsen in 4 interactiepunten. In een van de interactiepunten staat de detector DELPHI (Detector for Electron, Lepton, Photon and Hadron Identification) opgesteld. Deze detector vult de volledige ruimtehoek. Hij bestaat uit verschillende sub-detectoren die elk een specifieke taak hebben. We onderscheiden de spoordetectoren, die het traject van het deeltje registreren, de calorimeters, die plaats en energie van de deeltjes meten en de detectoren die informatie geven over de aard van het deeltje.

De DELPHI detector verzamelde in 1990, 1991 en 1992 gegevens over ongeveer

een miljoen botsingen waarin een Z^0 boson geproduceerd wordt en vervalt in een fermion-antifermion paar. In dit werk, wordt dit staal gebruikt om het verval van het Z^0 boson in bottom-antibottom quark paren te bestuderen. Als een Z^0 vervalt in een quark-antiquark paar, wordt dit waargenomen als 2 groepen (jets) van deeltjes die in tegengestelde richting vliegen. De selectie van de bottom quarks uit het hadronische staal gebeurt op basis van enkele kenmerken van de B hadronen. De B hadronen hebben in vergelijking met de hadronen die afkomstig zijn van lichte quarks (u,d en s quarks), een grote massa, een lange levensduur en een harde fragmentatie[1]. Elk van deze kenmerken vertaalt zich in een "etiketteer"-variabele. Omwille van de grote b massa, zullen de vervalprodukten van het B hadron een grote impuls meekrijgen in het rustsysteem van het hadron. Na een Lorentz transformatie naar het laboratorium stelsel uit dat zich in een grote transversale impuls van het deeltje t.o.v de vluchtrichting van het B hadron. Een lange levensduur geeft aanleiding tot sporen die niet uit het interactiepunt komen (Het B hadron loopt een eindje alvorens het vervalt). Door de harde fragmentatie heeft het B hadron en ook nog zijn vervalprodukten een grote impuls in het laboratorium stelsel.

Voor de analyse van b quark gebeurtenissen, wordt er gebruik gemaakt van het semi-leptonische verval van de B hadronen in muonen. Deze muonen hebben een grote impuls en grote transversale impuls t.o.v. hun jet-as, die in goede benadering de richting van het originele B hadron aangeeft. Hierdoor kunnen de bottom quark gebeurtenissen van de andere onderscheiden worden. Omwille van het grote aantal geladen deeltjes ($\sim$ 21) in hadronische gebeurtenissen, is hier de identificatie van muonen minder eenduidig dan in muon paar gebeurtenissen. Energetische kaonen en pionen hebben een zekere waarschijnlijkheid om de muonkamers te bereiken en daar een signaal te geven. Muonen die in de muonkamers een signaal geven, moeten geassocieerd worden met het juiste spoor in de spoordetectoren voor de impuls en lading bepaling. Er wordt een algoritme ontwikkeld dat muonen in hadronische gebeurtenissen met een goede identificatie efficiëntie identificeert. Op basis van een χ^2-fit van de treffers in de muonkamers met de sporen in de centrale spoordetectoren en de penetratiediepte van het deeltje in het ijzer van de hadron calorimeter, worden de deeltjes al dan niet als muon geïdentificeerd. De efficiëntie voor het detecteren van een muon is $\sim$ 81%, en het percentage aan echte muonen in het aldus bekomen staal is $\sim$ 73%.

De fractie Z^0 bosonen dat vervalt in een $b\bar{b}$ paar, en de voorwaarts-achterwaartse asymmetrie van deze bottom quarks, wordt gemeten. De voorwaarts-achterwaartse asymmetrie wordt bepaald aan de hand van de muonen uit het semi-leptonische verval van de B hadronen. De muonen in de hadronische gebeurtenissen worden verdeeld in verschillende klassen, die elk hun specifieke

[1] D.w.z. dat de B hadronen een grote fractie van de aanwezige b quark energie meekrijgen bij fragmentatie.

impuls en transversale impuls verdelingen hebben. De verschillende klassen zijn:

- $b \to \mu$, $b \to \tau \to \mu$, $J/\psi \to \mu^+\mu^-$
- $b \to c \to \mu$
- $c \to \mu$
- muonen uit het verval van pionen en kaonen
- hadronen geïdentificeerd als muon

De impuls en transversale impuls verdelingen van alle muonen in hadronische gebeurtenissen worden gefit aan de verdelingen van de Monte Carlo simulatie. De muonen uit het semi-leptonische verval van de b quark reflecteren de lading van de b quark. Door het aantal muonen van b gebeurtenissen in de voorwaartse (N_F) en achterwaartse (N_B) richting te meten, wordt de voorwaarts-achterwaartse asymmetrie van de b quark, A^b_{FB}, bepaald:

$$A^b_{FB} = \frac{N_F - N_B}{N_F + N_B}$$

Voor de 1990 en 1991 gegevens, meten we een voorwaarts-achterwaartse asymmetrie van

$$A^b_{FB} = 0.113 \pm 0.39(stat) \pm 0.013(syst) \pm 0.004(mix)$$

Hetzelfde resultaat wordt bekomen uit een fit van het produkt van de lading van het muon met de $(-\cos\theta_{thrust})$ verdeling van de hadronische gebeurtenissen, na aftrek van de bijdrage van de niet-prompte muonen. De verdeling wordt gefit met de volgende vorm:

$$\frac{d\sigma}{d\cos\theta_b} \propto (1 + \cos^2\theta_b + \frac{8}{3}A^b_{FB}\cos\theta_b),$$

waarin θ_b de polaire hoek is van de b quark.

De b partiële breedte wordt met twee verschillende methoden bepaald. De eerste methode, uitgevoerd op de 1990 en 1991 gegevens, is eveneens gebaseerd op het semi-leptonische verval in muonen. De muon impuls en transversale impuls verdelingen worden gefit aan die van de Monte Carlo simulatie. Hieruit wordt het produkt van de partiële breedte met de inclusieve vertakkingsverhouding van b quarks in muonen bepaald. Voor de 1990 en 1991 DELPHI gegevens, wordt het volgende resultaat verkregen:

$$\frac{\Gamma_{b\bar{b}}}{\Gamma_{had}} BR(b \to \mu) = 0.02232 \pm 0.00048(stat) \pm 0.00135(syst)$$

Een tweede meting van $\Gamma_{b\bar{b}}/\Gamma_{had}$ maakt, naast het semi-leptonische verval van b quarks in muonen, ook gebruik van de grote impactparameter die sporen hebben die komen van het verval van een B hadron. Deze meting is een "gemengde etiketteer" methode, d.w.z. dat door gebruik te maken van twee verschillende etiketteer methodes in de twee hemisferen van een gebeurtenis, de efficiënties rechtstreeks bepaald worden uit de gegevens. Een gebeurtenis wordt opgedeeld in twee hemisferen, door het vlak door de oorsprong en loodrecht op de *uitval*-as. Het hadronische staal wordt vervolgens opgesplitst in drie sub-stalen:

- Het hoge p_t staal van gebeurtenissen waarin in één van de hemisferen zich een muon bevindt met een transversale impuls t.o.v. zijn jet-as groter dan 1 GeV/c.
- Het lage p_t staal van gebeurtenissen waarin zich een muon bevindt met een transversale impuls kleiner dan 1 GeV/c.
- Alle hadronische gebeurtenissen.

Voor elk van de twee hemisferen wordt een multipliciteitsverdeling gemaakt. De multipliciteit is hier het aantal sporen in de hemisfeer waarvan de verhouding van de impactparameter tot zijn resolutie groter is dan 2. Er wordt verondersteld dat de samenstelling aan b, c en lichte quarks van het eerste en tweede staal gekend zijn, relatief t.o.v. het hadronische staal. Vervolgens beschouwt men voor de eerste twee stalen de multipliciteitsverdeling van de hemisfeer waartoe het muon *niet* behoort. Deze verdeling is een superpositie van 3 verdelingen, nl. van de multipliciteitsverdeling van de b, de c en de uds gebeurtenissen omdat deze drie klassen gekarakteriseerd zijn door verschillende levensduren. Vermits de relatieve samenstelling van deze eerste twee stalen gekend is, kan de $(Z \rightarrow b\bar{b})/(Z \rightarrow \text{hadronen})$ en de multipliciteitsverdeling van de klassen b, c en uds bepaald worden.

$$R_b = \frac{\Gamma_{b\bar{b}}}{\Gamma_{had}} = 0.2190 \pm 0.0053(stat) \pm 0.0090(syst).$$

Uit de voorwaarts-achterwaartse b asymmetrie, wordt de effectieve Weinberg hoek bepaald:

$$\sin^2\theta_{eff} = 0.2289 \pm 0.0069(stat) \pm 0.0024(syst)$$

Uit de beide metingen van de partiële breedte, wordt de inclusieve semi-leptonische vertakkingsverhouding voor b quarks bepaald.

$$BR(b \rightarrow \mu) = 10.19 \pm 0.33(stat) \pm 0.52(syst)\%$$

Het LEP gemiddelde (1990-1992) voor R_b is 0.2200 ± 0.0027. Deze meting ligt in de buurt van een 1% precisie. De gemengde en dubbele etiketteermethoden zijn beloftevolle methodes om deze precisie beneden de 1% te krijgen. De bepaling van $\sin^2_{eff}$ uit de b asymmetrie meting van 1991-1992 gegevens is, dankzij de grotere gevoeligheid, de hoge statistiek in 1992 en de vooruitgang in het begrijpen van de systematische onzekerheden, competitief met de metingen gebaseerd op leptonische eindtoestanden. De resultaten van dit proefschrift, nl. $\Gamma_{b\bar{b}}$, A^b_{FB} en $\sin^2\theta_{eff}$ zijn in uitstekende overeenstemming met het Standaard Model dat de electro-zwakke interacties beschrijft.

Addendum: list of abbreviations

ADC	Analog to Digital Converter
BCO	Beam Cross Over signal
BRICH	Barrel Ring Imaging Cherenkov Counter
CEB	Crate Event Buffer
CP	Crate Processor
DAQ	Data Acquisition
DAS	Data Acquisition System
DELPHI	Detector with Lepton, Photon and Hadron Identification
DST	Data Summary Tape
EM	Electromagnetic
EPA	Electron Positron Accumulating Ring
FCA	Forward Chamber A
FCB	Forward Chamber B
FEB	Front End Buffer
FEMC	Forward Electromagnetic Calorimeter
FRICH	Forward Ring Imaging Cherenkov Counter
GEB	Global Event Buffer
HAC	Hadron Calorimeter
HOF	Forward Hodoscope
HPC	High-density Projection Chamber
ID	Inner Detector
LEP	Large Electron Positron collider
LIL	Linear Injection Linac
LTD	LEP Time Digitiser
MC	Monte Carlo simulation
MEB	Multi Event Buffer
MIM	Minimal Invariant Mass algorithm
MSM	Minimal Standard Model
MUB	Barrel Muon Chambers
MUC	Muon Chambers
MUF	Forward Muon Chambers
MVD	Microvertex Detector
MWPC	Multi Wire Proportional Chamber

OD	Outer Detector
PS	Proton Synchrotron
PYTHIA	Trigger supervisor decision box
RICH	Ring Imaging Cherenkov Counter
SAT	Small Angle Tagger
SM	Standard Model
SPS	Super Proton Synchrotron
SUSY	Supersymmetry
TD	detector data
TDC	Time to Digital Converter
TDL	Trigger Data Line
TE	Track Elements
TK	Tracks
TOF	Time-Of-Flight counter
TPC	Time Projection Chamber
VSAT	Very Small Angle Tagger
ZEUS	Trigger supervisor control box